

TRANSPORT AND PHASE TRANSITIONS IN CERAMICS AND AMORPHOUS
METALS BY ATOMIC-LEVEL SIMULATION

By

BRIAN J. DEMASKE

A DISSERTATION PRESENTED TO THE GRADUATE SCHOOL
OF THE UNIVERSITY OF FLORIDA IN PARTIAL FULFILLMENT
OF THE REQUIREMENTS FOR THE DEGREE OF
DOCTOR OF PHILOSOPHY

UNIVERSITY OF FLORIDA

2017

© 2017 Brian J. Demaske

To my friends and family

ACKNOWLEDGMENTS

I want to thank my advisor Prof. Simon Phillpot for his guidance over the past four and a half years. He has always been receptive and understanding to any issues that have arisen during my graduate education, both in my research and personal life. He exemplified the role of a mentor by always putting his students and their well-being before anything else. His words of encouragement often came at just the right time to give me that much-needed boost of confidence. He has promoted me to think independently and gradually pushed me towards self-sufficiency in my work. Both skills that are invaluable to a successful career in scientific research.

I would also like to acknowledge the other members of my doctoral committee: Prof. Sinnott, Prof. Spearot, Prof. Yang, Prof. Andrew and Prof. Hamlin. I want to thank them for the time and energy they have invested into this process. I would especially like to thank Prof. Spearot for his thoughtful discussions and guidance during early Friday morning meetings on shock waves. I would also like to extend my thanks to Prof. Tonks for taking time out of his schedule to serve as a substitute during my oral defense and for helpful suggestions on how to improve this dissertation. Although I am not a member of his group, Prof. Hennig kindly offered me an account on his allocation on the University's supercomputer. This extra bit of computing power made a world of difference in my work and I thank him for his generosity. I would also like to thank Dr. Alex Chernatynskiy, who helped me tackle my first project upon joining the group. Last, but not least, I would like to thank the other students in our group, both past and present, who helped to make graduate school enjoyable.

Making it this far would not have been possible without the love and support of my family. My parents gave me the foundation of a strong family and taught me the

importance of maintaining a balance between life and work. Both my brother and sister have always been there for me, from our early years growing up in Ohio all the way up to today. I could not imagine my life without them. Finally, I would like to thank Danielle, who has become my closest friend over these last few years. Her constant love and support have helped me through some rough patches. I could not have done this without her by my side.

TABLE OF CONTENTS

	<u>page</u>
ACKNOWLEDGMENTS	4
LIST OF TABLES	9
LIST OF FIGURES	11
LIST OF ABBREVIATIONS.....	15
ABSTRACT.....	16
CHAPTER	
1 INTRODUCTION	18
1.1 General Overview	18
1.2 Motivation of Problems	19
1.2.1 Vanadium Carbide Diffusion Barrier.....	19
1.2.2 High-strain-rate Deformation of Metallic Glasses	21
1.2.3 Lanthanum Borogermanate Glass-ceramics	24
1.3 Outline	25
2 OVERVIEW OF SIMULATION METHODS.....	27
2.1 Density Functional Theory	27
2.2 Modern Theory of Polarization	29
2.3 Molecular Dynamics.....	30
2.4 Embedded Atom Method	32
3 INTRINSIC DEFECTS AND SELF-DIFFUSION IN VANADIUM CARBIDE	34
3.1 Background	34
3.2 Simulation Methods	36
3.3 Simulation Results	39
3.3.1 Ordered Structures of V_2C	39
3.3.2 Electronic and Elastic Properties of V_2C	44
3.3.3 Vacancy Formation Energies	48
3.3.4 Energy Barriers for Self-diffusion	50
3.3.4.1 Vanadium self-diffusion	50
3.3.4.2 Carbon self-diffusion.....	56
3.4 Discussion	62
3.5 Summary	68
4 ENERGETICS AND KINETICS OF METAL IMPURITIES IN VANADIUM CARBIDE	69

4.1	Background	69
4.2	Simulation Methods	70
4.3	Simulation Results	74
	4.3.1 Impurity Site Preference	74
	4.3.2 Impurity-vacancy Binding	77
	4.3.3 Migration Barriers for Impurity Diffusion.....	81
4.4	Summary	83
5	SHOCK COMPRESSION OF COPPER-ZIRCONIUM METALLIC GLASSES.....	84
5.1	Background	84
5.2	Simulation Methods	86
	5.2.1 Interatomic Potential Verification.....	86
	5.2.2 Amorphous Structure Creation.....	89
	5.2.3 Piston-driven Shock Method	91
5.3	Simulation Results	93
	5.3.1 Shock Wave Structure at Different Shock Intensities	93
	5.3.2 Hugoniot Elastic Limit	95
	5.3.3 U_p - U_s Shock Hugoniot	96
	5.3.4 Composition Dependence of the Shock Response.....	100
5.4	Discussion	105
	5.4.1 Pressure-dependent Yield Criterion	105
	5.4.2 Bilinear U_p - U_s Hugoniot	107
5.5	Summary	107
6	MICROSTRUCTURAL RESPONSE OF METALLIC GLASSES TO SHOCK LOADING	109
6.1	Background	109
6.2	Simulation Methods	111
6.3	Simulation Results	114
	6.3.1 Shock-induced Deformation	114
	6.3.2 Composition Dependence and Melting	119
	6.3.3 Local Structural Changes During Shock Compression	124
6.4	Summary	129
7	FERROELECTRICITY IN LANTHANUM BOROGERMANATE	131
7.1	Background	131
7.2	Simulation Methods	132
7.3	Simulation Results	133
	7.3.1 Low-temperature Phase of LaBGeO_5	133
	7.3.2 High-temperature Phase of LaBGeO_5	139
	7.3.3 Lattice Dynamics of the Ferroelectric Phase Transition	142
	7.3.4 Spontaneous Polarization.....	146
7.4	Discussion	147
7.5	Summary	149

8 CONCLUSIONS.....	151
LIST OF REFERENCES.....	158
BIOGRAPHICAL SKETCH.....	173

LIST OF TABLES

<u>Table</u>	<u>page</u>
3-1	Lattice constants and cohesive energies for the α and β' phases of V_2C and the low-energy structure belonging to space group $Pn\bar{m}$41
3-2	Zero-temperature elastic constants and elastic moduli for the three ordered V_2C structures.....45
3-3	Vacancy formation energies ΔE_f and vibrational formation entropies ΔS_f^{vib} for the three ordered V_2C structures calculated using DFT.49
3-4	Migration energies ΔE_A^m and ΔE_B^m and effective frequencies ν^* for the vacancy-assisted vanadium self-diffusion mechanism for the three ordered V_2C structures calculated using DFT.54
3-5	Correlation factors for vacancy-assisted self-diffusion in an hcp lattice calculated using values of w_A/w_B obtained for vanadium self-diffusion in the β' phase of V_2C55
3-6	Activation energies Q and diffusion prefactors D_0 for vacancy-assisted vanadium self-diffusion for the three ordered V_2C structures calculated using DFT.56
3-7	Migration energies ΔE_A^m and ΔE_B^m and effective frequencies ν^* for carbon self-diffusion for each of the three ordered V_2C structures calculated using DFT.61
3-8	Activation energies Q and diffusion prefactors D_0 for carbon self-diffusion for each of the three ordered V_2C structures calculated using DFT.62
4-1	Theoretical equilibrium lattice constants, cohesive energies and magnetic moments for ground state phases of V, Fe, Ni, Ce, Nd and U.71
4-2	Supercell dimensions and calculation parameters used in defect calculations for α - V_2C73
4-3	Substitutional and interstitial defect formation energies and impurity volumes....76
4-4	Impurity-vacancy binding energies for each of the six in-plane and six out-of-plane nearest-neighbor sites on the vanadium sublattice.....79
5-1	Calculated elastic constants and glass transition temperature T_g for $Cu_{30}Zr_{70}$, $Cu_{50}Zr_{50}$ and $Cu_{70}Zr_{30}$ metallic glass samples.91
5-2	Calculated parameters for both the elastic and plastic branches of the U_p - U_s Hugoniot for $Cu_{30}Zr_{70}$, $Cu_{50}Zr_{50}$ and $Cu_{70}Zr_{30}$ metallic glass.....100

7-1	Comparison of equilibrium lattice constants for the low-temperature phase of LaBGeO ₅	134
7-2	Comparison of atom positions for the low-temperature phase of LaBGeO ₅	136
7-3	Comparison of B-O, Ge-O and La-O interatomic distances (in Å) for the low-temperature phase of LaBGeO ₅	137
7-4	Comparison of atom positions for the high-temperature phase of LaBGeO ₅	141
7-5	Comparison of B-O, Ge-O and La-O interatomic distances (in Å) for the high-temperature phase of LaBGeO ₅	143
7-6	Atom displacements for the Γ -point modulation of the high-temperature phase and those between the initial and saddle points along the MEP.	148

LIST OF FIGURES

<u>Figure</u>	<u>page</u>
1-1	Dependence of fracture strength on strain rate for several metallic glasses.22
3-1	Symmetry-unique superstructures generated from a 4-site hexagonal cell in order of increasing volume.....40
3-2	Energies for a subset of low-energy V_2C structures enumerated from derivative superstructures with volumes ≤ 8 times the volume of the base 4-site hexagonal cell.42
3-3	Unit cells of three ordered V_2C structures including the low-energy orthorhombic structure belonging to space group $Pn\bar{m}$, the α phase and the β' phase.43
3-4	Electronic band structure and DOS for the α phase of V_2C from DFT calculations.44
3-5	Spatial variation in of the Young's modulus E for the low-energy orthorhombic structure belonging to space group $Pn\bar{m}$, the α phase of V_2C and the β' phase of V_2C46
3-6	Theoretical phonon DOS for the low-energy orthorhombic structure belonging to space group $Pn\bar{m}$, the α phase of V_2C and the β' phase of V_2C47
3-7	Calculated vacancy formation energies as a function of the number of atoms in the supercell for the low-energy structure belonging to space group $Pn\bar{m}$, the α phase of V_2C and the β' phase of V_2C48
3-8	In-plane and out-of-plane jumps for vanadium to a nearest-neighbor site within the vanadium sublattice without octahedral sites shown and with octahedral sites shown.....51
3-9	Theoretical MEPs for vanadium vacancy migration for in-plane and out-of-plane migration for the α phase from CI-NEB calculations.53
3-10	Coordination polyhedra for the octahedral and tetrahedral interstitial sites in V_2C57
3-11	Octahedral-octahedral, labeled A and B, and octahedral-tetrahedral-octahedral, labeled C, site jumps considered as likely migration paths for carbon self-diffusion in V_2C without and with the vanadium atoms shown.58
3-12	Theoretical MEPs for carbon interstitial migration in-plane and out-of-plane for the β' phase from CI-NEB calculations.60

3-13	Illustration showing arrangement of carbon atoms for the α phase of V_2C and the low-energy orthorhombic structure described by space group $Pn\bar{m}$	64
3-14	Calculated vanadium self-diffusion coefficients for the three ordered V_2C structures and experimental self-diffusion coefficients for Nb in NbC_x and Ti in TiC_x	66
3-15	Calculated carbon self-diffusion coefficients for the three ordered V_2C structures and experimental self-diffusion coefficients for C in $NbC_{0.868}$ and C in V_6C_5	67
4-1	Unit cell of low-temperature ordered orthorhombic phase α - V_2C	72
4-2	Convergence of substitutional and interstitial defect formation energies with respect to the size of the defect supercell.	75
4-3	Impurity-vacancy pairs in the α - V_2C structure: six in-plane pairs have indices 1–6 and out-of-plane pairs have indices 7–12.	78
4-4	Average in-plane and out-of-plane impurity-vacancy binding energies and distance from the ideal vanadium site for substitutional impurities $X = Fe, Ni, Ce, Nd$ and U in α - V_2C	80
4-5	MEPs for migration of Fe and Ni impurities for each of the six in-plane and six out-of-plane vanadium sites.	82
5-1	Zero-temperature stress-strain curves and sound speed curves calculated using the Cheng potential for Cu-Zr(-Al) and the Mendeleev potential for Cu-Zr.	87
5-2	MSDs for liquid and metallic glass and Cu-Cu RDFs for liquid and metallic glass.	90
5-3	Volume-temperature relationships during cooling for $Cu_{30}Zr_{70}$, $Cu_{50}Zr_{50}$ and $Cu_{70}Zr_{30}$ systems.	91
5-4	Shock wave profiles of shock pressure and shear stress from MD simulations of $Cu_{50}Zr_{50}$ metallic glass at $U_p = 0.125, 0.5$ and 1.5 km/s.	94
5-5	Shock pressure at the HEL P_{HEL} as a function of final shock pressure for $Cu_{30}Zr_{70}$, $Cu_{50}Zr_{50}$ and $Cu_{70}Zr_{30}$ metallic glass.	96
5-6	Shock pressure distributions at different times and positions for $Cu_{50}Zr_{50}$ metallic glass at $U_p = 1.5$ km/s and $U_p = 0.5$ km/s.	97
5-7	Shock velocity U_s as a function of piston velocity U_p for $Cu_{30}Zr_{70}$, $Cu_{50}Zr_{50}$ and $Cu_{70}Zr_{30}$ metallic glass.	99

5-8	Shock wave profiles at $t = 100$ ps for $\text{Cu}_{30}\text{Zr}_{70}$, $\text{Cu}_{50}\text{Zr}_{50}$ and $\text{Cu}_{70}\text{Zr}_{30}$ metallic glass samples at $U_p = 1.5$ km/s.....	101
5-9	Shock-induced temperatures as a function of shock pressure.....	102
5-10	Peak shear stress and flow stress as a function of the final shock pressure.	103
5-11	Cu-Cu RDFs in the aftershock flow of $\text{Cu}_{50}\text{Zr}_{50}$ metallic glass for four different shock intensities.	105
5-12	Shock pressure at the HEL P_{HEL} versus mean pressure P_m at the HEL.	106
6-1	Pressure P_{xx} and shear stress profiles at $t = 125$ ps for $\text{Cu}_{50}\text{Zr}_{50}$ metallic glass at different piston velocities.	115
6-2	Snapshots of von Mises shear strain for $\text{Cu}_{50}\text{Zr}_{50}$ metallic glass at different piston velocities.	116
6-3	Snapshot at $t = 40$ ps of von Mises shear strain η_i^{VM} and profiles of $\eta^{\text{VM}}(x)$ and shear stress for $\text{Cu}_{50}\text{Zr}_{50}$ and $U_p = 0.375$ km/s.....	118
6-4	Peak shear stress τ_{peak} as a function of the mean pressure P_m and flow stress τ_{flow} as a function of the final shock pressure P_{xx}	119
6-5	Snapshots of von Mises shear strain for $\text{Cu}_{30}\text{Zr}_{70}$, $\text{Cu}_{50}\text{Zr}_{50}$ and $\text{Cu}_{70}\text{Zr}_{30}$ metallic glasses at $P_{xx} = 20$ GPa.	121
6-6	Average von Mises shear strain in the quasi-steady flow state B behind the shock front as a function of the final shock pressure P_{xx}	122
6-7	Diffusivity as a function of shock pressure P_{xx} for Cu-Zr metallic glasses from this work and $\text{Cu}_{46}\text{Zr}_{54}$ metallic glass from Hugoniotat simulations.	123
6-8	Representative Cu-centered clusters corresponding to the given set of Voronoi indices.	125
6-9	Fraction of Cu-centered Voronoi polyhedra at the quasi-steady flow state behind the shock front as a function of the piston velocity U_p	126
6-10	Fraction of Cu-centered Voronoi polyhedra that have been transformed into other types after transitioning from the unshocked state to the quasi-steady flow state B behind the shock front.	128
7-1	Structure of the low-temperature phase of LaBGeO_5 from the side and from the top.	133
7-2	Structure of the LaO_9 polyhedra with attached GeO_4 (green) and BO_4 (blue) tetrahedra and without.....	135

7-3	Electronic band structure and DOS for the low-temperature phase of LaBGeO ₅ calculated using DFT.....	138
7-4	Phonon dispersion and DOS for the low-temperature phase of LaBGeO ₅ calculated using DFT.....	139
7-5	Structure of the high-temperature phase of LaBGeO ₅	140
7-6	Structure of the LaO ₉ polyhedron from the low-temperature phase of LaBGeO ₅ and the LaO ₁₀ polyhedron from the high-temperature phase.	142
7-7	Phonon dispersion and DOS for the high-temperature phase of LaBGeO ₅ calculated using DFT.....	144
7-8	Energy as a function of the relative displacement of atoms from the high-temperature phase of LaBGeO ₅ along the unstable phonon modes at the Γ , M and K points.....	145
7-9	MEP between the low-temperature (ferroelectric) and high-temperature (paraelectric) phases of LaBGeO ₅ , and magnitude of polarization along the c-axis at different points along the MEP.	146
7-10	Illustration of the rigid rotation of the BO ₄ tetrahedra occurring during the ferroelectric phase transition in LaBGeO ₅	149

LIST OF ABBREVIATIONS

CI-NEB	Climbing image nudged elastic band
DFT	Density functional theory
DOS	Density of states
EAM	Embedded atom method
FCCI	Fuel-cladding chemical interaction
GGA	Generalized gradient approximation
HEL	Hugoniot elastic limit
HNF	Hermite normal form
LAMMPS	Large-scale Atomic/Molecular Massively Parallel Simulator
LDA	Local density approximation
MEP	Minimum energy path
MG	Metallic glass
MSD	Mean square displacement
NN	Nearest neighbor
PAW	Plane augmented wave
PBE	Perdew-Burke-Ernzerhof
PES	Potential energy surface
RDF	Radial distribution function
SFR	Sodium fast reactor
SRO	Short-range order
STZ	Shear transformation zone
TST	Transition state theory
UFF	Universal force field
VASP	Vienna Ab Initio Simulation Package

Abstract of Dissertation Presented to the Graduate School
of the University of Florida in Partial Fulfillment of the
Requirements for the Degree of Doctor of Philosophy

TRANSPORT AND PHASE TRANSITIONS IN CERAMICS AND AMORPHOUS
METALS BY ATOMIC-LEVEL SIMULATION

By

Brian Demaske

December 2017

Chair: Simon R. Phillpot

Major: Materials Science and Engineering

Microscopic phenomena of diffusion, phase transitions and high-strain-rate mechanical behavior are investigated in ceramics and amorphous metals using atomic-scale simulation methods. The defect and diffusion behavior of V_2C is investigated using density functional theory calculations owing to its potential use as a diffusion barrier in nuclear fuel-cladding applications. Self-diffusion coefficients for carbon and vanadium are calculated using methods based on transition state theory and compared to existing experimental measurements. Dilute metal impurities are found to prefer substitutional vanadium sites over interstitial sites. Impurity-vacancy binding is found to increase with impurity size with the largest impurities forming clusters with neighboring vanadium vacancies.

Shock compression of Cu_xZr_{100-x} ($x = 30, 50$ and 70) metallic glasses is carried out over a wide range of shock intensities using molecular dynamics simulations. An elastic-plastic response characterized by a narrow elastic precursor and sluggish plastic shock wave is observed for all compositions. The Hugoniot elastic limit of the simulated metallic glasses is found to be strongly pressure-dependent, in contrast to crystalline metals. Yielding of the metallic glass occurs via nucleation of shear transformation

zones with a gradual shift towards homogeneous flow at high shock intensities. Local shear-resistance of the metallic glass is correlated with the degree of icosahedral order of Cu-centered clusters, which is found to increase with Cu content. The shock-induced melting transition is found to occur at higher shock pressures for samples with higher Cu content.

Ferroelectricity in LaBGeO₅ with stillwellite structure is investigated using density functional theory calculations. Phonon dispersion calculations of the high-temperature paraelectric phase reveal an unstable mode that is shown to drive the ferroelectric phase transition. The main feature of the ferroelectric distortion is a rigid rotation of BO₄ tetrahedra, which agrees with previous short-range potential calculations. A spontaneous polarization of 4.6 $\mu\text{C}/\text{cm}^2$ is calculated for LaBGeO₅ using the modern theory of polarization. This value lies within the experimental range of 2.7 – 12 $\mu\text{C}/\text{cm}^2$.

CHAPTER 1 INTRODUCTION

1.1 General Overview

On the smallest scales, the behavior of a material is ultimately determined from the interactions among its constituent atoms. The potential energy of a system comprised of N atoms is a $3N$ -dimensional function of the atomic coordinates. All possible sets of atomic coordinates, or simply configurations, make up the potential energy surface (PES) of a given system. Along the PES, there exist local minima that correspond to configurations of stable or quasi-stable structures, such as crystal phases, glasses or molecules. A transition from one distinct local potential energy minima to another occurs along a minimum energy path (MEP) of the PES that passes through a saddle point or transition state. At the transition state, the potential energy attains a local minimum in all but one dimension in which it attains a local maximum.

In addition to the potential energy, atoms in real materials also possess kinetic energy due primarily to thermal motion. At low temperatures, systems can only sample a small area of the PES around a local energy minimum. As the temperature is increased, however, the number of configurations that the system passes through increases, which gives it the ability to sample more of the PES. Occasionally, the system will overcome an energy barrier between two nearby energy minima by passing through a transition state. Together the height of the energy barrier and the temperature of the system dictate the rate of the process: lower barriers and higher temperatures correspond to faster processes.

Many phenomena, such as phase transitions, diffusion, chemical reactions, glass formation, structure prediction, etc., can be easily understood on the basis of the PES or

energy landscape paradigm. For example, the process of glass formation is the result of cooling a liquid at a rate that is faster than the competing crystallization rate [1]. While traversing the PES, the system becomes trapped in a local energy minimum corresponding to an amorphous or glassy configuration and due to insufficient thermal energy is unable to overcome the barrier to the lower energy crystalline state.

The idea of the energy landscape has proven extremely useful in atomic-scale simulations in which the configurations of and interactions among individual atoms are controlled and specified by the user. In this work, we use both static and dynamic simulation methods to study problems related to lattice diffusion, phase transitions and plastic deformation processes in ceramics and metals. Static simulation methods are used to search out energy minima on the PES to determine stable ordered crystalline structures of V_2C and transition state searches are conducted between neighboring energy minima to determine MEPs for diffusion. The dynamics of the ferroelectric phase transition in the stillwellite compound $LaBGeO_5$ are determined by characterizing the PES around a known transition state configuration. Dynamic methods are used to simulate the trajectories of atoms within a metallic glass (MG) under the action of high-strain-rate shock compression. MGs correspond to quasi-stable energy minima along the PES. Plastic deformation in MGs has been shown to be a thermally-activated process whereby a small cluster of atoms undergoes a collective shear motion in response to an applied shear stress [2].

1.2 Motivation of Problems

1.2.1 Vanadium Carbide Diffusion Barrier

Nuclear fuel rods consist of fuel pellets encased within a metallic tube, or cladding. During operation, the gap between the fuel and cladding closes and

components of the fuel, including fission products, and cladding can diffuse into one another forming an interaction layer [3–6]. This process is known as fuel-cladding chemical interaction (FCCI) and can result in the formation of brittle or low-melting point phases that thin the cladding wall and make it susceptible to failure. Next generation nuclear reactors, such as sodium-cooled fast reactors (SFRs), are being developed that enable higher fuel burn-ups and better thermal efficiency when compared to current generation reactors. In SFR designs, U-Zr or U-Pu-Zr metallic alloys represent typical fuels and ferritic/martensitic steels represent typical cladding materials [7]. The metal-metal interface can exacerbate FCCI in contrast to the metal-oxide interface present in previous generation reactors. Moreover, the high service temperatures and irradiation levels in SFRs can also act to further enhance FCCI [8–11], so new methods are being sought to reduce the interdiffusion of fuel and cladding components.

Recently, vanadium has emerged as a promising candidate material to act as a diffusion barrier between the fuel and cladding [12–14]. To ensure there is good bonding between the diffusion barrier and cladding, a pack cementation diffusion coating (PCDC) process was developed to deposit vanadium on HT-9 steel [15], a potential candidate cladding material in design of SFRs [7]. Decarburization of the steel during the PCDC process leads to the formation of a thin layer with nearly V_2C stoichiometry. Out-of-pile diffusion couple experiments between Ce, acting as a fuel surrogate, and HT-9 steel with and without the V_2C coating layer were performed, and it was found that the interdiffusion layer is effectively eliminated when the vanadium coating is present [15].

The kinetics of diffusion in V_2C is largely unknown. Most of the available experimental diffusion data has been obtained for carbon self-diffusion in the cubic transition metal carbides [16–26]. Self-diffusion data on metal atom self-diffusion is rare [27,28] and experiments on impurity diffusion are nonexistent. Moreover, little theoretical work has been done to address lattice diffusion in the transition metal carbides. The goal of Chapters 3 and 4 of this work is to characterize the diffusion behavior of intrinsic defects and impurities in V_2C . Self-diffusion of vanadium and carbon will be treated in Chapter 3 guided by available experimental results for self-diffusion in the cubic transition metal carbides. Chapter 4 will proceed to address the behavior of impurities in V_2C , specifically addressing those impurities originating in nuclear fuel and steel cladding materials. Calculations are performed using density functional theory (DFT) as it has proven effectiveness in accurately describing self-diffusion and impurity diffusion in metals [29–38] and can treat a wide variety of impurity types at no added cost.

1.2.2 High-strain-rate Deformation of Metallic Glasses

In terms of mechanical properties, MGs outperform crystalline alloys in yield strength, elastic strain limits and energy storage [2,39–49]. Their superior performance is grounded in their amorphous structure, which leads to a fundamentally different plastic deformation mechanism than the dislocation-mediated plastic response of metallic crystals. Quasistatic compression and tension experiments at room temperature have shown that plastic deformation in MGs occurs inhomogeneously through the nucleation and growth of shear bands [44,2,46–48,50]. Under tension, only a single dominant shear band may be activated resulting in catastrophic failure of the MG with little to no macroscopic plasticity. However, under constrained loading

geometries, like uniaxial compression or bending, serrated flow is observed and some macroscopic plasticity ($\sim 1\%$ plastic strain) is achieved before failure. The serrated flow corresponds to emission of localized shear bands in a step-by-step manner.

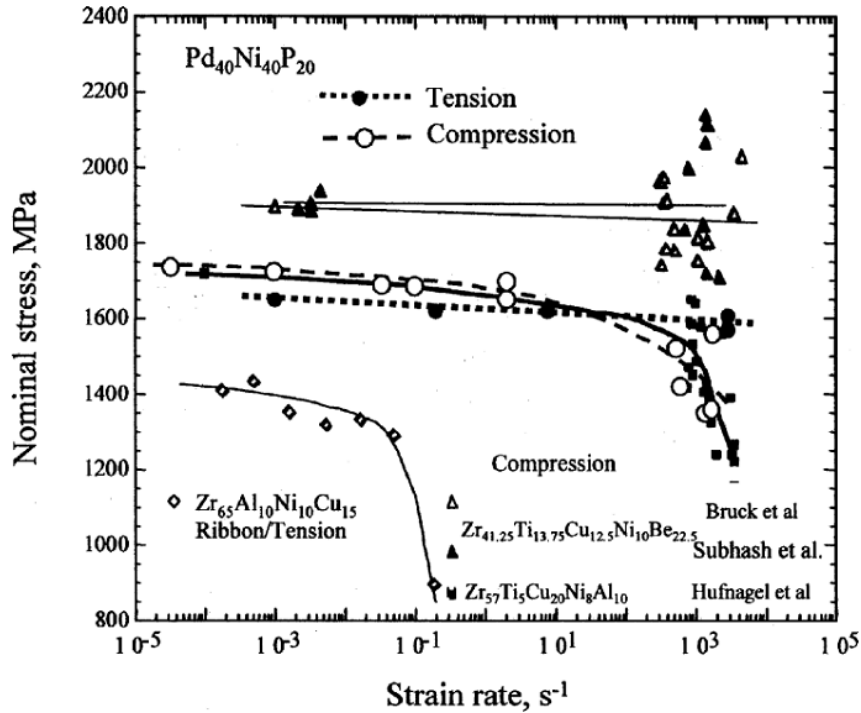


Figure 1-1. Dependence of fracture strength on strain rate for several metallic glasses. Reprinted from [51] with permission from Elsevier.

Less is known about the deformation behavior of MGs under dynamic loading conditions. The fracture strengths of several representative MGs under uniaxial stress conditions are shown in Fig. 1-1 for a range of strain rates from 10^{-4} to 10^4 s⁻¹. The bulk (> 1 mm thickness) MGs were found to exhibit rate independent behavior or a slightly negative response with increasing strain rate. At the highest strain rates, the fracture surfaces of the bulk MG samples are rough due to simultaneous operation of multiple shear bands [2,47,51,52]. The large drop in strength for the Zr₆₅Al₁₀Ni₁₀Cu₁₅ MG ribbon (0.05 mm) is presumed to be due to surface effects. Although there is some agreement

among the different studies, the effect of strain rate on the yield behavior of MGs has not been shown definitively.

Shock waves have long been used as a tool to measure the strength of materials at very high strain rates ($> 10^5 \text{ s}^{-1}$) [53–55]. In experiments, high-velocity projectiles or laser pulses are used to generate shock waves, which propagate through the target at supersonic velocities. Material entering the shock is rapidly compressed along the shock wave propagation direction. Such compression results in a state of uniaxial *strain* within the sample, whereas the results discussed above were obtained for uniaxial *stress* states. If the amplitude of the shock wave exceeds the Hugoniot elastic limit (HEL), then the material begins to yield. Shock compression experiments have been performed on several MGs [56–66]. However, due to the high speed of the shock wave, experimentalists are limited in their ability to obtain thermodynamic or microstructural information *in situ*. Time-resolved X-ray diffraction measurements have been useful in analyzing shock deformation in crystals [67–71], but have yet to be applied to MGs.

Molecular dynamics (MD) simulations have been used to study shock deformation in many different types of materials [72–93]. Results of these simulations have provided insights into the microscopic deformation behavior of single- and nanocrystalline metals [75,83,87–89,94] as well as resolved fine details of shock wave structure [78,85,86]. In contrast to experiments, MD simulations provide the complete atomic-scale dynamics of the system starting from the initial loading event to reflection of the shock at the opposite surface. Chapters 5 and 6 of this work will characterize the shock response of Cu-Zr MGs using MD simulations. Specific focus will be placed on the thermodynamic response of the MG as well as changes to the microstructure that

occur during shock compression. Such simulations will provide insights into the behavior of MGs under shock loading as well as the microscopic plastic deformation mechanism at high strain rates.

1.2.3 Lanthanum Borogermanate Glass-ceramics

The lanthanum borogermanate $\text{La}_2\text{O}_3\text{-B}_2\text{O}_3\text{-GeO}_2$ system has good glass-forming ability [95]. When subjected to heat treatment, some glass compositions undergo monophasic crystallization into LaBGeO_5 [95–97], which is isomorphous with stillwellite CeBSiO_5 . At room temperature, LaBGeO_5 is ferroelectric [98–102] and, when doped with Nd^{3+} or Pr^{3+} , LaBGeO_5 can be used as a self-frequency doubling laser [103,104]. Surface and bulk crystallization of lanthanum borogermanate glasses can be achieved through various heat treatment processes. By adjusting the temperature and duration of the heat treatment, it is possible to generate transparent glass-ceramic composites with nanometer-sized crystallites of LaBGeO_5 [105–109]. Such transparent glass-ceramic nanocomposites have applications in optoelectronics, integrated optics, photonics and communication technologies due to the nonlinear optical properties of the embedded LaBGeO_5 crystals.

In addition to the heat treatment method discussed above, it has been shown that crystallization of lanthanum borogermanate glasses is also possible through focused laser irradiation [110–115]. Heating of the glass by a pulsed femtosecond laser leads to localized melting of the glass and formation of a LaBGeO_5 seed crystal at the melt-glass interface. By continuously moving the sample during laser irradiation, crystalline tracks can be grown within the bulk or on the surface of the glass. Moreover, provided the bending angles along a track are gradual, the orientation of the crystal varies continuously through the bend without forming grain boundaries [111].

Interestingly, the polar axis of the LaBGeO₅ crystal aligns with the direction of the laser writing. Recently, it has been shown that these crystalline tracks can function as waveguides with second-harmonic generation properties [115].

The Curie temperature for LaBGeO₅ is ~530°C [98,99]. Below this temperature, LaBGeO₅ attains a nonzero spontaneous polarization along the *c*-axis that can be reversed under an electric field. Measurements of the spontaneous polarization at room temperature have a range of 2.7-12 μC/cm² [98–102]. Neutron diffraction data show continuous variation of the cell volume through the temperature range 200-700°C [116], which is evidence for the second-order nature of the phase transition at 530°C. Subsequent experimental measurements [117] and force-field modelling [118] of the vibrational properties of LaBGeO₅ found the ferroelectric phase transition is dominated by rotation of BO₄ tetrahedra. However, the lattice dynamics of the ferroelectric phase transition could not be conclusively shown from these works. Chapter 7 of this work will use accurate DFT calculations to characterize the low- and high-temperature phases of LaBGeO₅ and to determine the complete lattice dynamics of the ferroelectric phase transition. From these results, the spontaneous polarization of ferroelectric phase is calculated within the framework of the modern theory of polarization [119–123].

1.3 Outline

This dissertation is organized as follows. In Chapter 2, brief overviews of DFT and MD are given emphasizing their specific applications to the calculations performed in this work. In Chapters 3 and 4, the DFT calculations of the energetics and diffusion behavior of intrinsic defects and select impurities in V₂C are presented. The focus of Chapter 3 is on the intrinsic defect and self-diffusion behavior. Self-diffusion coefficients are calculated under the assumptions of a vacancy-assisted mechanism for vanadium

and an interstitial mechanism for carbon. In Chapter 4, the site preference and impurity-vacancy binding energies are determined for select impurity types as a first step towards characterizing the impurity diffusion behavior. Impurity types considered are Fe and Ni, U and Ce and Nd, which represent major components of the clad, nuclear fuel and fission products, respectively. Migration barriers are calculated for the two smallest impurities, Fe and Ni. In Chapters 5 and 6, MD simulations of shock compression of Cu-Zr MGs are presented. The focus of Chapter 5 is on the shock wave structure, Hugoniot states and yield criterion. In Chapter 6, the microstructural changes of the MGs during shock loading are investigated with emphasis on the influence of short-range order (SRO) on the plastic deformation behavior. In both Chapters 5 and 6, the composition of the MG is varied to determine its effect on the shock response. In Chapter 7, DFT calculations of the ferroelectric phase transition and spontaneous polarization in LaBGeO_5 are presented. A collected summary of results and ideas for future work are given in Chapter 8.

CHAPTER 2 OVERVIEW OF SIMULATION METHODS

Defect and diffusion behavior in V_2C as well as the ferroelectric phase transition and spontaneous polarization in $LaBGeO_5$ will be investigated using first-principles DFT calculations. Shock compression of Cu_xZr_{100-x} MGs will be simulated using MD.

2.1 Density Functional Theory

DFT can treat upwards of a thousand atoms with routine calculations being performed on systems with several tens to a few hundred atoms. Such small system sizes preclude direct calculation of diffusion coefficients in solids, because of the long time and finite temperatures needed to sample diffusive processes. Fortunately, diffusion problems can be readily addressed via static DFT calculations using ideas from transition state theory (TST) [124]. To use TST methods, the diffusion mechanism must be known ahead of time, i.e., the initial and final states of the diffusing atom must be known. As such, only simple diffusion problems can be addressed in this way. A method for calculation of diffusion coefficients in simple crystal structures using DFT is given in Ref. [125]. Macroscopic polarization can also be treated within the framework of DFT owing to the development of the modern theory of polarization [119–123].

DFT is a reformulation of nonrelativistic quantum mechanics in the language of density functionals. The foundation of DFT is the two Hohenberg-Kohn theorems [126]. The first theorem states that the external potential v_{ext} of an N -electron system is a unique functional of the ground state electron density n_0 . By implication, all other observables, including the total energy, are functionals of n_0 . The second theorem states that $E[n_0] \leq E[n']$, where n' is some other density satisfying the necessary boundary conditions. Thus, the ground state energy can be obtained by minimizing

$E[n']$. Kohn and Sham showed that the minimization problem can be mapped to a set of single particle Schrödinger-like equations, known as the Kohn-Sham equations [127]

$$\left[-\frac{\hbar^2 \nabla^2}{2m} + v_{ext}(\mathbf{r}) + v_H(\mathbf{r}) + v_{xc}(\mathbf{r}) \right] \phi_i(\mathbf{r}) = \varepsilon_i \phi_i(\mathbf{r}), \quad (2-1)$$

where ϕ_i are the single particle orbitals of the non-interacting system. The Hartree potential $v_H = e^2 \int \frac{n(\mathbf{r}')}{|\mathbf{r}-\mathbf{r}'|} d^3r'$ represents the Coulomb repulsion between particles. All non-classical interactions are contained in the exchange-correlation potential $v_{xc} = \delta E_{xc}[n]/\delta n$.

The exact form of the exchange-correlation functional $E_{xc}[n]$ is unknown, so approximations must be made. The two most common approximations used in the study of condensed matter systems are the local density approximation (LDA) and the generalized gradient approximation (GGA). In the LDA, $E_{xc}^{LDA}[n] = \int e_{xc}^{hom}(n(\mathbf{r})) d^3r$, where $e_{xc}^{hom}(n)$ is the exchange-correlation energy of a homogeneous electron gas of density n . The GGA expands on the LDA by including the gradient of the electron density ∇n within the calculation of $E_{xc}^{GGA} = \int f(n, \nabla n) d^3r$. There are many different variants of GGA depending on the form of $f(n, \nabla n)$. In addition to the Perdew-Zunger parameterization of the LDA [128], this work uses the Perdew-Burke-Ernzerhof (PBE) form of the GGA [129] and a variant designed specifically for solids, PBEsol [130].

With an appropriate expression for v_{xc} , the Kohn-Sham equations can then be solved self-consistently to determine n_0 and, hence, the ground state energy. Note that given the exact form of v_{xc} , the charge density $n = \sum_i |\phi_i|^2$ is equal to n_0 for the true N -electron system. In practice, ϕ_i are expressed in terms of either localized (atomic-like) basis sets, like Gaussians, or delocalized basis sets, like plane waves. DFT codes, such

as VASP [131], that use plane-wave basis sets are particularly well-suited to solve problems in periodic systems, which is one of the main reasons for their popularity among researchers in condensed matter physics and materials science. In DFT applications, v_{ext} is specified from the positions of atoms or nuclei, which are assumed to remain fixed when solving for the electronic ground state. In a nutshell, this is the Born-Oppenheimer or adiabatic approximation. Once the electronic ground state is obtained self-consistently, interatomic forces and stresses can be obtained via the Hellman-Feynman theorem. By minimizing the interatomic forces and stresses in the cell, one can calculate the equilibrium structure of the system. In addition, by considering finite changes in atom positions and/or cell vectors, one can also calculate elastic constants, phonons and other aspects of the PES, as well as a range of other properties.

2.2 Modern Theory of Polarization

With the advent of the modern theory of polarization [119–123], calculation of the macroscopic polarization is now a standard feature of most DFT codes. According to the theory, the macroscopic polarization of a 3D periodic system with a volume Ω is a multivalued quantity defined modulo a vector $\mathbf{P}_i = \frac{1}{\Omega} e\mathbf{R}_i$ known as the polarization quantum, where e is the electronic charge and \mathbf{R}_i ($i = 1, 2, 3$) is a lattice vector. As a consequence, the polarization for a given system is not uniquely defined, but is instead represented by a lattice of values with spacing given by \mathbf{P}_i [132]. Moreover, even nonpolar systems can exhibit nonzero polarization equal to $\pm n\mathbf{P}_i$ or $(\frac{1}{2} \pm n)\mathbf{P}_i$, where n is an integer [132]. Different values of n correspond to different branches within the polarization lattice. The spontaneous polarization of a ferroelectric is defined as the

polarization difference between a polar system and a reference nonpolar system or, equivalently, as one-half the polarization difference between two polar systems with enantiomorphous structures [122]. In practical calculations of the spontaneous polarization, it is useful to calculate the polarization at several points along a continuous transformation path between these two systems to ensure that the two end structures reside on the same branch of the polarization lattice.

2.3 Molecular Dynamics

Material entering a shock front is compressed uniaxially at very high strain rates, which leads to heating and stress generation. For moderate shocks, i.e., those that occur in most materials applications, the temperatures and stresses are low enough to safely ignore electronic effects. Because of the high strain rates involved in shock compression of solids, it is necessary to explicitly treat interactions among individual atoms to understand how the material will respond near the shock front. Thus, MD has become the natural choice for simulating shock waves in solids [72–93].

In MD simulation, the classical equations of motion are solved numerically to yield the trajectories for a system of N interacting particles, usually atoms. Given a set of boundary and initial conditions, positions $\mathbf{r}_i(t = 0)$ and velocities $\mathbf{v}_i(t = 0)$, particle trajectories are updated after a time step Δt using a finite difference algorithm. There are many choices of algorithms, Verlet [133], velocity Verlet [134], predictor-corrector [135], etc. In this work, the velocity Verlet algorithm is used, in which the position and velocity of a particle at time $t + \Delta t$ are given by

$$\begin{aligned}\mathbf{r}_i(t + \Delta t) &= \mathbf{r}_i(t) + \mathbf{v}_i(t)\Delta t + \frac{1}{2}\mathbf{a}_i(t)\Delta t^2 \\ \mathbf{v}_i(t + \Delta t) &= \mathbf{v}_i(t) + \frac{1}{2}(\mathbf{a}_i(t) + \mathbf{a}_i(t + \Delta t))\Delta t,\end{aligned}\tag{2-2}$$

where \mathbf{a}_i is the acceleration. From Newton's second law, the acceleration of each particle is proportional to the net force acting on it $\mathbf{F}_i = m_i \mathbf{a}_i = -\nabla_{\mathbf{r}_i} U(\mathbf{r}_1, \mathbf{r}_2, \dots, \mathbf{r}_N)$, where U is the potential energy function, or interatomic potential, of the system and m_i is the particle's mass. After the positions and velocities of all particles have been updated using Eq. 2-2, the simulation time is advanced $t = t + \Delta t$ and the process is repeated for the next time step.

During an MD run, properties for individual particles can be calculated using relations from statistical mechanics. For example, the instantaneous temperature $T = \frac{1}{3Nk_B} \sum_i m_i \mathbf{v}_i^2$ for a particle with three degrees of freedom. By performing averages over a group of particles or a series of time steps or both, one can extract thermodynamic properties of the system, such as kinetic and potential energies, temperature, pressure tensor, flow velocity, density, etc. Other information about the system can be determined by monitoring trajectories, like the mean square displacement (MSD) or atomic strain tensor, or by looking at the local environments around particles, like radial distribution functions (RDFs) or Voronoi polyhedra.

Proper solutions to the Newton's equations of motion will conserve the total energy (E), volume (V) and number of particles (N) in the system. Such simulations correspond to the NVE or microcanonical ensemble. It is possible to modify the equations of motion to simulate other thermodynamic ensembles. Some of the most common ensembles used in MD simulations, other than NVE , are the isochoric canonical ensemble (NVT) and the isobaric canonical ensemble (NPT). In this work, both the NVE and NPT ensembles are used. In the NPT ensemble, the temperature and pressure of the system are controlled by a thermostat and barostat, respectively. The

NPT calculations in this work are performed using a Nosé-Hoover thermostat [136–138] and Parrinello-Rahman barostat [139]. MD simulations presented in this work are performed using LAMMPS [140].

The interatomic potential U determines the forces on particles and, therefore, the dynamics of the system under study. In *ab initio* MD, the potential is supplied directly from electronic structure calculations, like DFT. However, after each time step, the potential must be recalculated as the atoms move and the external potential v_{ext} changes. Therefore, *ab initio* MD is computationally demanding and is limited to small systems (~1-1000 atoms) and short time durations (~1-100 ps). In contrast, in classical MD electronic degrees of freedom are not treated explicitly and the interatomic potential is fixed ahead of time, which allows for much larger system sizes and longer simulation times. The disadvantage is that the potential must be carefully chosen for the problem at hand with no guarantee of transferability. Many types of potentials exist for many different types of systems that range in complexity from simple pair potentials, like Lennard-Jones [141], to complex reactive force fields, like ReaxFF [142].

2.4 Embedded Atom Method

The MD simulations in this work are concerned with metallic alloys, specifically Cu-Zr MGs. Perhaps the most widely-used and successful approaches to modeling interatomic potentials in metals is the embedded atom method (EAM) [143,144]. The potential energy in the EAM formalism is given by

$$U = \sum_{i < j} V_{s_i s_j}(r_{ij}) + \sum_i F_{s_i}(\bar{\rho}_i), \quad (2-3)$$

where $V_{s_i s_j}$ is a pair potential between atom types s_i and s_j and F_{s_i} is an embedding energy for atom i . The charge density at site i is $\bar{\rho}_i = \sum_{j \neq i} \rho_{s_j}(r_{ij})$, where ρ_{s_j} is the charge density associated with atom j . In the original derivation, ρ is a measure of the local electron density of each atom and F represents the energy associated with placing an atom in a region with electron density $\bar{\rho}$. The pair potential V represents short-range interactions between cores. However, most current implementations treat each of the terms in Eq. 2-3 as fitting functions and the potential is fit to a database comprising experimental and *ab initio* data [145]. The success of EAM potentials lie in their ability to accurately model metallic bonding through the many-body embedding term $F(\rho)$.

CHAPTER 3 INTRINSIC DEFECTS AND SELF-DIFFUSION IN VANADIUM CARBIDE¹

3.1 Background

Transition metal carbides exhibit a combination of excellent mechanical and thermal properties, such as high hardness, high melting temperature, good wear resistance and high thermal conductivity [146–148]. These properties combined with the success of vanadium metal as a cladding liner for nuclear fuel rods [12,149] have sparked interest in the use of vanadium carbide as a diffusion barrier to help mitigate FCCI in next generation nuclear reactors [15]. Using Ce as a stand-in for the metallic fuel and fission products, diffusion couple experiments were performed at 660°C (933 K) for 100 hours on HT9 steel with and without the vanadium carbide coating [15]. Results indicate an almost complete elimination of the interdiffusion layer when the vanadium carbide coating is present.

The coating process used in Ref. [15] results in the formation of a vanadium carbide layer having close to V_2C stoichiometry. According to existing phase diagrams [150–152], a disordered β - V_2C_y phase is stable at high temperatures and is characterized by a hexagonal vanadium sublattice with carbon atoms randomly occupying $y/2$ of the available octahedral sites. Ordering of the carbon atoms occurs at lower temperatures resulting in the formation of two ordered phases, α - V_2C and β' - V_2C . Of these two phases, α - V_2C is the experimental ground state structure. The order-disorder transition temperature between α - V_2C and β - V_2C_y is estimated to be in the range of 1100-1600 K [152], though the exact temperature is unknown.

¹The work described in this chapter has been published in B.J. Demaske, A. Chernatynskiy, and S.R. Phillpot, J. Phys: Condens. Matt. 29, 245403 (2017).

Self-diffusion of carbon in cubic transition metal carbides with NaCl-type structure has been investigated experimentally for NbC [20], ZrC [17,18], TiC [16,17,22] and V_6C_5 [24], whereas metal atom self-diffusion has been characterized only in NbC_x [27] and TiC_x [28]. Experimental diffusion studies on transition metal carbides with non-NaCl-type structures are scarce with only a few studies on WC [153], Mo_2C [21] and Fe_3C [154]. Furthermore, experiments have yet to address the diffusion of impurities in any of the transition metal carbides, including V_2C . From a theoretical perspective, only basic studies of the structural, electronic and elastic properties of V_2C have been performed [155–157]. No work has yet been done to address the diffusion of intrinsic defects or impurities in V_2C . The objective of the following two chapters will be to investigate intrinsic defects and impurities in V_2C using first-principles DFT calculations. This chapter will address the intrinsic defect behavior and self-diffusion of carbon and vanadium, while Chapter 4 will address the energetics and kinetics of dilute metal impurities representative of the fuel-clad system.

Self-diffusion experiments on the transition metal carbides found that metal atom diffusivity is independent of carbon concentration, whereas carbon diffusivity is not. Therefore, it can be inferred from these results that carbon and metal atom diffusion processes are uncorrelated. Researchers have postulated the most likely self-diffusion mechanisms in NaCl-type M_xC_y , including (1) the direct migration of an atom to a nearest-neighbor (NN) vacant site and (2) a two-jump sequence in which the migrating atom temporarily occupies a tetrahedral site before advancing to a NN vacant site. The first mechanism is thought to occur primarily for metal atoms [27,28], while the second

mechanism is thought to occur for carbon [20,24]. The self-diffusion behavior of binary transition metal carbides has been summarized in Refs. [18] and [158].

This chapter will begin to fill the gap in understanding self-diffusion in non-cubic transition metal carbides from a theoretical perspective using V_2C as a case study owing to its potential use as a cladding liner in nuclear fuel rods. Expected application temperatures are low enough such that carbon ordering is likely. Therefore, the focus is on ordered V_2C structures. An exhaustive search of different possible ordered structures up to a certain specified volume and satisfying the hexagonal symmetry of the vanadium sublattice is conducted to determine the lowest-energy configurations maintaining V_2C stoichiometry. Equilibrium structural, electronic and elastic properties of representative V_2C structures are calculated and compared to existing experimental and theoretical data prior to intrinsic defect and self-diffusion calculations. Predicted carbon self-diffusion coefficients, diffusion prefactors and activation energies are compared to available experiments for the disordered cubic phases of V_6C_5 [24] and $NbC_{0.868}$ [20], while theoretical results for vanadium self-diffusion are compared to available experiments for self-diffusion of Nb in NbC_x [27] and Ti in TiC_x [28]. Experimental diffusion data is measured for single-crystals over the temperature range 2000-2500 K.

3.2 Simulation Methods

The equilibrium structural, electronic and elastic properties and intrinsic defect energetics and self-diffusion coefficients of V_2C are calculated using VASP [131,159], which employs the plane augmented wave (PAW) method to simplify treatment of core electrons [160,161]. In our calculations, 4 electrons for C ($2s^22p^2$) and 13 electrons for V ($3p^63d^84s^2$) are treated as valence. For comparison purposes, both the PBE form of the GGA [129] and the Perdew-Zunger parameterization of the LDA [128] are used to

approximate the exchange-correlation functional. Γ -centered Monkhorst-Pack k -point meshes for each supercell are generated using the fully automatic scheme implemented in VASP in which the number of subdivisions in the k -point mesh N_i along a reciprocal lattice vector \vec{b}_i is determined according to

$$N_i = \max(1, l \times |\vec{b}_i| + 0.5), \quad (3-1)$$

where l is a parameter that can be varied to change the density of the k -point mesh.

A plane-wave energy cutoff of 600 eV and k -point mesh with $l = 30$ are found to give energies converged to within 5 meV/atom. Very fine k -point meshes with $l = 60$ are used in calculations of the electronic density of states (DOS) and strings of k -points along major directions in the Brillouin zone are used in calculations of the electronic band structure. Wave function optimization is truncated when the energy difference between successive electronic steps drops below 10^{-6} eV. Partial orbital occupancies are treated using the method of Methfessel-Paxton (1st order) with a smearing width of 0.2 eV. Structure relaxation calculations are carried out using the conjugate gradient algorithm [162] until the maximum force on each atom is < 0.01 eV/Å and the maximum stress component on the cell is < 0.01 eV/Ω, where Ω is the cell volume.

The ordered structures, described in the first section of the Simulation Results, have different cell shapes and volumes. To test the convergence of the total energies of the ordered structures with respect to number of k -points, the k -point mesh is systematically increased from $9 \times 9 \times 9$ to $17 \times 17 \times 17$, where a uniform mesh is used instead of the automatic scheme outlined above. The use of the uniform mesh is preferred as the lattice vectors and, hence, reciprocal lattice vectors vary from structure to structure, which would lead to different k -point meshes for different structures using

the automatic generation scheme. The ordered structures are first relaxed to equilibrium and then additional static calculations are performed using the linear tetrahedron method with Blöchl corrections [163] to obtain total energies. Upon increasing the size of the k -point mesh from $13 \times 13 \times 13$ to $15 \times 15 \times 15$, the maximum change in the relative energies for all ordered structures drops below 0.25 meV.

Equilibrium elastic constants are calculated by considering both finite distortions of the cell with rigid ions [164] and contributions from ion relaxation [165]. The plane-wave energy cutoff and size of the k -point mesh are systematically increased to test convergence of the elastic constants, where a uniform k -point mesh is used instead of the automatic generation scheme as VASP changes the k -point set on-the-fly when deforming the cell. Use of the automatic scheme may cause changes in the k -point mesh due to the finite deformations of the cell lattice vectors, which can lead to inaccuracies in the calculated elastic constants. Above a plane-wave energy cutoff of 1050 eV and a $11 \times 11 \times 11$ k -point mesh, individual elastic constants are found to vary by < 0.5 GPa. Analysis of the elastic constant matrices is performed using the ELATE software package [166]. Dynamical matrices are obtained using the finite-displacement method implemented in the software package Phonopy [167] with VASP as the force calculator. Migration barriers for self-diffusion are calculated using the climbing image nudged elastic band (CI-NEB) method [168,169] with a force tolerance of 0.01 eV/Å. By varying the number of intermediate images used in the CI-NEB calculations, we find that the transition states do not change appreciably beyond five images for vanadium atom migration and seven images for carbon atom migration.

3.3 Simulation Results

3.3.1 Ordered Structures of V₂C

According to X-ray diffraction studies of nearly stoichiometric V₂C [150,152,170], at low temperatures V₂C forms two ordered phases: a hexagonal β' phase (space group $P\bar{3}1m$) stable under carbon-deficient conditions and an orthorhombic α phase (space group $Pbcn$) stable below 1100 – 1600 K. In the β' phase, the vanadium atoms are arranged on a hexagonal lattice while the α phase has a small ~1.1% distortion of the hexagonal lattice. The two phases differ predominantly in the ordering of carbon atoms. Calculated equilibrium properties for the two experimentally-observed ordered phases are given in Table 3-1. Indeed, the α phase is lower in energy than the β' phase in our DFT calculations, confirming experimental results.

To see how the arrangement of carbon atoms influences the total energy, we perform an exhaustive search over all possible configurations of superstructures of volume n that can be generated from the base 4-site hexagonal cell (space group $P6_3/mmc$), see Fig. 3-1, where n is a multiple of the base cell volume. In Fig. 3-1, large (red) spheres represent vanadium atoms and small (gray) spheres represent octahedral sites. Superstructures are generated using the Hermite normal form (HNF) routines found in the AFLOW software package [171]. Details of superstructure generation using HNF matrices can be found in Ref. [172]. The symmetry-unique superstructures of the base cell are shown in Fig. 3-1 in order of increasing volume. For each superstructure, all configurations satisfying the V₂C stoichiometry are enumerated by placing carbons at half of the octahedral sites, e.g. a superstructure containing m octahedral sites has $\binom{m}{m/2}$ configurations. The energy of each configuration is then calculated using the

universal force field (UFF) method [173]. The process is repeated for n from 1 to 8, generating a total of 495,542 configurations. Note that both the α and β' phases of V_2C were among the structures generated for $n = 4(8)$ and $n = 3(6)$, respectively. Duplicate configurations with the same UFF energy are removed and only 110 configurations with the lowest energies are retained for structural relaxation using VASP.

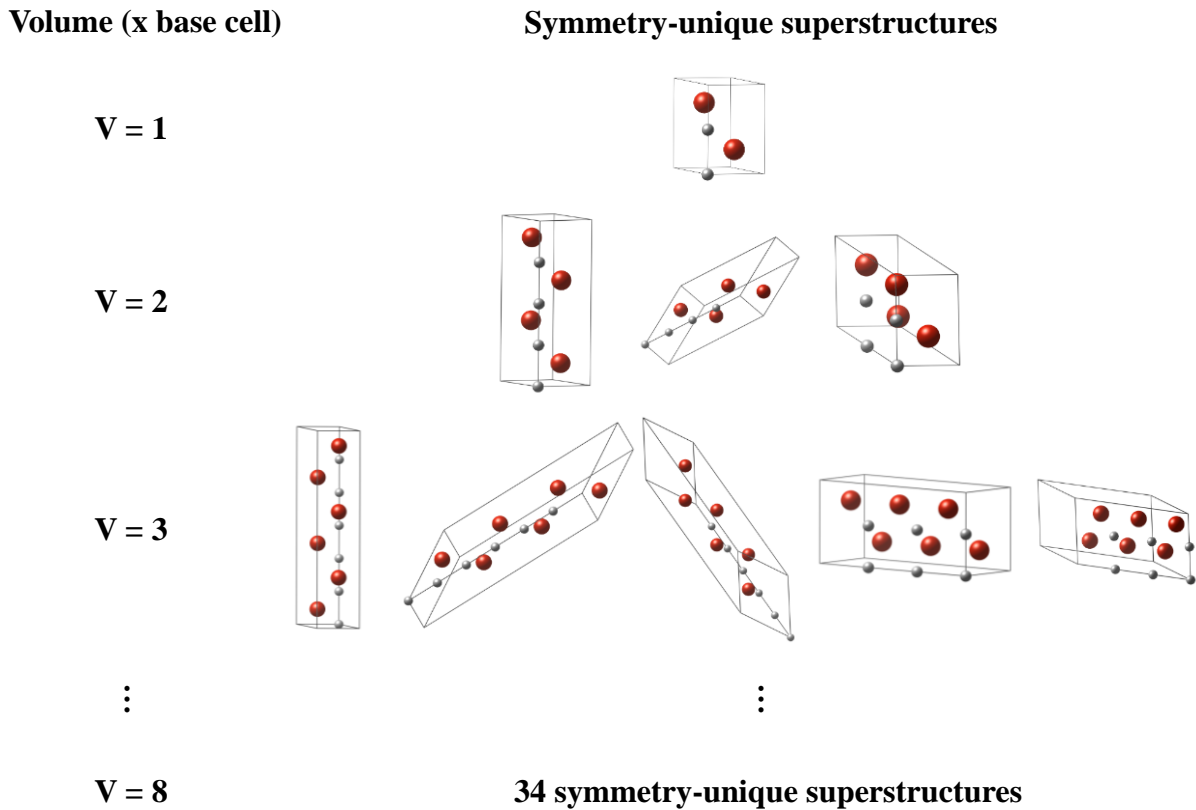


Figure 3-1. Symmetry-unique superstructures generated from a 4-site hexagonal cell (space group $P6_3/mmc$) in order of increasing volume.

Table 3-1. Lattice constants and cohesive energies for the α and β' phases of V_2C and the low-energy structure belonging to space group $Pn\bar{m}$ (see Fig. 3-1).

Space group (phase)	$Pn\bar{m}$			$Pbcn$ (α)			$P\bar{3}1m$ (β')	
Lattice type	orthorhombic			orthorhombic			hexagonal	
Prototype	<i>anti</i> CaCl ₂			ζ -Fe ₂ N			ϵ -Fe ₂ N	
a (Å)	4.534	4.549	4.540	4.495	4.551	4.570	5.008	5.005
b (Å)	5.039	5.735	5.726	5.628	5.735	5.742	-	-
c (Å)	2.864	5.031	5.031	4.929	5.032	5.026	4.536	4.551
E_0 (eV/atom)	-9.5565	-9.5554	-	-	-	-	-9.5496	-
E_{ZP} (meV/atom)	72.9	72.6	-	-	-	-	72.6	-
Reference	This work (VASP-PBE)	This work (VASP-PBE)	VASP-PBE Ref. [174]	CASTEP Ref. [155]	CASTEP Ref. [156]	Expt. Ref. [175]	This work (VASP-PBE)	Expt. Ref. [176]

Note: theoretical results obtained at zero temperature

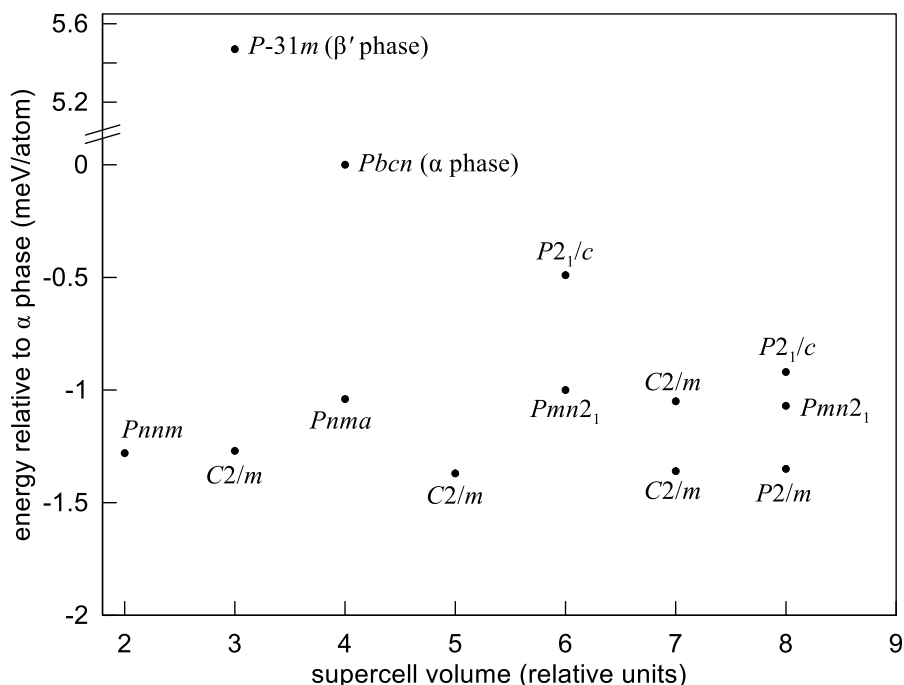


Figure 3-2. Energies for a subset of low-energy V_2C structures enumerated from derivative superstructures with volumes ≤ 8 times the volume of the base 4-site hexagonal cell.

It turns out that the experimental ground state structure of V_2C , namely the α phase, does not correspond to the lowest energy structure in our DFT calculations. Instead, there are several ordered V_2C structures that are $\sim 0-2$ meV/atom lower in energy, see Fig. 3-2. Note energies in Fig. 3-2 are given relative to the α phase (space group $Pbcn$). The low-energy structures share the feature that no carbon atoms sit directly atop one another in adjacent planes perpendicular to the c -axis, as is the case for the α and β' phases. The structures with the lowest energies for each supercell volume possess linear chains of carbon atoms perpendicular to the c -axis. Such chains are arranged parallel to one another forming a pattern in which the length of the motif increases with the volume of the structure. The simplest of these structures has a motif length of two, belongs to the orthorhombic space group $Pnnm$ and has a volume twice that of the base hexagonal cell, see Fig. 3-3(a). The energy of the $Pnnm$ structure is

~1.3 meV/atom less than that of the α phase. Local environments, out to 2nd nearest neighbors (NNs), of the larger structures with longer motifs are very similar to that of the $Pn\bar{m}$ structure. Therefore, we expect the self-diffusion behavior of these structures to be similar as well. In addition to the α and β' phases of V_2C , the low-energy $Pn\bar{m}$ structure is included in our subsequent calculations and discussion. The unit cells for these three structures are shown in Fig. 3-3. In the figure, vanadium atoms are shown as large (red) spheres and carbon atoms as small (brown) spheres. Note that the β' phase is unique in that the density of carbon planes perpendicular to the c -axis alternates between a low and high value, whereas this density is constant for the two orthorhombic structures.

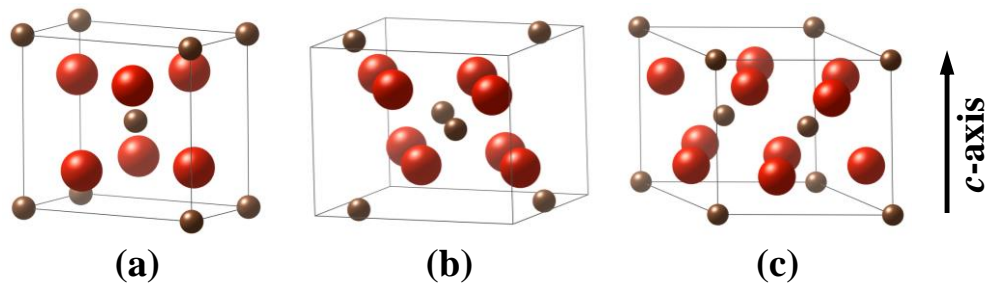


Figure 3-3. Unit cells of three ordered V_2C structures including (a) the low-energy orthorhombic structure belonging to space group $Pn\bar{m}$, (b) the α phase and (c) the β' phase.

Zero-temperature lattice constants for the low-energy orthorhombic structure and the α and β' phases of V_2C calculated using the GGA-PBE functional are given in Table 3-1. Available experimental and other theoretical values for the α phase and experimental values for the β' phase are also shown. To the best of our knowledge, no other theoretical work has examined the β' phase. The equilibrium lattice parameters for the α and β' phases of V_2C calculated using the GGA-PBE functional are in excellent

agreement with experiment, while those obtained using the LDA functional underestimate experiment by ~2%. Therefore, the GGA-PBE functional is used for all calculations presented in the remainder of this chapter.

3.3.2 Electronic and Elastic Properties of V_2C

The calculated electronic band structure and DOS for the α phase of V_2C at zero temperature are shown in Fig. 3-4. Band energies are given relative to the Fermi energy, which is set to zero. The absence of a band gap is in agreement with the experimental fact that early transition metal carbides are good electrical conductors [147]. Both electronic band structures and DOS for the β' phase and the Pnm structure exhibit similar features to those shown for the α phase. Atom-projected DOS calculations show that states near the Fermi level are predominantly associated with vanadium atoms. Since all three ordered V_2C structures share an almost identical vanadium sublattice, it is not surprising that their electronic structures are similar. Small differences can be attributed to the differing arrangements of carbon atoms.

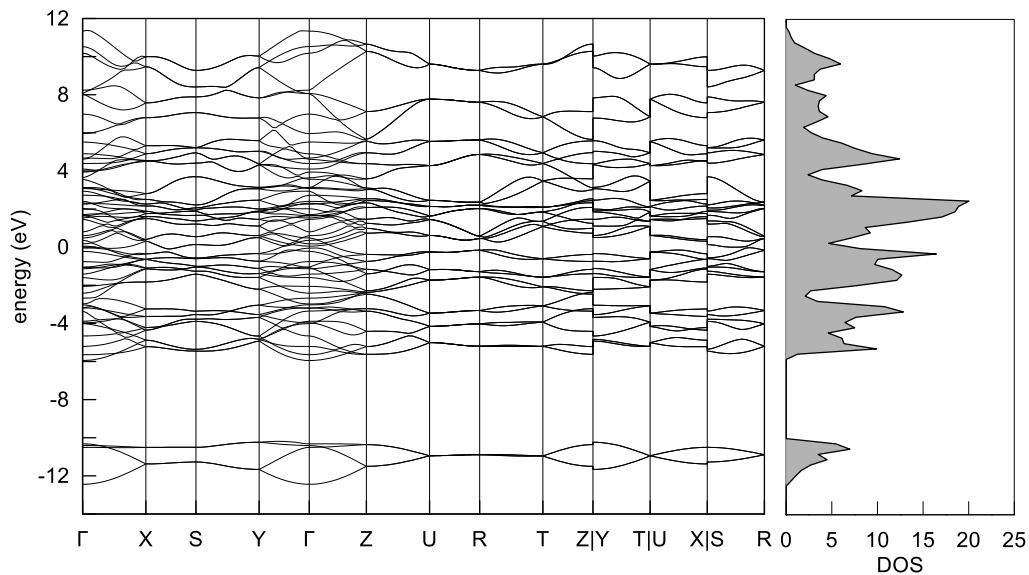


Figure 3-4. Electronic band structure and DOS for the α phase of V_2C from DFT calculations.

Table 3-2. Zero-temperature elastic constants and elastic moduli for the three ordered V₂C structures.

Space group (phase)	<i>Pn</i> nm		<i>Pbc</i> n (α)		<i>P</i> 31m (β')	
c_{11} (GPa)	406	384	381	450	383	418
c_{22} (GPa)	425	415	410	493	414	418
c_{33} (GPa)	434	404	393	452	400	431
c_{12} (GPa)	150	188	189	205	189	176
c_{13} (GPa)	116	182	181	207	182	148
c_{23} (GPa)	161	124	122	146	120	148
c_{44} (GPa)	85	107	107	122	110	131
c_{55} (GPa)	153	128	125	143	130	131
c_{66} (GPa)	95	136	131	161	135	121
K (GPa)	235	243	250	279	242	246
G (GPa)	119	120	118	140	121	130
E (GPa)	305	309	303	359	311	331
ν	0.284	0.288	0.290	0.290	0.286	0.277
Reference	This work (VASP-PBE)	This work (VASP-PBE)	VASP-PBE Ref. [174]	CASTEP-PBE Ref. [155]	CASTEP-PBE Ref. [156]	This work (VASP-PBE)

Elastic constants for the three different V₂C structures are given in Table 3-2.

There are no experimental measurements of single-crystal elastic constants for either the α or β' phases. The elastic constants for the α phase calculated in Refs. [174] and [156] are within 2% of those calculated in this work, while those of Ref. [155] are significantly higher overall. This difference may be due to the use of norm-conserving pseudopotentials in Ref. [155], while our calculations and those of Ref. [174] use PAW pseudopotentials. It is not clear what type of pseudopotentials were used in the

calculations of Ref. [156]. No published theoretical results could be found for the β' phase. All values are obtained for zero temperature.

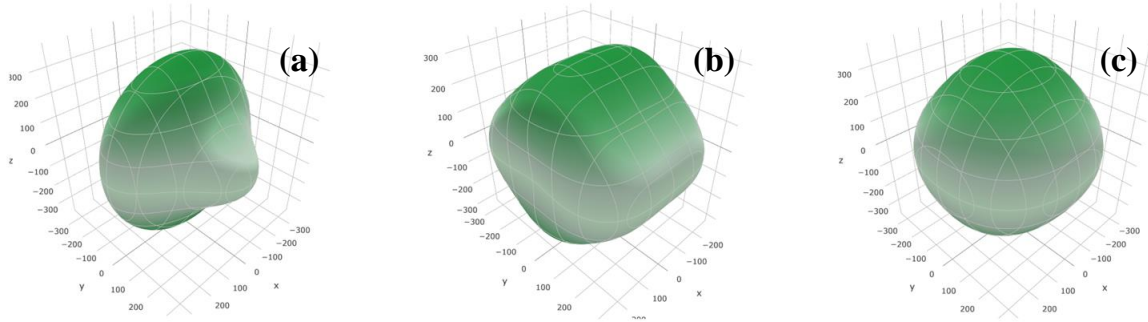


Figure 3-5. Spatial variation in of the Young's modulus E for (a) low-energy orthorhombic structure belonging to space group $Pn\bar{m}$, (b) a phase of V_2C and (c) β' phase of V_2C .

The bulk modulus K and shear modulus G for the aggregate V_2C crystal are estimated from the elastic constants using the Voigt-Reuss-Hill approximation [177]. The Young's modulus E and Poisson ratio ν are then calculated from the well-known relations: $\frac{1}{E} = \frac{1}{3G} + \frac{1}{9K}$ and $\nu = \frac{1}{2} \left(1 - \frac{3G}{3K+G} \right)$. Elastic moduli from our DFT calculations for all three V_2C structures as well as from other theoretical works are given in Table 3-2. Overall the three V_2C structures exhibit elastic moduli that differ by $< 10\%$, which indicates their average elastic response is similar and only weakly influenced by carbon ordering. However, the two orthorhombic structures exhibit greater anisotropy of E , G and ν along different spatial directions compared to the β' phase, which has a nearly isotropic elastic response. To illustrate this, a 3D plot of E is shown in Fig. 3-5 for each of the three V_2C structures, where the distance from the center to the surface of each shape corresponds to E in that specific direction. More spherical shapes correspond to more isotropic elastic behavior. It is clear from the figure that E for the β' phase is nearly

isotropic, whereas the other two structures exhibit more anisotropy. Similar behavior is observed for G and ν (plots not shown).

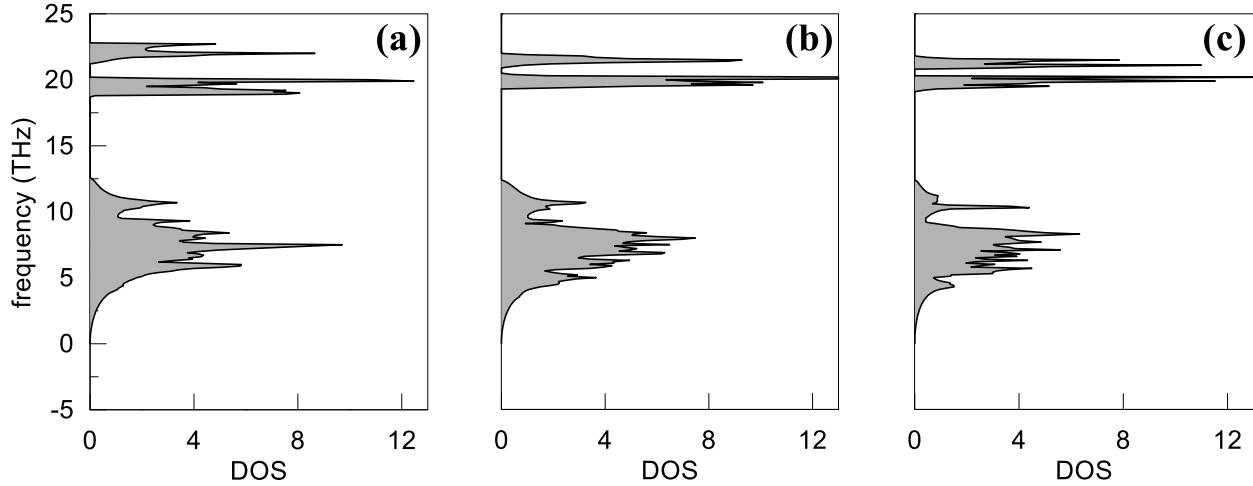


Figure 3-6. Theoretical phonon DOS for the (a) low-energy orthorhombic structure belonging to space group $Pnmm$, (b) the α phase of V_2C and (c) the β' phase of V_2C .

Figure 3-6 shows the theoretical phonon DOS for all three of the ordered V_2C structures calculated using the relaxed lattice parameters in Table 3-1. Each of the phonon DOS decays to zero as the frequency approaches zero indicating no unstable modes. Therefore, the three ordered V_2C structures are mechanically stable. Zero-point vibrational energy corrections to the total energy are given by

$$E_{ZP} = \int_0^{\infty} g(\omega) \frac{\hbar\omega}{2} d\omega, \quad (3-2)$$

where $g(\omega)$ is the normalized phonon DOS [178]. The zero-point correction to the cohesive energies for each of the three V_2C structures are given in Table 3-1. The three structures give values of E_{ZP} that are the same to within 1 meV/atom. Therefore, the $Pnmm$ structure remains the lowest-energy V_2C structure, though the energy difference with the α phase is small (< 1 meV/atom).

3.3.3 Vacancy Formation Energies

As a first step towards investigating the self-diffusion behavior of V_2C , we calculated the formation energies of intrinsic defects most likely to aid in diffusion. The formation energy at zero-temperature for a neutral defect X is given by [179–182]

$$\Delta E_f[X] = E[X] - E[\text{bulk}] + \sum_j n_j \mu_j, \quad (3-3)$$

where $E[X]$ is the total energy of the cell with the defect, $E[\text{bulk}]$ is the total energy of the perfect cell, n_j is the number of atoms of chemical species j that are removed ($n_j > 0$) or added ($n_j < 0$) to the cell and μ_j is the energy of the atomic reservoir to which the atom is removed or added. In this work, μ_j is taken to be the cohesive energy per atom of either *bcc* vanadium or carbon graphite.

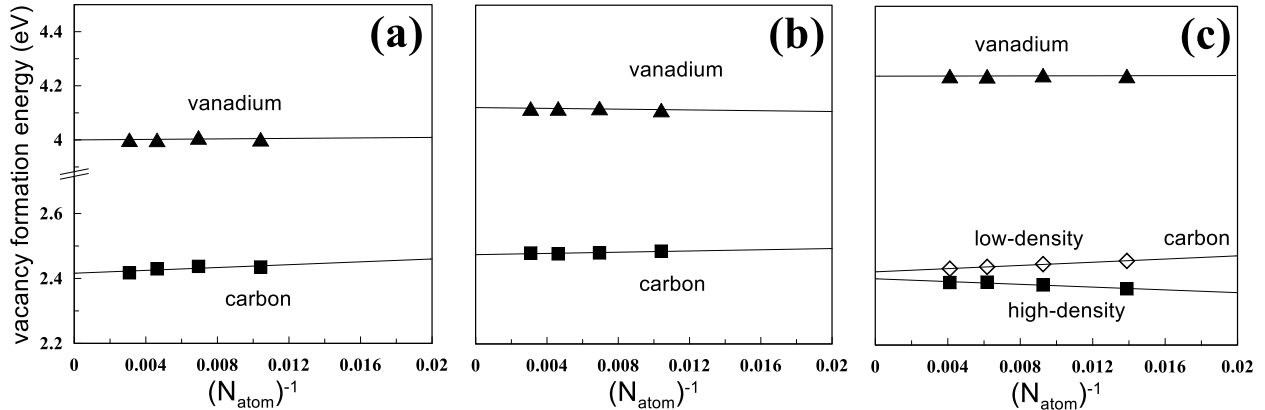


Figure 3-7. Calculated vacancy formation energies as a function of the number of atoms in the supercell for the (a) low-energy structure belonging to space group $Pn\bar{m}$, (b) the α phase of V_2C and (c) the β' phase of V_2C .

Since the self-diffusion of vanadium and carbon are assumed to occur separately on their respective sublattices, the only relevant defects to consider are vacancies.

Figure 3-7 shows the convergence of the carbon and vanadium vacancy formation

energies with respect to supercell size for the each of the three V₂C structures. The vacancy formation energies listed in Table 3-3 are found by extrapolating linear fits of the calculated formation energies as $N^{-1} \rightarrow 0$. For the β' phase, we denote the carbon lying in the high-density plane as C' and the carbon lying in the low-density plane as C. In the limit $N^{-1} \rightarrow 0$, $\Delta E_f[v_C]$ and $\Delta E_f[v_{C'}]$ differ by ~ 0.03 eV.

Table 3-3. Vacancy formation energies ΔE_f and vibrational formation entropies ΔS_f^{vib} for the three ordered V₂C structures calculated using DFT.

Space group (phase)	<i>Pnmm</i>	<i>Pbcn</i> (α)	<i>P31m</i> (β)
$\Delta E_f[v_C]$ (eV)	2.42	2.48	2.43
$\Delta E_f[v_{C'}]$ (eV)	-	-	2.40
$\Delta E_f[v_V]$ (eV)	4.00	4.08	4.24
$\Delta S_f^{vib}[v_V]$ (k)	5.00	5.53	4.97

Creation of a vanadium vacancy requires breaking bonds with 12 NN vanadium atoms, whereas creation of a carbon vacancy requires breaking bonds with only 6 NN vanadium atoms. Therefore, more energy is required to create a vanadium vacancy than a carbon vacancy and $\Delta E_f[v_V] > \Delta E_f[v_C]$. Carbon vacancy formation energies for the three different ordered structures are within 0.1 eV of each other, which is reflective of their nearly identical vanadium sublattices. Vanadium vacancy formation energies are also similar across structures, which indicates that the carbon arrangement has only a small effect on the overall bonding strength. To the best of our knowledge, no other theoretical calculations or experimental measurements of the vacancy formation energies have been performed for V₂C or any of the other vanadium carbides.

3.3.4 Energy Barriers for Self-diffusion

3.3.4.1 Vanadium self-diffusion

Ignoring the small distortions in the two orthorhombic structures, the vanadium atoms in V_2C form an *hcp* sublattice. It is assumed that vanadium self-diffusion occurs exclusively on the vanadium sublattice by a standard vacancy-assisted mechanism. This assumption is based on experimental evidence that the metal atom diffusivity in transition metal carbides is independent of carbon concentration. Considering only the first NN shell, a vanadium may either migrate within its own basal plane (jump A) or into one of the two adjacent planes (jump B) as shown in Fig. 3-8. In the figure, vanadium atoms are shown as large (red) spheres, while octahedral sites are shown as small (brown) spheres. In V_2C , only half of the octahedral sites are occupied by carbon atoms. The in-plane D_{\perp} and out-of-plane D_{\parallel} self-diffusion coefficients for vacancy-mediated diffusion are given by

$$D_{\perp} = \frac{1}{4} C_v \left(f_{Ax} \sum_i v_i^* \exp\left(-\frac{\Delta E_{A,i}^m}{kT}\right) d_{\perp,i}^2 + f_{Bx} \sum_j v_j^* \exp\left(-\frac{\Delta E_{B,j}^m}{kT}\right) d_{\perp,j}^2 \right) \quad (3-4)$$

$$D_{\parallel} = \frac{1}{2} C_v f_{Bz} \sum_i v_i^* \exp\left(-\frac{\Delta E_{B,i}^m}{kT}\right) d_{\parallel,i}^2,$$

where C_v is the concentration of thermal vacancies on the vanadium sublattice, v_i^* are the effective frequencies, $\Delta E_{A,i}^m$ and $\Delta E_{B,i}^m$ are the vacancy migration energies for jumps of type A and B, respectively, $d_{\perp,i}^2$ and $d_{\parallel,i}^2$ are the in-plane and out-of-plane squared displacements and f 's are the correlation factors. The subscripts i and j denote the index of the migrating atom. In the expression for D_{\perp} , the sum in i is over the six NN vanadium atoms within the basal plane of the vacancy and the sum in j is over the six NN

vanadium atoms in the two adjacent basal planes. In the expression for D_{\parallel} , the sum is taken over only the six NN vanadium atoms in the two adjacent basal planes; jumps within a basal plane do not contribute to D_{\parallel} .

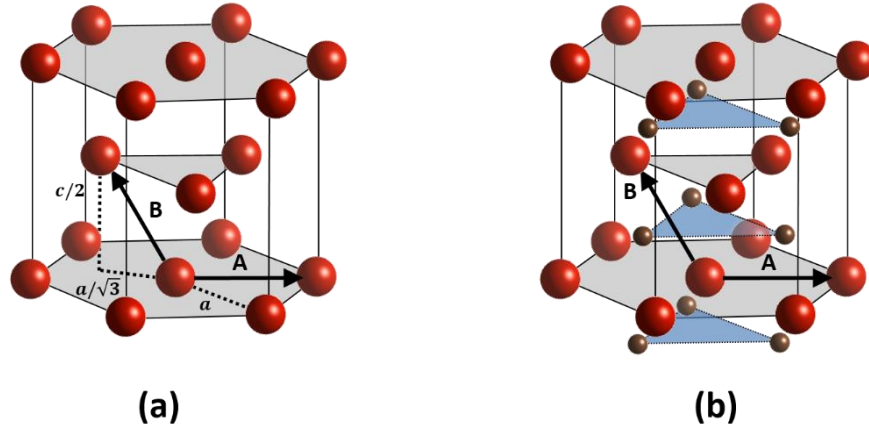


Figure 3-8. In-plane (A) and out-of-plane (B) jumps for vanadium to a nearest-neighbor site within the vanadium sublattice (a) without octahedral sites shown and (b) with octahedral sites shown.

The concentration of vacancies on the vanadium sublattice follows an Arrhenius dependence $C_v = \exp[-\Delta G_f/kT]$. Contributions from lattice vibrations to the free energy are treated in the harmonic approximation. The vibrational entropy of a harmonic solid of N atoms is given by

$$S^{vib} = k \int_0^{\infty} g(\omega) \left\{ \frac{\hbar\omega}{kT} \left[\exp\left(\frac{\hbar\omega}{kT}\right) - 1 \right]^{-1} - \ln \left[1 - \exp\left(-\frac{\hbar\omega}{kT}\right) \right] \right\} d\omega, \quad (3-5)$$

where $g(\omega)$ is the normalized phonon DOS at zero temperature [183]. The expression for ΔS_f^{vib} is analogous to Eq. 3-3 for ΔE_f and requires calculating $g(\omega)$ for three systems: perfect V_2C , the same system with a single vanadium vacancy and *bcc* vanadium. The supercell sizes used in the force constant calculations are $2 \times 2 \times 4$ (96

atoms) for the $Pn\bar{m}$ structure, $2 \times 2 \times 2$ (96 atoms) for the α phase and $2 \times 2 \times 2$ (72 atoms) for the β' phase. A $3 \times 3 \times 3$ conventional supercell is used in the force constant calculation for bcc vanadium. A uniform Γ -centered $25 \times 25 \times 25$ mesh of phonon wave vectors is used to sample the dynamical matrices, which are solved to get $g(\omega)$ for each system. The integration in Eq. 3-5 is then carried out to get the vibrational entropy S^{vib} . Calculated values of ΔS_f^{vib} for the three structures are given in Table 3-3. The free energy of vacancy formation considering only harmonic contributions from phonons is given by $\Delta G_f = \Delta E_f - T\Delta S_f^{vib}$.

Migration energy is defined as $\Delta E^m = E^{TS} - E^{IS}$, where E^{TS} is the energy of the saddle point along the MEP between the two end states and E^{IS} is the energy of the initial state. For the vacancy mechanism considered here, the initial state corresponds to a supercell with a single vanadium vacancy, while the final state corresponds to one of the 12 NN vanadium atoms moved to the vacancy site. CI-NEB calculations are performed on a set of interpolated structures for each of the 12 initial and final state pairs. We find that migration energies converge rapidly with respect to supercell size. A 71-atom supercell for the β' phase and 95-atom supercells for the two orthorhombic structures give ΔE^m converged to within 0.05 eV. MEPs for the six in-plane and six out-of-plane migration paths for the α phase of V_2C are shown in Fig. 3-9(a) and 3-9(b), respectively.

Three distinct groups of MEPs are observed for the out-of-plane B jumps shown in Fig. 3-9(b). The same grouping is also seen for the β' phase and the $Pn\bar{m}$ structure whose MEPs are not shown. For the α phase, in-plane migration energies ΔE_A^m are found to vary by 0.2 eV, while out-of-plane migration energies ΔE_B^m vary by as much as

2.6 eV. The large variation in ΔE_B^m is attributed to the vanadium atom having to pass through an intervening plane of carbon atoms during its jump to an adjacent basal plane; see the Discussion for more details. The other two V_2C structures show similar variation in ΔE_A^m , whereas the variation in ΔE_B^m for the $Pn\bar{m}$ structure (3.6 eV) is ~ 1 eV more than either the β' phase (2.7 eV) or the α phase (2.6 eV). This difference is attributed to differences in carbon atom arrangements among the structures and will be expanded upon in the Discussion. Table 3-4 gives calculated values for ΔE_A^m and ΔE_B^m for each of the six possible jumps of types A and B.

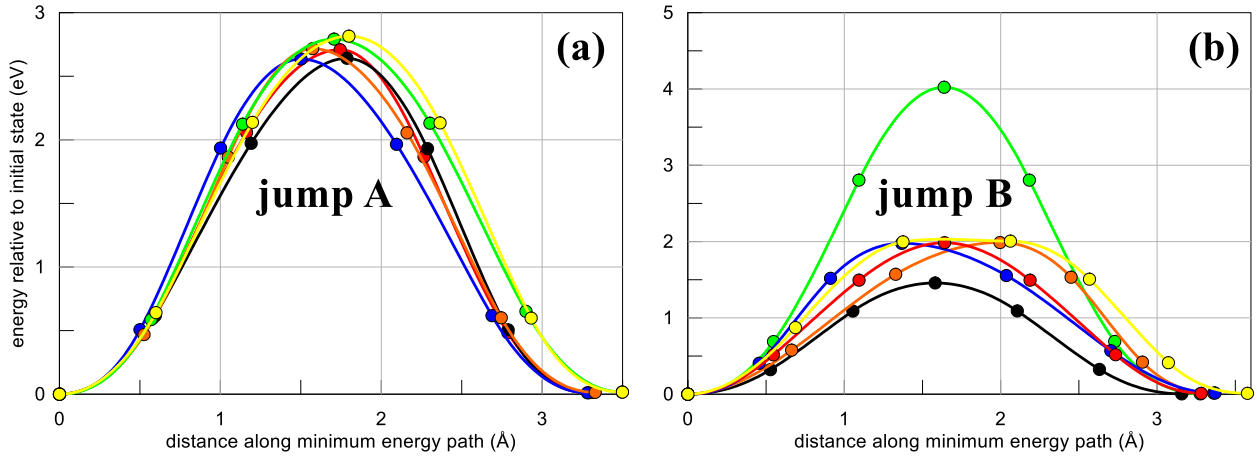


Figure 3-9. Theoretical MEPs for vanadium vacancy migration for (a) in-plane (jump A) and (b) out-of-plane (jump B) migration for the α phase from CI-NEB calculations.

The effective frequencies ν^* for an N-atom system are calculated from

$$\nu^* = \prod_{i=1}^{3N-3} \omega_i / \prod_{j=1}^{3N-4} \omega'_j, \quad (3-6)$$

where the ω_i and ω'_j are the normal mode frequencies for the initial and transition states, respectively [29,30,37]. The product over the transition state frequencies is reduced by one relative to the initial state due to an imaginary mode along the migration

direction. We approximate the normal mode frequencies for the entire system by those of the migrating atom only. This is the Einstein (independent oscillator) approximation. Eq. 3-6 simplifies greatly as the migrating atom contributes only three normal modes to the initial state and two modes to the transition state; the third mode of the transition state is imaginary and does not enter Eq. 3-6. The ν^* are calculated for each of the 12 MEPs determined by the CI-NEB calculations. We use a supercell with the same dimensions as was used in the calculation of ΔS_f^{vib} and ΔE^m . The calculated ranges for ν^* for both A and B jumps are given in Table 3-4.

Table 3-4. Migration energies ΔE_A^m and ΔE_B^m and effective frequencies ν^* for the vacancy-assisted vanadium self-diffusion mechanism for the three ordered V_2C structures calculated using DFT.

Space group (phase)	<i>Pnmm</i>	<i>Pbcn</i> (α)	<i>P31m</i> (γ)
ΔE_A^m (eV)	2.69	2.64	2.76
	2.69	2.64	2.76
	2.85	2.71	2.85
	2.85	2.72	2.85
	2.85	2.79	2.87
	2.85	2.82	2.87
ΔE_B^m (eV)	1.24	1.46	1.59
	2.09	1.98	1.59
	2.09	1.99	1.69
	2.10	1.99	2.10
	2.10	2.01	2.10
ν_A^* (THz)	4.84	4.02	4.34
	9.3-10.0	8.3-10.5	8.2-10.9
ν_B^* (THz)	5.6-12.8	5.7-10.9	5.4-10.6

The correlation factors f for vacancy-assisted self-diffusion in an *hcp* lattice have been calculated elsewhere [184] and are a function of the ratios of in-plane and out-of-plane jump frequencies $w_A = v_A^* \exp(-\Delta E_A^m/kT)$ and $w_B = v_B^* \exp(-\Delta E_B^m/kT)$, respectively. Table 3-5 gives correlation factors over a temperature range of 1000 – 3000 K calculated using the average jump frequencies $\overline{w_A}$ and $\overline{w_B}$ for vanadium self-diffusion in the β' phase of V_2C . The differences between f_{Bx} and f_{Bz} are negligible for the range of jump frequencies considered. The correlation factors for the other two structures are calculated in the same way and we obtain values nearly identical to those given in Table 3-5 for the β' phase. This is expected as the average in-plane and out-of-plane migration barriers and effective frequencies are similar for all three V_2C structures.

Table 3-5. Correlation factors for vacancy-assisted self-diffusion in an *hcp* lattice taken from Ref. [184] calculated using values of w_A/w_B obtained for vanadium self-diffusion in the β' phase of V_2C .

T (K)	w_A/w_B	f_{Ax}	f_{Bx} (f_{Bz})
1000	0.0050	0.9214	0.6475
1200	0.0123	0.9197	0.6490
1400	0.0233	0.9171	0.6514
1600	0.0378	0.9138	0.6546
1800	0.0549	0.9097	0.6584
2000	0.0740	0.9052	0.6628
2200	0.0946	0.9004	0.6674
2400	0.1160	0.8955	0.6722
2600	0.1379	0.8906	0.6770
2800	0.1598	0.8857	0.6817
3000	0.1817	0.8810	0.6863

In-plane and out-of-plane self-diffusion coefficients D_{\perp} and D_{\parallel} for vanadium are calculated by plugging in the values of $\Delta E_f[v_V]$, $\Delta S_f^{vib}[v_V]$, ΔE_A^m , ΔE_B^m , v_A^* and v_B^* listed in Tables 3-3 and 3-4 into Eq. 3-4. The self-diffusion coefficients are then fit to an Arrhenius expression of the form $D = D_0 \exp(-Q/kT)$. Activation energies Q and diffusion prefactors D_0 from these fits are given in Table 3-6 for each of the three ordered V_2C structures. Experimental values for Q and D_0 for metal atom self-diffusion in cubic NbC_x and TiC_x are also given for comparison. Overall, there is good agreement between the calculated activation energies and that measured in self-diffusion experiments for Nb in NbC_x , while the experimental activation energy for self-diffusion of Ti in TiC_x is significantly higher. Calculated diffusion prefactors underestimate experimental results by an order of magnitude. This is not surprising as first-principles studies of self-diffusion in *hcp* metals [33,37] also observed a similar underestimation in their calculated diffusion prefactors.

Table 3-6. Activation energies Q and diffusion prefactors D_0 for vacancy-assisted vanadium self-diffusion for the three ordered V_2C structures calculated using DFT.

	This work (<i>Pnnm</i>)	This work (α phase)	This work (β' phase)	Nb in NbC_x (Expt. Ref. [27])	Ti in TiC_x (Expt. Ref. [28])
Q_{\perp} (kcal/mol)	121.4	129.3	139.6	140.0 ± 2.4	176.4 ± 3.6
Q_{\parallel} (kcal/mol)	121.2	128.9	139.5		
$D_{0,\perp}$ (cm ² /s)	0.089	0.223	0.238	$4.54_{-1.75}^{+2.85}$	$4.36_{-2.34}^{+5.02}$
$D_{0,\parallel}$ (cm ² /s)	0.383	0.812	0.852		

3.3.4.2 Carbon self-diffusion

In each of the V_2C structures, carbon atoms fill half of the available octahedral interstitial sites, while the other half are empty. Because the concentration of such

structural vacancies dwarfs the concentration of thermal vacancies, we expect carbon self-diffusion to occur through migration of carbon atoms to empty NN octahedral sites. Together the octahedral interstitial sites form a simple hexagonal lattice (ignoring the small distortions for the two orthorhombic structures). Coordination polyhedra for the octahedral and tetragonal interstitial sites are shown in Fig. 3-10. Carbon atoms are surrounded by brown octahedra, while empty octahedral sites are surrounded by blue octahedra. Tetrahedral sites are surrounded by white tetrahedra. Octahedral sites share faces with neighboring octahedral sites in adjacent basal planes, but share edges with neighboring octahedral sites within the same basal plane. Tetrahedral sites share faces with neighboring octahedral sites within the same basal plane.

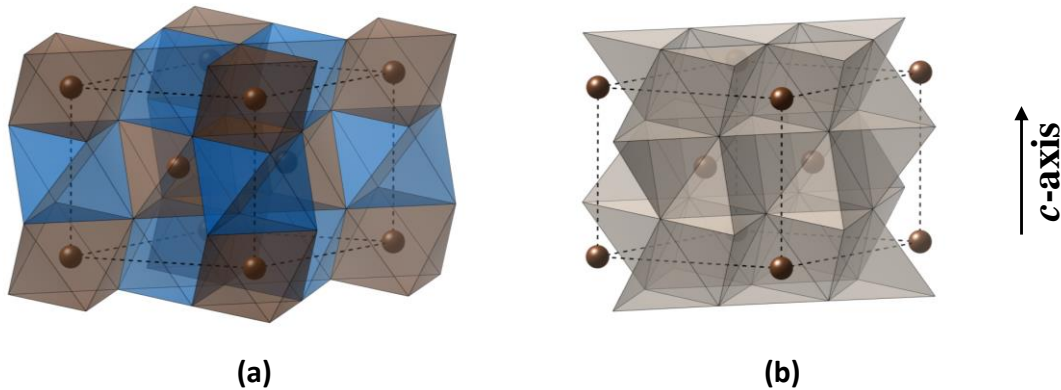


Figure 3-10. Coordination polyhedra for the (a) octahedral and (b) tetrahedral interstitial sites in V_2C .

It has been argued that in close-packed structures migrating atoms will pass through faces of connecting polyhedra rather than edges due to the larger effective “window” provided by the faces [185,186]. In light of this, an octahedral-tetrahedral-octahedral (O-T-O) mechanism was proposed [20,24] in which the migrating interstitial atom temporarily occupies a NN tetrahedral site before advancing to an empty

octahedral site within the same basal plane. However, to the best of our knowledge, no direct evidence for the carbon self-diffusion mechanism has been given for V_2C . Therefore, we consider a direct octahedral-octahedral (O-O) mechanism in addition to the O-T-O mechanism in our DFT calculations. Between basal planes the octahedral sites share faces and so a direct O-O jump mechanism is almost certain. In total, we consider two O-O and one O-T-O jumps: an O-O jump within the same basal plane (jump A), an O-O jump from one basal plane to another (jump B) and an O-T-O jump in which the two octahedral sites share the same basal plane (jump C). These jumps are shown in Fig. 3-11. In the figure, vanadium atoms are shown as large (red) spheres, octahedral sites as medium-sized (brown) spheres and tetrahedral sites as small (white) spheres.

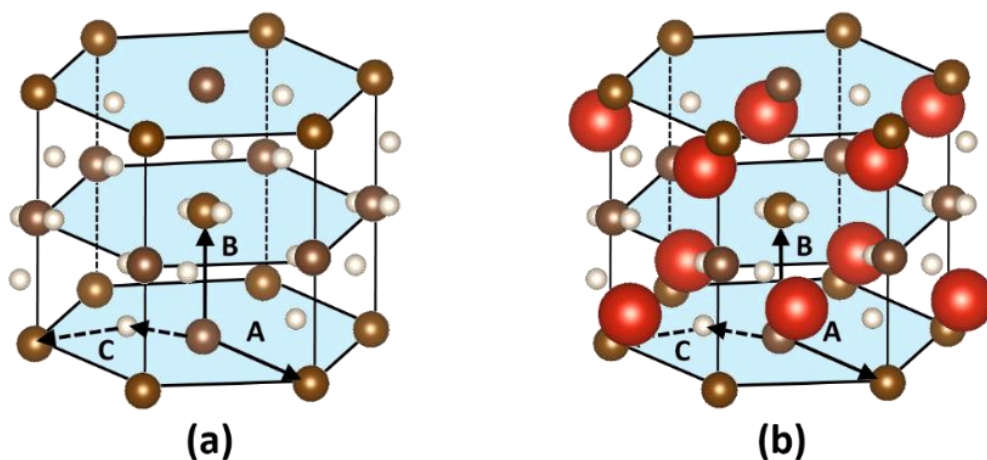


Figure 3-11. Octahedral-octahedral, labeled A and B, and octahedral-tetrahedral-octahedral, labeled C, site jumps considered as likely migration paths for carbon self-diffusion in V_2C (a) without and (b) with the vanadium atoms shown.

Based on our DFT calculations, the energy cost of a carbon atom occupying a tetrahedral site is > 1.5 eV more than the migration energy for the direct in-plane O-O

mechanism (jump A). This is true for all three of the ordered V₂C structures considered in this work. Therefore, the contribution of the O-T-O mechanism (jump C) to the self-diffusion coefficient of carbon will be negligible in comparison to the contribution from the direct O-O mechanism (jump A). Ignoring the contribution from O-T-O jumps, the in-plane D_{\perp} and out-of-plane D_{\parallel} self-diffusion coefficients for interstitial diffusion of carbon are given by

$$\begin{aligned} D_{\perp} &= \frac{1}{4} C_{v,\perp} f_x \sum_i v_i^* \exp\left(-\frac{\Delta E_{A,i}^m}{kT}\right) d_{\perp,i}^2 \\ D_{\parallel} &= \frac{1}{2} C_{v,\parallel} f_z \sum_i v_i^* \exp\left(-\frac{\Delta E_{B,i}^m}{kT}\right) d_{\parallel,i}^2 \end{aligned} \quad (3-7)$$

where $C_{v,\perp}$ and $C_{v,\parallel}$ are the fractions of vacant octahedral sites surrounding the migrating carbon atom within the same basal plane and in the adjacent basal planes, respectively. Effective frequencies are given by v_i^* , migration energies for jumps A and B are given by $\Delta E_{A,i}^m$ and $\Delta E_{B,i}^m$ and f 's are the correlation factors. In the expression for D_{\perp} , the sum is taken over all possible jumps of type A. Similarly, the sum in D_{\parallel} is taken over all possible jumps of type B. Jumps of type B do not contribute to D_{\perp} while jumps of type A do not contribute to D_{\parallel} . For the β' phase, $C_{v,\perp} = 1$ for the low-density carbon plane and $C_{v,\perp} = 1/2$ for the high-density plane. $C_{v,\perp} = 2/3$ for the two orthorhombic structures and $C_{v,\parallel} = 1$ for all three structures.

Every carbon atom is surrounded by eight NN octahedral sites: six sites in the same basal plane and one site in each of the two adjacent basal planes. For all three structures, the two sites in the adjacent planes are empty, thereby contributing two jumps of type B. For the two orthorhombic structures, four of the six in-plane sites are empty, while two are occupied by carbon atoms. Thus, there are four possible A jumps

for the two orthorhombic structures. For the β' phase, the situation is complicated by the fact that there are low- and high-density carbon planes. In the low-density plane, all six in-plane sites are empty, whereas, in the high-density plane, only three in-plane sites are empty. Thus, for the β' phase, there are six possible A jumps for the low-density carbon plane and three possible A jumps for the high-density plane. The converged MEPs for carbon migration in the β' phase are shown in Fig. 3-12. The MEPs for the orthorhombic structures (not shown) are similar albeit with only a single unique carbon plane. As in the case of the CI-NEB calculations for vanadium migration, the saddle points for carbon migration converge rapidly with respect to supercell size. Migration energies for a 72-atom supercell for the β' phase and 96-atom supercells for the two orthorhombic structures are converged to within 0.05 eV.

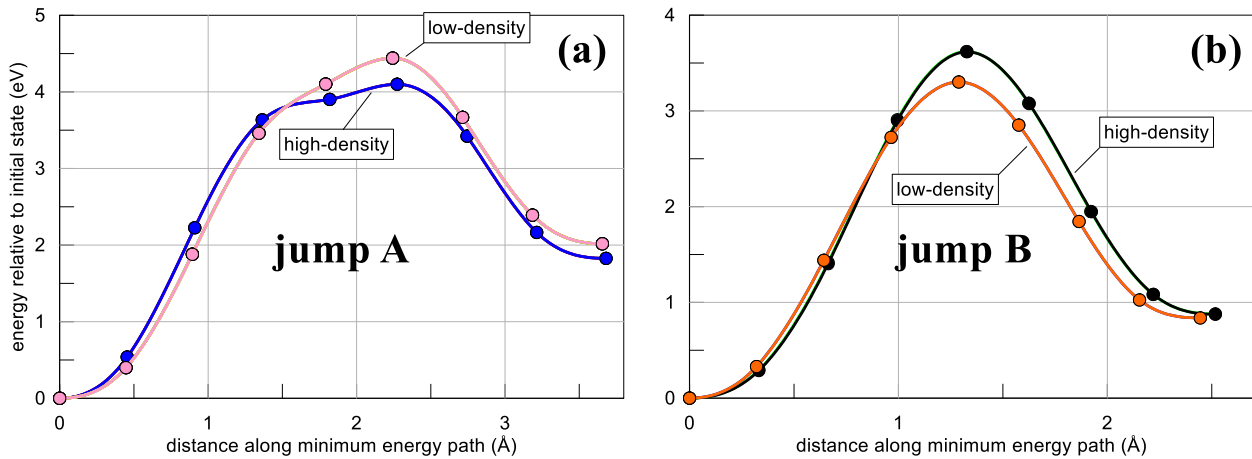


Figure 3-12. Theoretical MEPs for carbon interstitial migration (a) in-plane (jump A) and (b) out-of-plane (jump B) for the β' phase from CI-NEB calculations.

The converged migration energies ΔE_A^m and ΔE_B^m for each possible jump of that type and for each structure are given in Table 3-7. There is a variation in ΔE_A^m of 0.2 eV for the α phase, whereas all ΔE_A^m are equal for the $Pnmm$ structure and ΔE_A^m in like planes are equal for the β' phase. These differences can be attributed to the distribution

of carbon atoms among the six in-plane NN octahedral sites surrounding the migrating carbon atom. In the $Pn\bar{m}$ structure and the β' phase, the distribution of carbon atoms is symmetric, while in the α phase it is not. Calculated ranges of the effective frequencies ν_A^* and ν_B^* for carbon self-diffusion are also given in Table 3-7 for each jump type. The ν^* for carbon are calculated in the same manner and using the same supercell sizes used in the calculation of ν^* for vanadium self-diffusion.

Table 3-7. Migration energies ΔE_A^m and ΔE_B^m and effective frequencies ν^* for carbon self-diffusion for each of the three ordered V_2C structures calculated using DFT.

Space group (phase)	$Pn\bar{m}$	$Pbcn$ (α)	$P31m$ (β)
	4.09	4.13	4.44 (low density) 4.10 (high density)
	4.09	4.18	4.44 (low density) 4.10 (high density)
ΔE_A^m (eV)	4.09	4.18	4.44 (low density) 4.10 (high density)
	4.09	4.37	4.44 (low density)
	-	-	4.44 (low density)
	-	-	4.44 (low density)
ΔE_B^m (eV)	3.57	3.32	3.30 (low density) 3.62 (high density)
ν_A^* (THz)	19.8-19.9	20.0-23.4	22.6-22.8 (low density) 21.7-21.8 (high density)
ν_B^* (THz)	19.7-19.8	21.6-21.7	20.5-20.6 (low density) 22.0 (high density)

The vanadium and carbon atoms do not share a common sublattice: one is hcp while the other is simple hexagonal. This contrasts with fcc interstitial compounds, where the octahedral interstitial sites also form an fcc lattice. In the fcc case, the

correlation factor for interstitial self-diffusion will lie between that for pure vacancy-assisted diffusion and unity. Because there is not a simple one-to-one correspondence for *hcp* structures, we instead set the correlation factors for carbon self-diffusion to unity. The self-diffusion coefficients given in Eq. 3-7 are calculated using the results in Table 3-7 and then fit to $D = D_0 \exp(-Q/kT)$. The activation energies Q and diffusion prefactors D_0 from these fits are given in Table 3-8. Overall, the calculated activation energies for all three ordered V_2C structures agree well with the experimental results for self-diffusion of C in disordered cubic V_6C_5 and C in cubic $NbC_{0.868}$. However, our calculated diffusion prefactors underestimate experiment by two orders of magnitude.

Table 3-8. Activation energies Q and diffusion prefactors D_0 for carbon self-diffusion for each of the three ordered V_2C structures calculated using DFT.

	This work (<i>Pnnm</i>)	This work (α phase)	This work (β' phase)	C in V_6C_5 (Expt. Ref.[24])	C in $NbC_{0.868}$ (Expt. Ref.[20])
Q_{\perp} (kJ/mol)	91.5	96.3	102.4 (low density) 94.5 (high density)	85.0 ± 0.5	100.4 ± 2.2
Q_{\parallel} (kJ/mol)	82.9	76.6	76.1 (low density) 83.4 (high density)		
$D_{0,\perp}$ (cm ² /s)	0.016	0.015	0.028 (low density) 0.014 (high density)	$2.65^{+0.35}_{-0.31}$	$2.59^{+1.82}_{-1.07}$
$D_{0,\parallel}$ (cm ² /s)	0.009	0.010	0.009 (low density) 0.010 (high density)		

3.4 Discussion

When a vanadium atom migrates from one basal plane to an adjacent one, it must pass through an intervening plane of octahedral sites. The black arrow labeled B in Fig. 3-8(b) shows the direction of the out-of-plane jump. At the transition state, the vanadium atom lies between two octahedral sites. This leads to one of three scenarios.

Either both octahedral sites are occupied by carbon atoms, both sites are vacant, or only one site is occupied.

Due to the proximity of the octahedral sites to the migrating vanadium atom at the transition state, the height of the migration barrier depends strongly upon the distribution of carbon atoms at these sites. In the two orthorhombic structures, where the intervening plane of carbon atoms always has the same density, the highest migration barrier occurs when both sites are occupied, while the lowest barrier occurs when both sites are vacant. The third scenario, in which only one site is occupied, leads to an intermediate barrier. Evidence for this behavior is given by the three groups of MEPs shown in Fig. 3-9(b) for the α phase. The *Pnmm* structure exhibits the same grouping, while the behavior of the β' phase is complicated because of the alternating high- and low-density carbon planes. However, the highest out-of-plane vanadium migration barrier for the β' phase still corresponds to both octahedral sites being occupied by carbon atoms.

Despite the two orthorhombic structures exhibiting the same grouping of MEPs for out-of-plane vanadium jumps, we found that that the barrier heights for jumps within a group are different for each structure. For example, the highest and lowest out-of-plane vanadium migration barriers for the α phase are 4.02 eV and 1.46 eV, respectively, while, for the *Pnmm* structure, they are 4.84 eV and 1.24 eV. To understand this behavior, one must also consider the arrangement of other nearby carbon atoms in addition to those closest to the vanadium migration path. Carbon atoms in the *Pnmm* structure form linear chains that lie parallel to basal planes of vanadium atoms, while carbon atoms in the α phase form zigzag chains. The geometry of these

chains is highlighted in Fig. 3-13. In the figure, large (red) spheres are vanadium atoms, small dark (brown) spheres are carbon atoms and small light (white) spheres are empty octahedral sites.

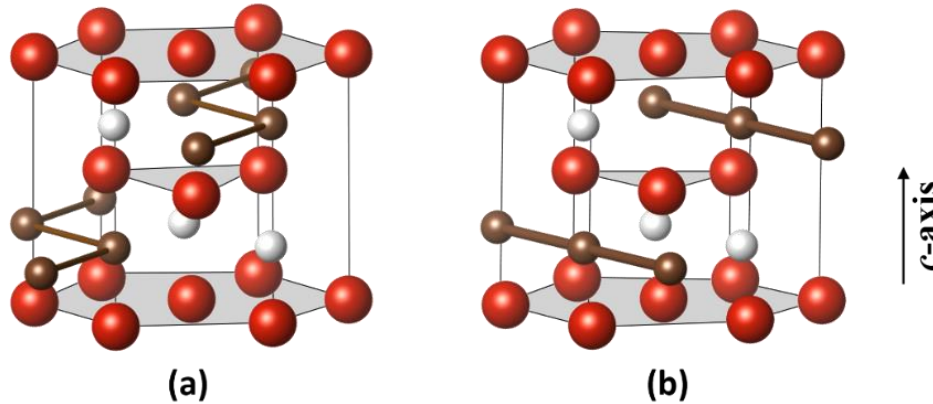


Figure 3-13. Illustration showing arrangement of carbon atoms for (a) the α phase of V_2C and (b) the low-energy orthorhombic structure described by space group Pnm .

A vanadium atom migrating into an adjacent basal plane in which the two intervening octahedral sites are occupied will displace both carbon atoms away from their ideal sites. On one hand, for the Pnm structure, the displacements are along the direction of the carbon chain. This leads to a great deal of resistance from the strong carbon-carbon bonds and the corresponding migration barrier for the vanadium atom is high. On the other hand, for the α phase, which has zigzag chains, the carbon atoms closest to the migrating vanadium atom are displaced towards empty octahedral sites. This leads to less resistance from other carbon atoms in the chain and correspondingly a smaller migration barrier for the α phase than for the Pnm structure.

The lowest out-of-plane migration barriers occur when both octahedral sites closest to the migrating vanadium atom are empty. At the transition state, the closest carbon atoms to the migrating vanadium atom are displaced towards the partially

vacated vanadium site. In the *Pnnm* structure, the displacements are nearly perpendicular to the direction of the carbon chains, so there is minimal resistance from other carbon atoms within the chain. By contrast, for the α phase, the displacements of these nearby carbon atoms tend to be directed more towards other neighboring carbon atoms within the zigzag chains. This leads to more resistance due to the strong carbon-carbon bonds and the corresponding migration barrier is higher for the α phase than for the *Pnnm* structure. Because the lowest migration barrier dominates the self-diffusion coefficient, the calculated activation energy for vanadium self-diffusion is ~ 8 kJ/mol less for the *Pnnm* structure than for the α phase.

Of the three V_2C structures, the β' phase has the highest activation energy for vanadium self-diffusion, followed by the α phase and then the *Pnnm* structure, see Table 3-6. The ~ 10 kJ/mol decrease in activation energy when going from the α to the β' phase is largely due to a ~ 0.2 eV difference in calculated values of $\Delta E_f[v_V]$, see Table 3-3. The calculated self-diffusion coefficients for vacancy-assisted self-diffusion of vanadium for the three ordered V_2C structures are plotted in Fig. 3-14. Experimental self-diffusion data for Nb in NbC_x [27] and Ti in TiC_x [28] are also included in the plot for comparison. Overall, the calculated self-diffusion coefficients are in better agreement with the self-diffusion data for Nb in NbC_x than for Ti in TiC_x , which is expected, as Nb and V belong to the same group in the periodic table.

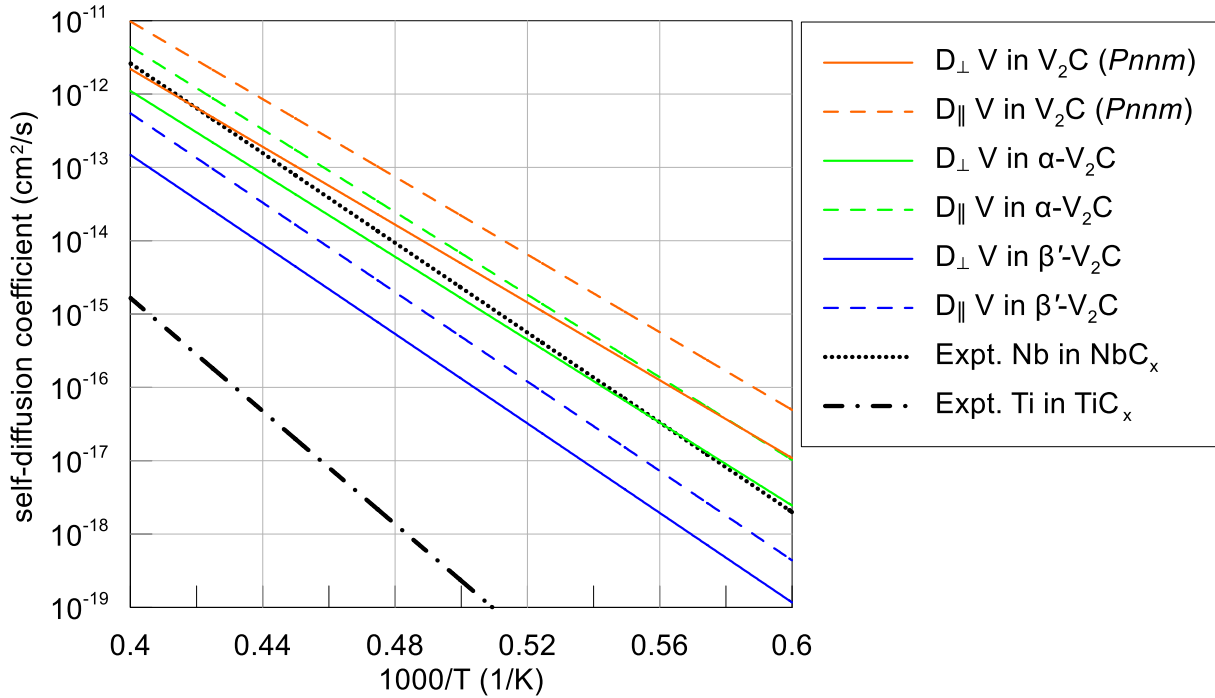


Figure 3-14. Calculated vanadium self-diffusion coefficients for the three ordered V_2C structures and experimental self-diffusion coefficients for Nb in NbC_x [27] and Ti in TiC_x [28].

The calculated self-diffusion coefficients for interstitial diffusion of carbon in the three ordered V_2C structures are shown in Fig. 3-15 along with experimental self-diffusion data for C in cubic $NbC_{0.868}$ [20] and C in cubic V_6C_5 [24]. The self-diffusion coefficients D_{\perp} and D_{\parallel} for the β' phase are averaged over the low- and high-density carbon planes. Note that the experimental data was obtained for self-diffusion in disordered structures, not the ordered structures considered in this work. Overall the calculated activation energies in Table 3-8 agree well with the experimental result for C in V_6C_5 . However, the calculated diffusion prefactors underestimate the experimental values by two orders of magnitude, which results in bad overall agreement with the self-diffusion coefficients, which is clear from Fig. 3-15. It is unclear why the underestimation is so severe.

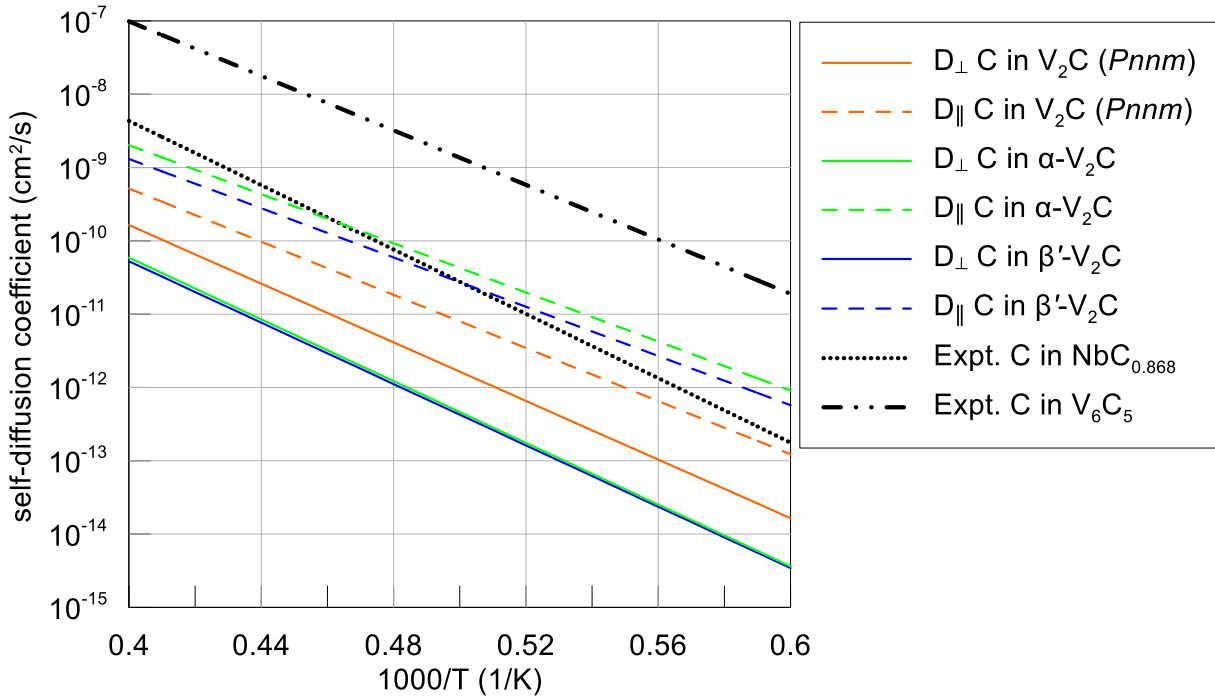


Figure 3-15. Calculated carbon self-diffusion coefficients for the three ordered V_2C structures and experimental self-diffusion coefficients for C in $NbC_{0.868}$ [20] and C in V_6C_5 [24].

Comparison of the vanadium and carbon self-diffusion coefficients shows that carbon self-diffusion is several orders of magnitude higher than vanadium self-diffusion. This is in agreement with self-diffusion experiments on several cubic transition metal carbides in which the carbon diffusivity was also found to be several orders of higher than the metal atom diffusivity [16,20,24,26–28,158]. Because we assume carbon diffuses via an interstitial mechanism, the carbon vacancy formation energy does not enter the expression for the self-diffusion coefficient. In contrast, vanadium self-diffusion is mediated by thermal vacancies and the added energy cost to produce these vacancies results in a much lower self-diffusion coefficient relative to carbon.

3.5 Summary

By enumerating all possible ordered V_2C structures up to 8 times the volume of the base *hcp* unit cell, our calculations reveal several ordered structures with lower energies than the experimentally observed α and β' phases. The simplest of these low-energy structures has a unit cell volume half that of the α phase and belongs to the orthorhombic space group *Pnmm*. The three ordered structures all exhibit similar electronic and elastic properties due to their nearly identical vanadium sublattices with variations that can be attributed to their different carbon arrangements. Of the three ordered V_2C structures considered in this work, the β' phase has the highest activation energy for vanadium self-diffusion, followed by the α phase and then the *Pnmm* structure. Differences in activation energies among the three ordered structures are the result of a combination of differences in vanadium vacancy formation energies and migration barrier heights. Calculated vanadium self-diffusion coefficients agree well with experimental results for Nb self-diffusion in single-crystal samples of disordered cubic NbC_x [27]. The calculated carbon self-diffusion coefficients are several orders of magnitude larger than those calculated for the metal atom, which is in agreement with diffusion experiments for the cubic transition metal carbides [16,20,24,26–28,158]. Theoretical activation energies for carbon self-diffusion in ordered V_2C agree well with experimental results for carbon self-diffusion in disordered cubic V_6C_5 [24], while diffusion prefactors are severely underestimated.

CHAPTER 4 ENERGETICS AND KINETICS OF METAL IMPURITIES IN VANADIUM CARBIDE

4.1 Background

Diffusion experiments on transition metal carbides are difficult due to a number of factors, including the difficulty of producing the high-purity single-crystal samples needed for accurate diffusion measurements [158]. While self-diffusion behavior of carbon interstitials has been investigated experimentally in NbC [20,23], ZrC [17], TiC [16,17,22], V₆C₅ [24], WC [153], Mo₂C [21] and Fe₃C [154], self-diffusion measurements for the metal atom are quite rare and results are known only for NbC_x [27] and TiC_x [28]. Furthermore, experiments have yet to address the diffusion of impurities in any of the transition metal carbides, including V₂C. From a theoretical perspective, the energetics of intrinsic defects and self-diffusion behavior in ordered phases of V₂C have been addressed in Chapter 3. However, no work has been done to address the energetics of impurities in V₂C or their diffusion behavior.

In this chapter, we seek to investigate the energetics of metallic impurities in the dilute limit and their migration within V₂C using DFT calculations. As was discussed in Chapter 3, this study is motivated by the potential use of V₂C as a diffusion coating to help mitigate fuel cladding chemical interaction in nuclear fuel rods. Calculations are performed for the ordered orthorhombic phase α -V₂C as (1) application temperatures for the diffusion barrier coating are expected to be below the order-disorder transition temperature, (2) it is the confirmed ground state phase for V₂C and (3) results of Chapter 3 indicate that carbon ordering does not have a significant effect on the self-diffusion behavior. Impurity species considered in this work include Fe and Ni as major

components of the cladding, Ce and Nd as fission products and U as a major component of the nuclear fuel.

As a first step, the formation energies for impurities at both the vanadium substitutional site and octahedral interstitial site are calculated to determine the site preference for each chemical species. All impurities are found to prefer the vanadium substitutional site. Assuming a standard vacancy-assisted mechanism for diffusion of impurities, we then calculate the impurity-vacancy binding energies. Large impurities, U, Nd and Ce, are found to bind much more strongly to neighboring vanadium vacancies than the smaller impurities, Fe and Ni. Relaxed impurity-vacancy structures show the large impurities form clusters with neighboring vacancies, so a standard vacancy-assisted diffusion mechanism is deemed unlikely. Migration barriers are calculated for the two small impurities, Fe and Ni, as they do not aggregate with neighboring vacancies. Comparison with migration barriers for V from Chapter 3 show that migration is easier for Ni, whereas it is harder for Fe.

4.2 Simulation Methods

Calculations are performed using the plane-wave DFT code VASP [131,159]. PAW potentials are used to treat the core electrons [160,161]. Electron exchange-correlation is treated by the PBE [129] formulation of the GGA, which has been shown in Chapter 3 to outperform the LDA in calculations on V_2C . Valence electron configurations for the reference atoms are the same as in Chapter 3 with the addition of $3d^64s^2$ for Fe, $3d^84s^2$ for Ni, $5s^25p^65d^16s^2$ for Ce, $5s^25p^65d^16s^2$ for Nd and $6s^26p^65f^77s^26d^1$ for U. DFT is known to have difficulties in treating partially filled f orbitals. Therefore, in our calculations the $4f$ electrons for Ce and Nd are treated as part of the frozen core in the pseudopotentials as was done in previous DFT calculation of

rare earth impurities in Mg [187]. There is no available PAW potential for U that includes the 5f electrons in the frozen core. Therefore, we apply a Hubbard U correction to the 5f orbitals in U using the Dudarev formulation [188]. An effective Hubbard parameter $U_{\text{eff}} = U - J = 1.24$ eV is used, which was shown to be the optimal value for calculations involving U metal and U-Zr alloys [189]. Tolerances on the electronic self-consistency cycle, interatomic forces and cell stress tensor are the same as in Chapter 3. Partial orbital occupancies are treated using the method of Methfessel-Paxton [190] (2nd order) with a smearing width of 0.1 eV.

Table 4-1. Theoretical equilibrium lattice constants, cohesive energies and magnetic moments for ground state phases of V, Fe, Ni, Ce, Nd and U. Deltas signify percent differences from experiment [191].

	V	Fe	Ni	Ce	Nd	U
Structure	<i>bcc</i>	<i>bcc</i>	<i>fcc</i>	<i>fcc</i>	<i>dhcp</i>	<i>ortho</i>
a (Å)	2.997	2.832	3.518	4.737	3.705	2.803
Δ	-0.9%	-1.2%	-0.2%	-2.3%	+1.3%	-1.8%
b (Å)	-	-	-	-	-	5.837
Δ	-	-	-	-	-	+0.6%
c (Å)	-	-	-	-	11.926	4.911
Δ	-	-	-	-	+1.1%	-0.9%
E_0 (eV/atom)	-8.992	-5.468	-8.238	-5.926	-4.712	-11.136
mag. (μ_B)	-	2.20	0.65	-	-	-
Δ	-	+0.5%	+2.3%	-	-	-

Note: *ortho* – orthorhombic; *dhcp* – double hexagonal close-packed

Reference chemical potentials used in the calculation of defect formation energies are calculated from the total energies of the relaxed ground state crystal structures for each element. Spin-polarized calculations are performed for the ferromagnetic elements Fe and Ni. Ground state structures, equilibrium lattice parameters, cohesive energies and magnetic moments (where necessary) are given in

Table 4-1 along with percentage differences from experiment [191]. A plane-wave energy cutoff of 600 eV and 6000 k -points per reciprocal atom are found to give total energies converged to within a few meV. Overall the agreement between the calculated and experimental lattice constants is good with a maximum difference of a few percent. Magnetic moments for bcc Fe and fcc Ni are also within a few percent of experiment.

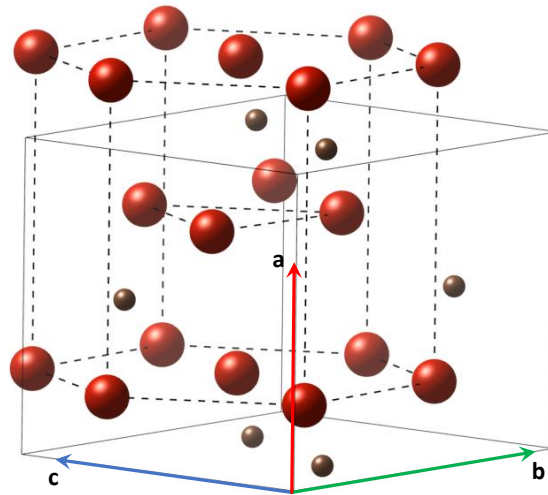


Figure 4-1. Unit cell (solid lines) of low-temperature ordered orthorhombic phase α - V_2C .

The vanadium sites of the α - V_2C phase constitute a nearly hcp sublattice with carbon atoms occupying exactly half of the available octahedral interstitial sites. The unit cell of α - V_2C is shown in Fig. 4-1 with additional vanadium atoms included to emphasize the hcp -like vanadium sublattice. In the figure, vanadium atoms are shown as large (red) spheres and carbon atoms are shown as small (brown) spheres. The octahedral site sublattice on which the carbon atoms reside is simple hexagonal with basal planes layered between the vanadium basal planes. Note that the close-packed direction is along \vec{a} , which means the basal planes lie in (100) lattice planes. Table 4-2 gives the cell dimensions, number of atoms, lattice parameters and k -point grids for the

supercells used in the defect calculations. Supercells up to 324 atoms are used to test for convergence of defect formation energies. The minimum distance between defects is given by the smallest cell dimension, e.g. a single defect in a 2x2x2 supercell has its nearest periodic image 9.10 Å away.

Table 4-2. Supercell dimensions and calculation parameters used in defect calculations for α -V₂C.

Supercell size	No. of atoms	a (Å)	b (Å)	c (Å)	k -point grid
1x1x1	12	4.55	5.73	5.03	9x9x9
1x2x2	48	4.55	11.46	10.06	9x5x5
2x2x2	96	9.10	11.46	10.06	5x5x5
3x2x2	144	13.65	11.46	10.06	3x5x5
3x2x3	216	13.65	11.46	15.10	3x5x3
3x3x3	324	13.65	17.20	15.10	3x3x3

MEPs for impurity migration are determined using the CI-NEB method [192,193]. The CI-NEB is preferred over the standard NEB method as one of the images along the MEP is guaranteed to converge to the saddle point, thus allowing easy and accurate calculation of migration barriers. The spring constant between images is set to 5 eV/Å². Convergence of the MEP is tested with respect to the number of interpolated images between the initial and final structures for a representative migration path. It is found that the MEP, including the location of the transition state, does not change appreciably beyond five images; therefore, five images are used in all CI-NEB calculations presented in this chapter.

4.3 Simulation Results

4.3.1 Impurity Site Preference

The substitutional vanadium and octahedral interstitial sites are chosen as the most likely sites for an impurity to occupy. All early transition metal carbides are good electrical and thermal conductors [146,147]. A metallic character is then expected for α -V₂C and is confirmed by electronic band structure and DOS calculations performed in Chapter 3 (Fig. 3-4) and in Refs. [34–36], which show an absence of a band gap at the Fermi level. Therefore, the metallic impurities will be charge neutral. The formation energy for a neutral impurity X (= Fe, Ni, Ce, Nd and U) on a substitutional vanadium site is given by

$$\Delta E_f[X_V] = E[X_V] - E[\text{bulk}] + \mu_V - \mu_X, \quad (4-1)$$

where $E[X_V]$ is the total energy of the supercell with the impurity, $E[\text{bulk}]$ is the energy of the perfect supercell and μ_V and μ_X are the chemical potentials of vanadium and the impurity, respectively. The chemical potential for each element is taken as the cohesive energy-per-atom of the relaxed ground state phase, see Table 4-1. All vanadium sites in α -V₂C are equivalent by symmetry, so there is a single unique $\Delta E_f[X_V]$ for each impurity species.

Half of the octahedral sites are occupied by carbon atoms, while the remaining half are free to accept an impurity. The formation energy for an impurity at an interstitial site is given by

$$\Delta E_f[X_i] = E[X_i] - E[\text{bulk}] - \mu_X, \quad (4-2)$$

where only the chemical potential of the impurity must be accounted for as the interstitial site is not previously occupied. Again, μ_X is the cohesive energy-per-atom of

the ground state phase of impurity X . As is the case for the vanadium sites, all empty interstitial sites are equivalent by symmetry, so there is a single unique $\Delta E_f[X_i]$ for each impurity species. Using the relaxed supercells from the substitutional and interstitial defect calculations, we also calculate the impurity volume

$$V_{imp}^X = V[X] - V[\text{bulk}], \quad (4-3)$$

where $V[X]$ and $V[\text{bulk}]$ are the volumes of the defect and perfect supercell, respectively. V_{imp}^X gives a measure of the size of the impurity. In the case of a substitutional defect, a negative V_{imp}^X implies that the defect is smaller than original vanadium atom.

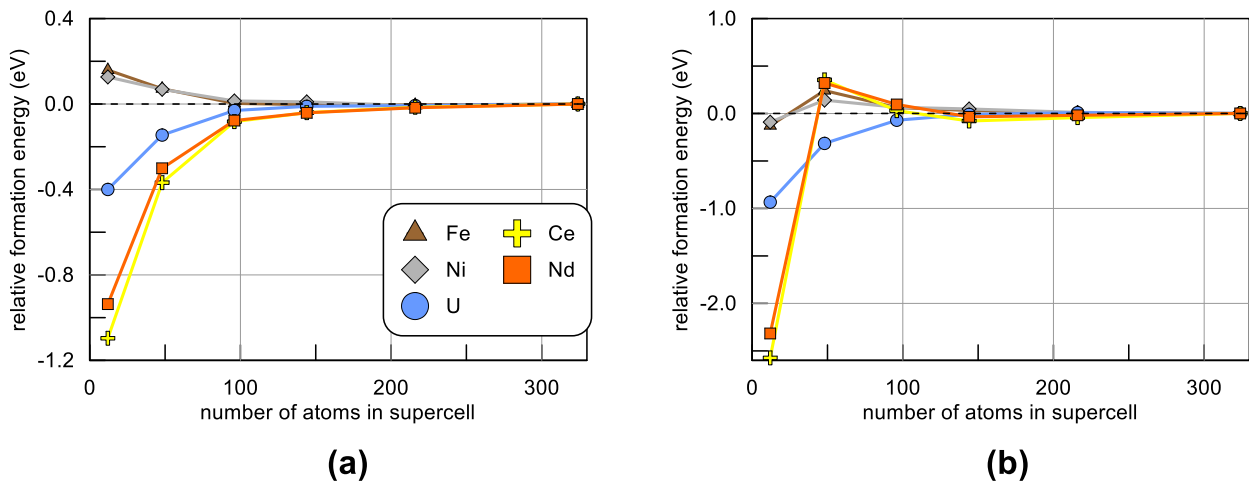


Figure 4-2. Convergence of (a) substitutional and (b) interstitial defect formation energies with respect to the size of the defect supercell. In each case, the zero of the relative formation energy corresponds to the size-converged formation energy.

Calculations of both substitutional and interstitial impurities are performed for the supercells listed in Table 4-2 to test for convergence of the defect formation energies. Relative defect formation energies are plotted in Fig. 4-2 as a function of the number of atoms in the supercell, where the reference point is taken as the corresponding defect

formation energy for the largest 3×3×3 supercell. Formation energies for both substitutional and interstitial impurities have converged to within 0.1 eV when the supercell dimensions are 2×2×2 and to within 0.05 eV when the supercell dimensions are 3×2×2. In addition, we observe less variation in the defect formation energies for the two smaller impurities, Fe and Ni, than for the larger ones, Ce, Nd and U.

Table 4-3. Substitutional and interstitial defect formation energies and impurity volumes.

Impurity	Formation energy (eV)		Impurity volume (Å ³)	
	<i>substitution</i>	<i>interstitial</i>	<i>substitution</i>	<i>interstitial</i>
Fe	0.77	2.83	-3.7	11.6
Ni	1.38	2.89	-2.4	11.9
U	2.81	6.26	10.4	19.5
Nd	4.36	8.12	15.3	24.3
Ce	5.07	8.82	15.6	25.8

Table 4-3 gives the substitutional and interstitial defect formation energies and impurity volumes for Fe, Ni, Ce, Nd and U calculated for the 3×3×3 supercell. No magnetic ground states were found in spin-polarized calculations. For all impurity species, the substitutional site is ~2–3 times lower in energy than for the interstitial site. Therefore, we conclude that substitution on a vanadium site is preferred for all impurity species. For both sites, the defect formation energy increases with the impurity volume. The ordering of impurity volumes is Fe < Ni < U < Nd < Ce. Defect formation energies follow the same trend. Without including the Hubbard correction, $\Delta E_f[U_V]$ increases by 0.1 eV and $\Delta E_f[U_i]$ decreases by 0.2 eV. Moreover, V_{imp}^U decreases by 0.5 and 0.8 Å³ for the substitutional vanadium site and interstitial site, respectively.

Impurity volumes for Ce, Nd and U at the substitutional site are positive indicating that they are larger than the original V atom, whereas for Fe and Ni, $V_{imp}^X < 0$ indicating a contraction of the cell around the impurity. Both Fe and Ni undergo minimal displacements $< 0.05 \text{ \AA}$ from the ideal vanadium site, while the larger impurities undergo much larger displacements $> 0.2 \text{ \AA}$ directed out of the basal plane and towards empty octahedral sites. As expected, all impurity volumes for the interstitial site are positive due to the site being previously unoccupied.

4.3.2 Impurity-vacancy Binding

Experiments have found the metal atom self-diffusion in NbC_x [27] and TiC_x [28] to be independent of the carbon composition. Therefore, as the vanadium substitutional site is energetically favored, we expect diffusion of the impurity to occur via direct exchange with a nearest-neighbor (NN) vanadium vacancy. A substitutional impurity is surrounded by twelve NN vanadium atoms: six within its own basal plane and three in each of the two adjacent basal planes, see Fig. 4-3. In an *hcp* crystal, like Mg, all in-plane impurity-vacancy pairs are equivalent and all out-of-plane impurity-vacancy pairs are equivalent [36,187,195]. However, in $\alpha\text{-V}_2\text{C}$, the impurity does not remain at the ideal vanadium site. Moreover, the proximity to carbon interstitials is different for different impurity-vacancy pairs. This leads to asymmetry among the in-plane and out-of-plane pairs; therefore, all twelve pairs must be examined individually.

The binding energy for an impurity-vacancy pair is given by

$$-\Delta E_b[X_V - v_V] = E[X_V v_V] + E[\text{bulk}] - E[X_V] - E[v_V], \quad (4-4)$$

where $E[X_V v_V]$ is the total energy of a supercell containing a substitutional impurity and a NN vanadium vacancy and $E[v_V]$ is the total energy of the same supercell with a

single vanadium vacancy. $E[\text{bulk}]$ and $E[X_V]$ are the same as in Eq. 4-1. The negative sign in front of the binding energy is added by convention so that $\Delta E_b > 0$ indicates favorable binding. The formation energy of an impurity-vacancy pair is related to the binding energy by

$$\Delta E_f[X_V - v_V] = \Delta E_f[v_V] - \Delta E_b[X_V - v_V], \quad (4-5)$$

where $\Delta E_f[v_V]$ is the formation energy of a single vanadium vacancy and has already been calculated for $\alpha\text{-V}_2\text{C}$ in Chapter 3. As $\Delta E_f[v_V]$ is a fixed value, a greater value for ΔE_b translates into a lower formation energy for the impurity-vacancy pair.

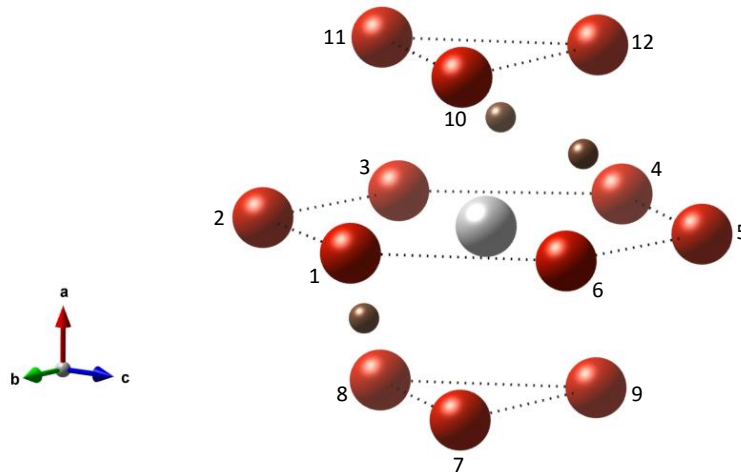


Figure 4-3. Impurity-vacancy pairs in the $\alpha\text{-V}_2\text{C}$ structure: six in-plane pairs have indices 1–6 and out-of-plane pairs have indices 7–12.

Calculated binding energies for each of the twelve impurity-vacancy pairs and five impurity species are given in Table 4-4. Values are calculated for a $2 \times 2 \times 2$ supercell. Indices correspond to the labels in Fig. 4-3, which shows the 1st NN shell around a substitutional vanadium impurity in $\alpha\text{-V}_2\text{C}$. For example, the row indexed 1 in Table 4-4 corresponds to ΔE_b supposing the atom labeled 1 in Fig. 4-3 was removed. Almost all binding energies are positive, indicating a favorable impurity-vacancy

interaction, save for one impurity-vacancy pair for Fe, which has a small negative value of -0.01 eV. The negative binding energy may be due to the increased proximity of this impurity-vacancy pair to interstitial carbon atoms relative to other pairs within the same basal plane.

Table 4-4. Impurity-vacancy binding energies for each of the six in-plane and six out-of-plane nearest-neighbor sites on the vanadium sublattice. $\Delta E_b > 0$ indicates favorable binding.

	Index	Fe	Ni	U	Nd	Ce
ΔE_b (eV) (in-plane)	1	0.07	0.21	0.45	0.40	1.21
	2	0.05	0.17	0.54	0.55	0.65
	3	0.09	0.18	0.61	1.15	1.46
	4	0.11	0.21	0.91	1.05	1.21
	5	-0.01	0.14	1.01	1.13	1.31
	6	0.12	0.17	0.57	0.64	0.76
ΔE_b (eV) (out-of-plane)	7	0.15	0.26	1.31	1.43	1.65
	8	0.13	0.28	1.13	1.56	1.84
	9	0.22	0.60	2.84	3.53	3.77
	10	0.14	0.22	1.31	1.43	1.65
	11	0.12	0.18	0.85	1.32	1.60
	12	0.21	0.34	0.45	0.40	0.44

Independent of the impurity species, ΔE_b is highest for the 9th out-of-plane impurity-vacancy pair. Examination of Fig. 4-3 shows that this pair has no intervening carbon interstitials between the adjacent vanadium basal planes. For the three large impurities, Ce, Nd and U, the minimum value of ΔE_b occurs for the 12th out-of-plane impurity-vacancy pair, which has two intervening carbon interstitials between the adjacent vanadium basal planes. The difference between the maximum and minimum values of ΔE_b is > 2 eV for Ce, Nd and U, which indicates the proximity of carbon interstitials to the impurity-vacancy pair can have a significant effect on binding strength

in the case of large impurities. In contrast, for smaller impurities, Fe and Ni, the difference is much less (< 0.5 eV).

For all impurity-vacancy pairs, binding is much weaker for the small impurities, Fe and Ni, than for the large ones, Ce, Nd and U. This can be seen clearly in Fig. 4-4(a), which plots the average in-plane and out-of-plane impurity-vacancy binding energies as a function of the impurity volume. The average distance of each impurity from the ideal substitutional site due to relaxation is plotted in Fig. 4-4(b). The much larger binding energies in the case of Ce, Nd and U are the result of significant displacements (> 0.5 Å) of the impurity towards the vacancy. In contrast, Fe and Ni remain much closer (< 0.1 Å) to the ideal substitutional site. As was shown in previous calculations of impurities in Al [196], the lattice strain that surrounds a large impurity can be reduced through the introduction of a neighboring vacancy. Clearly, the same mechanism is at play here.

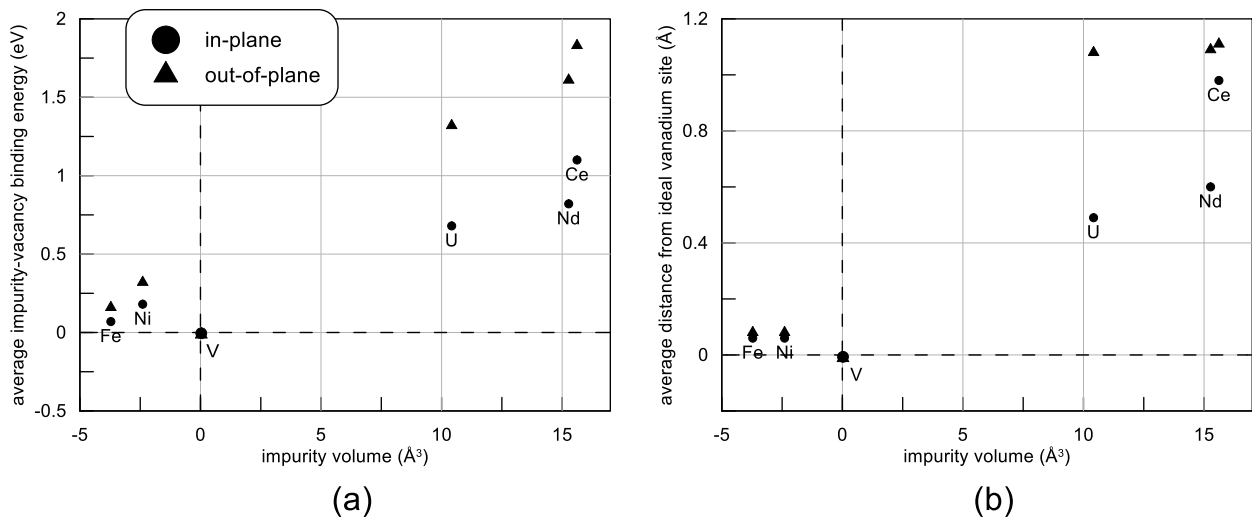


Figure 4-4. Average in-plane and out-of-plane impurity-vacancy (a) binding energies and (b) distance from the ideal vanadium site for substitutional impurities $X =$ Fe, Ni, Ce, Nd and U in α -V₂C.

As no experimental values exist for impurity-vacancy binding energies in V_2C , we compare our calculated energies for α - V_2C with those calculated in previous works for *hcp* Mg [187,195]. Calculated ΔE_b for an in-plane impurity-vacancy pair in α - V_2C (*hcp* Mg) are 0.07(0.09), 0.18(0.16), 0.82(0.02) and 1.10(0.08) for Fe, Ni, Nd and Ce, respectively. Note that the values given for α - V_2C are averages over all six in-plane pairs, as in Fig. 4-4(a). Binding energies for Fe and Ni in Mg are within a few hundredths of an eV of the average binding energies for α - V_2C , whereas binding energies for the larger impurities, Nd and Ce, are much higher in α - V_2C than in Mg. Although impurity-vacancy binding energies were not calculated in Refs. [187,195] for U in Mg, we expect the result to be the same. We stress that the only similarity between α - V_2C and Mg is that the metal atoms in both structures form an *hcp* lattice. The close agreement observed in impurity-vacancy binding energies for Fe and Ni is coincidental.

We suspect that the large difference in binding energies between the small impurities (Fe and Ni) and the large impurities (Ce, Nd and U) can be attributed to the openness of the α - V_2C structure, which is the result of a partially filled interstitial sublattice. This openness in α - V_2C allows large impurities room to relax, so that they can get closer and bind more strongly to a neighboring vanadium vacancy. This is confirmed by the data in Fig. 4-4(b), which shows that Ce, Nd and U undergo large displacements away from the ideal vanadium substitutional site. In the close-packed crystal structure of Mg, there is much less room into which atoms can relax, so the binding energies for the small and large impurities are similar.

4.3.3 Migration Barriers for Impurity Diffusion

When a vanadium vacancy is introduced into the 1st NN shell surrounding one of the large impurities, Ce, Nd and U, the impurity undergoes significant relaxation towards

the vacancy, which results in the formation of a defect cluster. In some cases, the relaxation is so large that the impurity sits within the interstitial plane. Therefore, we expect that diffusion of Ce, Nd and U should occur via some alternate mechanism, possibly involving multiple vanadium or carbon vacancies. However, the small impurities, Fe and Ni, remain closely bound to the ideal substitutional site and, so a simple vacancy-assisted mechanism may still be applicable.

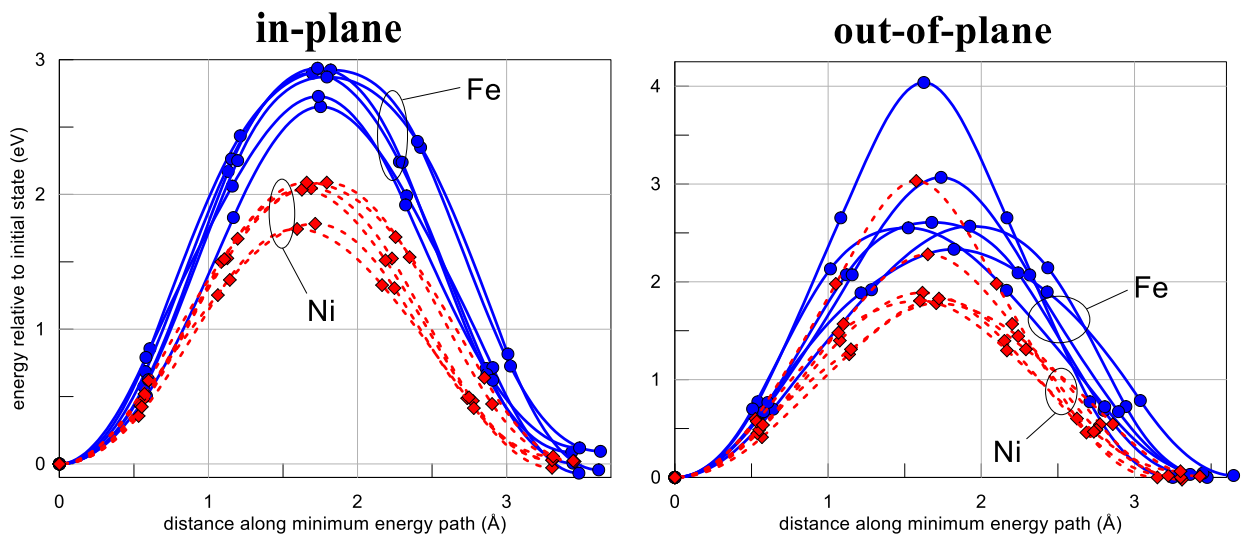


Figure 4-5. MEPs for migration of Fe and Ni impurities for each of the six in-plane and six out-of-plane vanadium sites.

MEPs for migration of Fe and Ni impurities to NN vanadium vacancies are calculated using the CI-NEB method. All six in-plane and out-of-plane vacancy sites must be treated as was done in the calculation of the impurity-vacancy binding energies. Calculated MEPs for each of the six possible in-plane and six possible out-of-plane jumps for Fe and Ni impurities are shown in Fig. 4-5. Energies are given relative to the initial state and the maximum point along the MEP corresponds to the transition state. MEPs calculated for in-plane jumps are more clustered than those calculated for out-of-plane jumps. This was also seen in Chapter 3 for the case of vanadium migration

in V_2C , where it was determined that the large variation in out-of-plane jumps can be attributed to the intervening plane of carbon interstitials.

The average in-plane and out-of-plane migration barriers in α - V_2C are 2.85 and 2.86 eV for Fe and 1.96 and 2.10 eV for Ni, respectively. For comparison, the average in-plane and out-of-plane migration barriers for V in α - V_2C are 2.71 and 2.24 eV, respectively. Therefore, migration is easier for Ni than for V, while migration is more difficult for Fe than either Ni or V.

4.4 Summary

In this chapter, we performed DFT calculations to investigate the energetics and kinetics of dilute metal impurities in V_2C . The impurities Fe, Ni, Ce, Nd and U were chosen to represent the different components of the combined fuel-clad system in which V_2C may be used as a diffusion barrier. We found that all impurity types prefer the vanadium substitutional site over the octahedral interstitial site and that the energy to incorporate the impurity increases with the impurity volume. Impurity-vacancy binding energies were calculated as a first step in determining the migration kinetics. Large impurities, U, Ce and Nd, bind more strongly to neighboring vanadium vacancies than the smaller impurities, Fe and Ni. The strong binding for the large impurities is attributed to the openness of the V_2C structure, which allows the lattice strain created upon insertion of the impurity to be partially relieved upon introduction of a neighboring vacancy. Because the large impurities form clusters with neighboring vanadium vacancies, a standard vacancy-assisted migration mechanism is deemed unlikely. However, the small impurities, Fe and Ni, remain close to the ideal vanadium site, so migration barriers can be calculated. Comparison with migration barriers for vanadium self-diffusion show migration of Ni is easier, while migration of Fe is more difficult.

CHAPTER 5 SHOCK COMPRESSION OF COPPER-ZIRCONIUM METALLIC GLASSES²

5.1 Background

Metallic glasses (MGs) have attracted a great deal of attention due to their excellent mechanical and physical properties [2,50,197–199]. Because of their good glass-forming ability and low cost, Cu- and Zr-based MGs are of interest for engineering applications. Recently, high-strain-rate impact experiments have been carried out on Cu- and Zr-based multicomponent MGs to investigate shock compression [57,58,60,65,200] as well as spallation behavior [201,202]. Hugoniot compression curves of shock velocity (U_s) versus impact/particle velocity (U_p) exhibit bilinear behavior with kinks appearing between 10 and 20 GPa that most likely indicate a phase transition [57,58,60,65,200]. Because of the short time- and length-scales inherent to shock compression experiments, no one has yet directly observed the microstructural changes occurring within the MGs during shock compression, and explanations of the kinks observed in the U_p - U_s Hugoniot curves continue to be a matter of debate [60,200]. MD simulations can provide a full atomic-level picture of the shock response of the sample, while overlapping with the range of strain rates attainable in laser-based shock compression experiments. Such simulations should be useful in shedding light on the high-strain-rate deformation behavior of MGs.

A large number of MD simulation works have focused on the shock response of single-crystal [82–85,88,89,92,203–205] and polycrystalline metals [81,206–208]. By

²The work described in this chapter has been published in P. Wen, B.J. Demaske, D.E. Spearot and S.R. Phillpot, J. Mater. Sci. doi:10.1007/s10853-017-1666-5. The first two authors contributed equally to this work.

contrast, only a few MD simulation works have investigated the shock response of MGs [91,93,209–211]. One such study by Arman et al. [93] found that atoms with different local structures exhibit different resistances to shear deformation, which leads to shear localization. Chen et al. [210] carried out MD simulations to investigate the time-dependent shock-induced strength of $\text{Cu}_{46}\text{Zr}_{46}\text{Al}_8$ MG. They proposed a hard-viscous composite material model to describe non-equilibrium strength relaxation at the shock wave front. Jian et al. [91] investigated short- and medium-range orders, and atomic packing efficiency in $\text{Cu}_{46}\text{Zr}_{54}$ MG upon shock loading. They found that the evolutions of short- and medium-range orders are the effects of compression combined with shock-induced melting. Huang et al. [211] studied the ductile-to-brittle transition during spallation of $\text{Cu}_{50}\text{Zr}_{50}$ MG. They found that the transition is controlled by the interaction between void nucleation and growth, which can be regarded as a competition between tension transformation zones and shear transformation zones (STZs). STZs are the fundamental unit of plastic deformation in MGs and will be discussed in more detail in Chapter 6. Lastly, Marinier et al. used a two-temperature model coupled to MD to simulate laser ablation of $\text{Cu}_x\text{Zr}_{100-x}$ MGs and observed homogeneous nucleation of STZs out of the pristine glassy material [209].

Recent experimental work and MD simulations on the binary Cu-Zr glass-forming system have revealed a strong dependence of glass-forming ability on the composition dependence [212–214] as well as structural and mechanical properties [215–222]. Over a wide composition range ($x = 35–70$), $\text{Cu}_x\text{Zr}_{100-x}$ MGs exhibit monotonic changes in high-energy X-ray diffraction patterns, atomic pair correlation functions, mass density and thermal stability behavior [218]. Quasistatic compression

experiments on a series of $\text{Cu}_x\text{Zr}_{100-x}$ MGs have shown that as Cu content increases from $\text{Cu}_{50}\text{Zr}_{50}$ to $\text{Cu}_{64}\text{Zr}_{36}$ the yield strength of the MG increases while the plasticity gradually diminishes [215,216].

In this chapter, the shock response of $\text{Cu}_x\text{Zr}_{100-x}$ ($x = 30, 50$ and 70) MGs is investigated via large-scale MD simulations. The response of each MG is characterized over a range of piston velocities $U_p = 0.125 - 2.5$ km/s, which corresponds to shock pressures from 3 to 130 GPa. At moderate shock intensities, all three MG compositions are found to undergo an elastic-plastic transition characterized by the formation of a sluggishly rising plastic wave preceded by a sharply rising and narrow elastic precursor. In contrast to crystalline metals, the yield strength of MGs under shock loading is found to depend on non-shear components of the pressure tensor. Simulated U_p-U_s Hugoniot curves exhibit elastic and plastic branches that converge at moderate shock intensities. Hugoniot states are found to depend strongly on Cu composition with $\text{Cu}_{70}\text{Zr}_{30}$ exhibiting greater resistance to plastic deformation than either $\text{Cu}_{50}\text{Zr}_{50}$ or $\text{Cu}_{30}\text{Zr}_{70}$.

5.2 Simulation Methods

5.2.1 Interatomic Potential Verification

Previous MD studies of impact- or laser-based shock compression on Cu-Zr MGs used the Finnis-Sinclair type EAM interatomic potential developed by Mendeleev et al. [223], whereas shock compression simulations of Cu-Zr-Al MGs used the ternary EAM potential developed by Cheng et al. [224]. While both the Mendeleev and Cheng potentials were designed to model MG structures, neither was designed specifically for shock compression simulations. Therefore, it is not clear which is better suited for this purpose. Zero-temperature stress-strain (cold pressure) curves are a computationally inexpensive way to help determine the applicability of a given potential to shock

compression simulations. A well-behaved potential should exhibit a monotonic increase in pressure as well as be free of inflection points at which $\partial^2 P / \partial \rho^2 = 0$, where P is the hydrostatic pressure and ρ is the mass density. Meeting this criterion is critical for shock compression simulations as failure to do so can result in unusual behavior such as decreasing sound speed ($c^2 = \partial P / \partial \rho$) with compression.

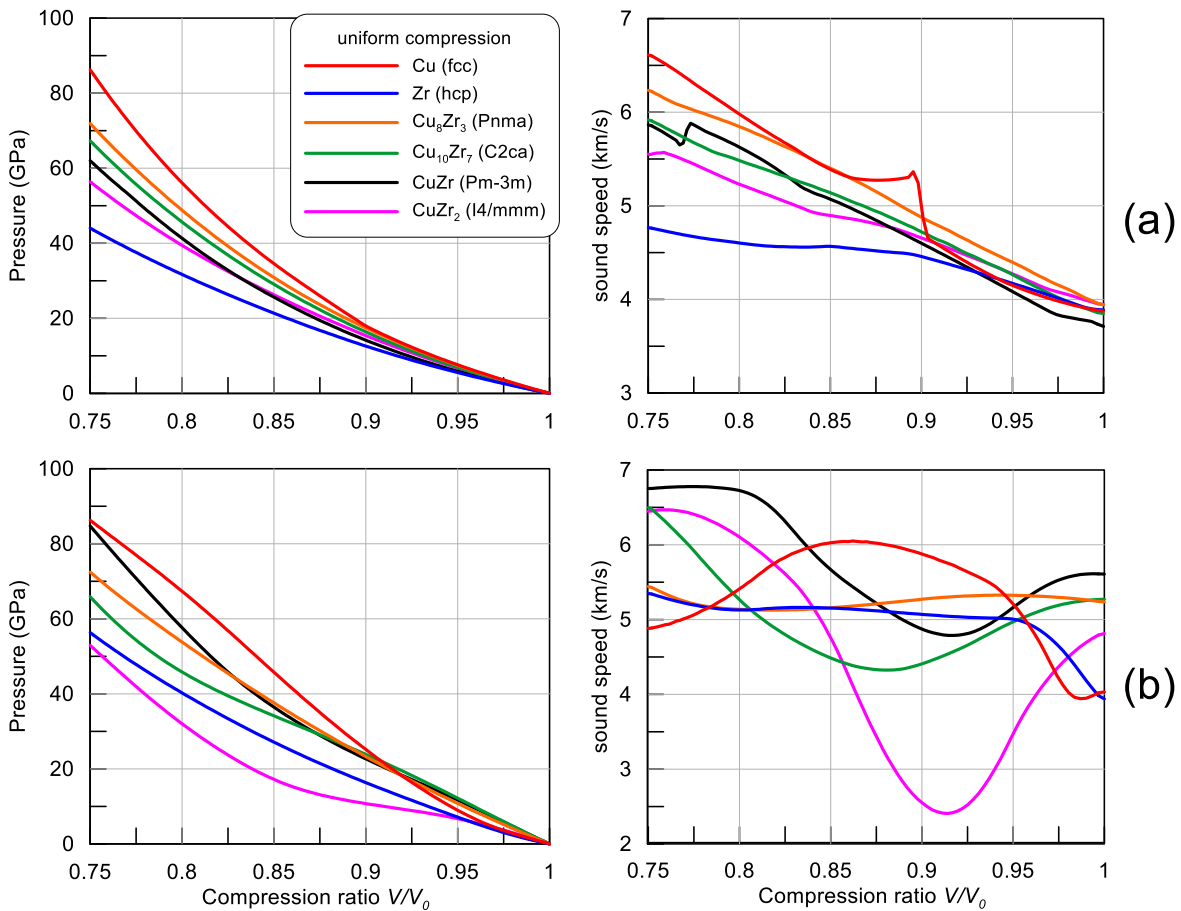


Figure 5-1. Zero-temperature stress-strain curves and sound speed curves calculated using the (a) Cheng potential for Cu-Zr(-Al) [224] and the (b) Mendeleev potential for Cu-Zr [223].

Cold pressure curves for uniform compression are calculated using LAMMPS [140] for the following crystalline phases: Cu (*fcc*), Cu_8Zr_3 (*Pnma*), $\text{Cu}_7\text{Zr}_{10}$ (*C2ca*), CuZr (*B2*), CuZr_2 (*I4/mmm*) and Zr (*hcp*). These phases are chosen to represent the different

local environments atoms are likely to encounter for the different compositions of MGs. Figure 5-1 is a plot of the cold pressure and sound speed curves for the Mendeleev and Cheng EAM potentials. Both potentials exhibit a monotonic increase in pressure for all crystalline phases over the range $0.75 < V/V_0 < 1$, where V/V_0 is the compression ratio. For the Cheng potential, all four binary phases exhibit increasing sound speed with compression (no inflection points) down to $V/V_0 = 0.78$, while the two unary phases, *fcc* Cu and *hcp* Zr, exhibit decreasing sound speed with compression over the brief intervals $0.88 < V/V_0 < 0.90$ and $0.84 < V/V_0 < 0.85$, respectively. For the Mendeleev potential, the cold pressure curves are generally not as well-behaved. All four binary phases and *fcc* Cu exhibit decreasing sound speed with compression over a large fraction of the range $0.75 < V/V_0 < 1$. The only exception is *hcp* Zr, which has similar behavior for both potentials.

Compression waves with amplitudes within the range where sound speed decreases with compression will not form shocks, but will instead spread out during propagation. Moreover, rarefaction waves in this range will form shocks. Such behavior is atypical [54,225]. If instead sound speed increases with compression, as is the case in most materials, then an initially smooth compression wave will steepen as it propagates until it forms a shock. The large regions of decreasing sound speed with compression exhibited by the Mendeleev potential for both unary and binary crystalline phases of the Cu-Zr system make it unattractive for shock simulation. In contrast, the Cheng potential exhibits decreasing sound speed with compression over a very limited range of compression ratios and only for unary phases, while the four binary phases all exhibit increasing sound speed with compression down to $V/V_0 = 0.78$. Overall, the

Cheng potential exhibits better compression behavior than the Mendeleev potential over the range $0.75 < V/V_0 < 1$. Therefore, the Cheng potential is better suited for shock compression simulations and is used in the MD simulations presented in this work.

5.2.2 Amorphous Structure Creation

The compositions used to create the MG samples used in this work are $\text{Cu}_{30}\text{Zr}_{70}$, $\text{Cu}_{50}\text{Zr}_{50}$ and $\text{Cu}_{70}\text{Zr}_{30}$. The initial *fcc* crystal structures consist of 4000 Cu atoms with 3D periodic boundary conditions. To achieve the desired composition, Cu atoms are randomly replaced with Zr atoms. Each system is given an initial temperature of 300 K and then heated at a constant rate of 10 K/ps to 2300 K. This temperature is chosen as it is far above the equilibrium melting temperatures of both Cu and Zr [226]. After heating, the system is equilibrated for 200 ps at 2300 K to ensure uniform mixing. The system is then cooled to 300 K at a constant rate of 5 K/ps. The cooling rate is within an order of magnitude of those used in previous studies [91,93,211]. The heating and quenching simulations are performed under the isobaric canonical (*NPT*) ensemble with a target pressure of zero.

Mean square displacement (MSD) curves and radial distribution functions (RDFs) are calculated for each composition after heating to 2300 K and after cooling to 300 K. The MSD curves of the system at 2300 K, shown in Fig. 5-2(a), exhibit linear behavior typical of a liquid. In contrast, the MSD curves for the quenched samples, shown in Fig. 5-2(b), are four orders of magnitude smaller, which indicates the atoms are capable of only local rearrangements, as is true in solids. Upon cooling, the second peak of the RDF splits indicating the final solid structure is amorphous, see Fig. 5-2(c) and 5-2(d). The average atomic volume as a function of temperature $V(T)$ during cooling is shown in Fig. 5-3 for all three compositions. Linear fits are applied to $V(T)$ on either side of the

glass transition. The temperature at the intersection of the two fits gives an estimate of the glass transition temperature T_g .

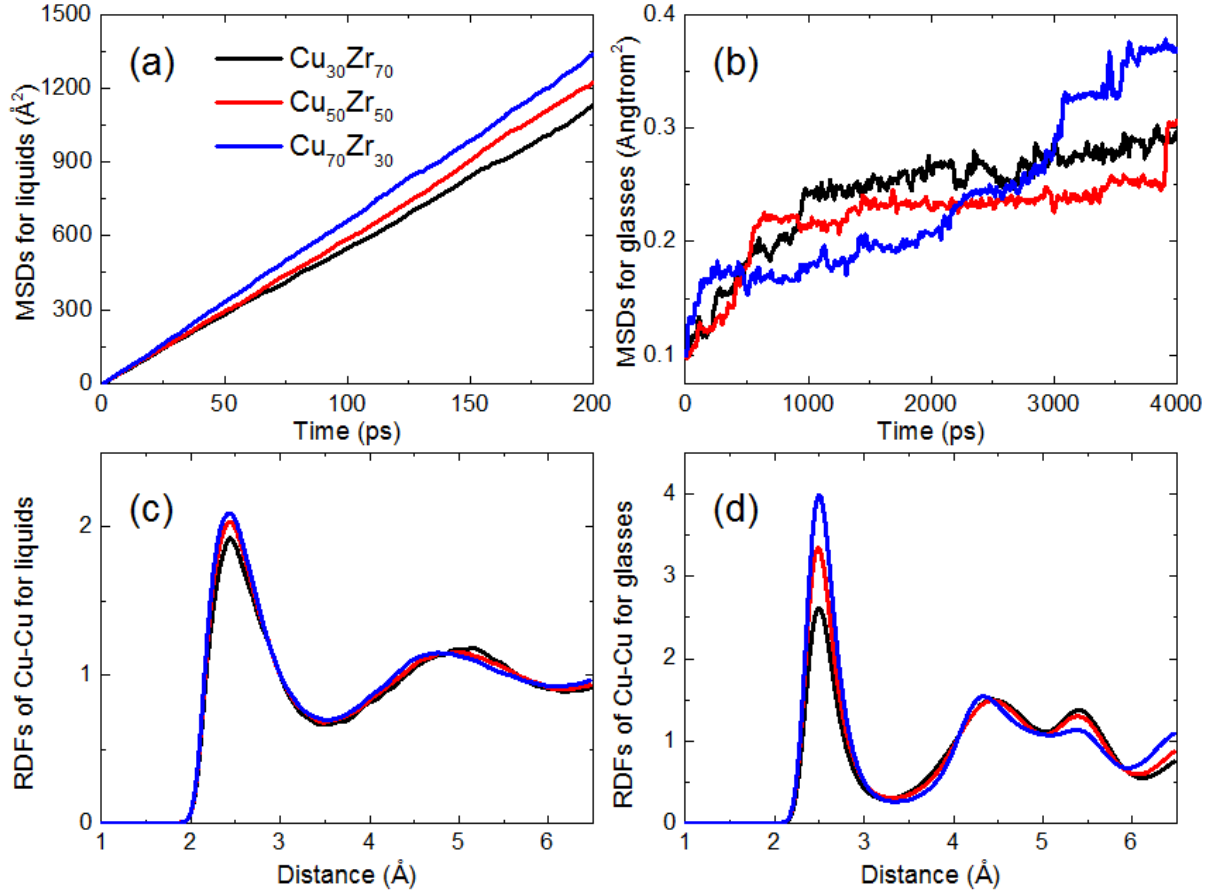


Figure 5-2. MSDs for (a) liquid and (b) metallic glass and Cu-Cu RDFs for (c) liquid and (d) metallic glass.

Table 5-1 gives the equilibrium density, elastic constants, sound speeds and glass transition temperatures T_g for each of the three MG samples. In the table, ρ is the mass density, B is the bulk modulus, G is shear modulus, ν is the Poisson ratio and c_β and c_α are the bulk and longitudinal sound velocities, respectively. Systems with higher Cu content have higher values of T_g , which is consistent with experimental results [218] and previous MD simulations [217].

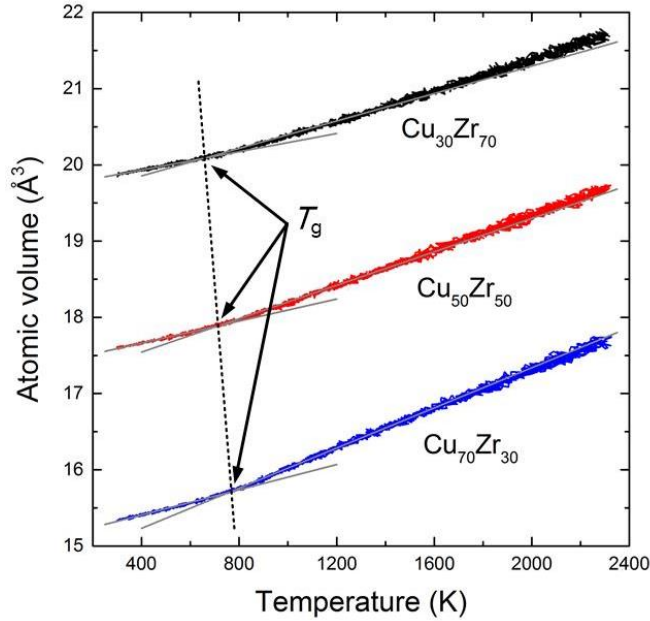


Figure 5-3. Volume-temperature relationships during cooling for $\text{Cu}_{30}\text{Zr}_{70}$, $\text{Cu}_{50}\text{Zr}_{50}$ and $\text{Cu}_{70}\text{Zr}_{30}$ systems.

Table 5-1. Calculated elastic constants and glass transition temperature T_g for $\text{Cu}_{30}\text{Zr}_{70}$, $\text{Cu}_{50}\text{Zr}_{50}$ and $\text{Cu}_{70}\text{Zr}_{30}$ metallic glass samples.

Composition	ρ (g/cc)	B (GPa)	G (GPa)	ν	c_B (km/s)	c_L (km/s)	T_g (K)
$\text{Cu}_{30}\text{Zr}_{70}$	6.918	95.62	23.38	0.388	3.72	4.31	657
$\text{Cu}_{50}\text{Zr}_{50}$	7.298	107.14	24.37	0.396	3.83	4.34	709
$\text{Cu}_{70}\text{Zr}_{30}$	7.782	115.76	26.52	0.395	3.86	4.40	753

Note: densities, elastic constants and sound speeds are obtained for zero temperature.

5.2.3 Piston-driven Shock Method

To produce the large-scale systems required for shock simulations, the small-size MG samples are replicated along the x , y and z directions. The $+x$ -axis is treated as the shock direction. The final cross-sectional sizes of the replicated systems are approximately $20 \times 20 \text{ nm}^2$. Cross-sections of 4.2×4.2 , 8.4×8.4 and $16.8 \times 16.8 \text{ nm}^2$ were simulated in Ref. [93] and no size-effects were found on the plastic deformation

behavior. The larger cross-section of our samples is mainly to provide better averages of thermodynamic properties extracted during shock compression simulations. The thickness of the sample along the x -axis is 800 nm when $U_p \leq 1.5$ km/s and 400 nm when $U_p \geq 1.8$ km/s. The 800-nm-thick samples consist of ~ 20 million atoms, while the 400-nm-thick samples consist of ~ 10 million atoms. Thicker samples are used for $U_p \leq 1.5$ km/s to allow for more time to track the evolution of the shock profile. At larger values of U_p , the shear stress goes to zero within a very short distance (< 50 nm) from the shock wave front, so thinner samples can be used.

Large-scale samples are equilibrated within the NPT ensemble at 300 K and zero pressure for 50 ps to remove possible artifacts from the replication process. After equilibration, the boundaries along the x -axis are set to free, that is there are free surfaces at the two ends; boundaries along the transverse dimensions remain periodic. Shock waves are generated in the equilibrated samples using the piston method [227]. A thin slab (2 nm) located at the left edge of the system is treated as the piston. At the start of the simulation, atoms inside the piston are assigned a uniform velocity along the $+x$ -axis and zero velocity along the transverse axes. Forces are zeroed for atoms within the piston at each time step. The piston velocity is ramped from 0 to U_p within 10 ps, thereby generating a compression wave within the sample. The final piston velocity U_p is varied from 0.125 to 2.5 km/s to obtain shocks of increasing strength. Shock simulations are carried out in the microcanonical (NVE) ensemble with a 1 fs time step.

Material response during shock wave propagation is monitored using one-dimensional profiles of thermodynamic properties. At the start of the simulation, the sample is divided along the x -axis into small 1-nm-thick slabs ($\sim 30,000$ atoms). During

the simulation, per-atom thermodynamic quantities are summed within each slab and over multiple time steps. The sums are then appropriately normalized to get one-dimensional profiles, which are outputted every 0.5 ps. Thermodynamic quantities used in the calculation of the profiles include the pressure tensor P_{ij} and temperature T , where T is the kinetic temperature after subtracting out the center-of-mass velocity of the slab along the x -axis. The shock pressure is P_{xx} and shear stress is $\tau = 0.5(P_{xx} - P_{yy})$ [84], where $P_{yy} \approx P_{zz}$ for the MG samples used in our simulations.

5.3 Simulation Results

5.3.1 Shock Wave Structure at Different Shock Intensities

Profiles of shock pressure P_{xx} and shear stress τ for $\text{Cu}_{50}\text{Zr}_{50}$ MG at three different piston velocities U_p are shown in Fig. 5-4. For $U_p = 0.125$ km/s, there is no obvious drop in shear stress following initial shock compression and the shear stress remains almost constant behind the shock wave front. Because no appreciable plastic deformation occurs at this stress level, the shock wave can be considered elastic. For $U_p = 0.5$ km/s, there is significant relaxation of shear stress within the shock, which indicates the MG has undergone plastic deformation and the final pressure state is above the Hugoniot elastic limit (HEL).

The shear stress reaches its peak value τ_{peak} rapidly following the initial compression by the elastic precursor, then drops as plastic deformation starts to develop. This is in contrast to previous MD shock compression simulations of $\text{Cu}_{54}\text{Zr}_{46}$ MG that used the Mendelev potential, where the start of plastic deformation did not necessarily coincide with the peak shear stress [93]. Tracking the position of the peak shear stress, a demarcation between the elastic precursor and start of the plastic wave front in the shock pressure profile can be identified, as shown in Fig. 5-4. Behind the

plastic shock wave front, the shear stress continues to relax as plastic flow develops. The flow stress τ_{flow} is defined as the average quasi-steady shear stress behind the plastic wave front.

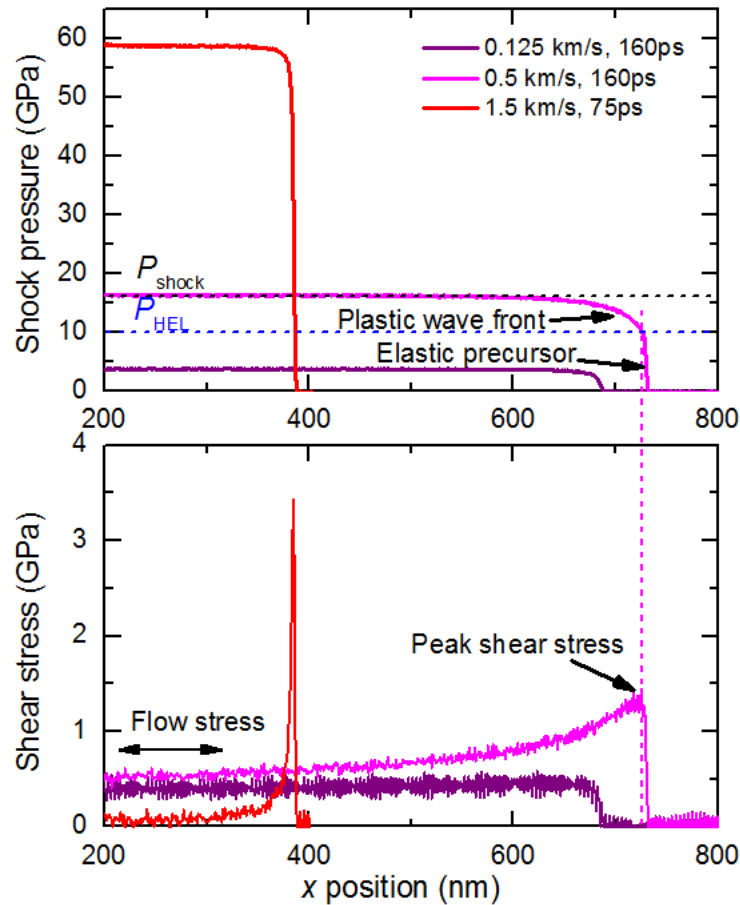


Figure 5-4. Shock wave profiles of shock pressure and shear stress from MD simulations of $\text{Cu}_{50}\text{Zr}_{50}$ metallic glass at $U_p = 0.125, 0.5$ and 1.5 km/s.

Previous MD simulations of shock compression of metallic single-crystals near the HEL show clearly-defined elastic and plastic wave structures with a clear separation between the elastic and plastic shock wave fronts [83,85,203,204]. However, for MGs it is difficult to distinguish the plastic wave front and elastic precursor clearly, as the plastic wave front is smooth and sluggishly rising with no clear separation from the

leading elastic precursor. Such behavior is similar to what has been observed in small-grain-size nanocrystalline metals where grain boundary motion dominates under shock compression [84,207,208,228]. At a much higher piston velocity, $U_p = 1.5$ km/s, the plastic shock wave has effectively overdriven the elastic precursor, which retains a small but finite width. Behind the shock wave front, the shear stress drops to nearly zero within a very short distance (~ 40 nm).

5.3.2 Hugoniot Elastic Limit

At the HEL, the material transitions from a pure elastic state to an elastic-plastic state. The shock pressure at the HEL is denoted by P_{HEL} . Equivalently, P_{HEL} is the amplitude of the elastic precursor when both elastic and plastic shock waves are present. As was already stated, the peak shear stress coincides with the onset of plastic deformation in our simulations. Thus, the peak shear stress also coincides with the location of the amplitude of the elastic precursor. Using the x-position of the peak shear stress, the corresponding amplitude of the elastic precursor can be obtained from the shock pressure profile as shown by the vertical dotted line in Fig. 5-4. This pressure P_{HEL} is shown by the blue horizontal dotted line. As the shock wave propagates through the sample, there is a gradual decay in P_{HEL} of $\sim 5 \times 10^{-3}$ GPa/nm. The observed decay rate is virtually independent of the MG composition.

Figure 5-5 shows P_{HEL} as a function of the final shock pressure for $Cu_{30}Zr_{70}$, $Cu_{50}Zr_{50}$ and $Cu_{70}Zr_{30}$ MGs. In addition to the gradual decay in P_{HEL} , there are also small fluctuations of ~ 0.1 GPa. To account for these effects, the data plotted in Fig. 5-5 represent averages over several profiles for a simulation at a given final shock pressure (or U_p) taken within a short time window of several ps. All three compositions show a similar linear dependence of P_{HEL} on the final shock pressure. In contrast, previous MD

shock compression simulations of $\text{Cu}_{46}\text{Zr}_{54}$ MG that used the Mendelev potential showed a constant P_{HEL} of ~ 7 GPa independent of the final shock pressure [93]. The pressure-independent HEL found for the Mendelev potential may be attributed to the unphysical behavior of the sound speed with compression shown in Fig. 5-1. Due to this behavior, it is possible the leading elastic wave does not steepen into a shock wave, which leads to the onset of plastic deformation at the same pressure level regardless of the final shock pressure. We define the minimum P_{HEL} to be the lowest shock pressure that results in plastic deformation behind the shock wave front subject to the length- and time-scale limitations of MD. Minimum P_{HEL} values measured in this work are 6.4, 7.0 and 7.3 GPa for $\text{Cu}_{30}\text{Zr}_{70}$, $\text{Cu}_{50}\text{Zr}_{50}$ and $\text{Cu}_{70}\text{Zr}_{30}$ MGs, respectively.

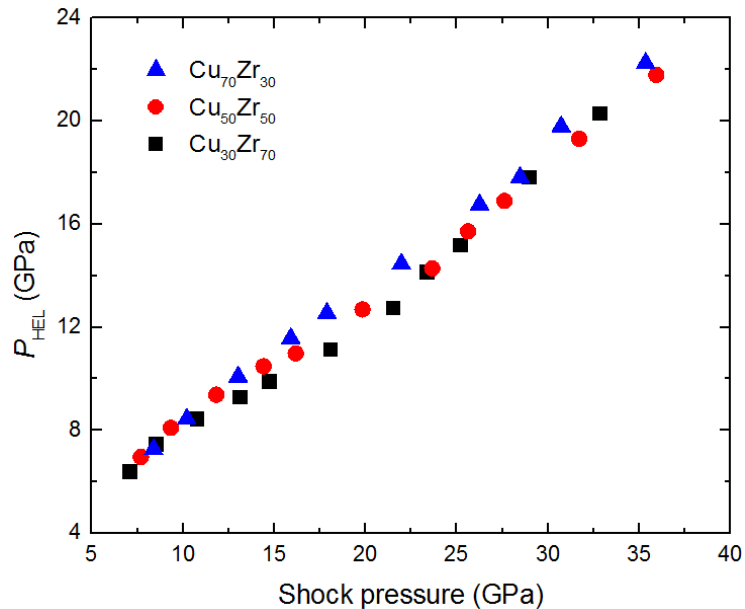


Figure 5-5. Shock pressure at the HEL P_{HEL} as a function of final shock pressure for $\text{Cu}_{30}\text{Zr}_{70}$, $\text{Cu}_{50}\text{Zr}_{50}$ and $\text{Cu}_{70}\text{Zr}_{30}$ metallic glass.

5.3.3 U_p - U_s Shock Hugoniot

The time-evolution of the shock pressure profile in $\text{Cu}_{50}\text{Zr}_{50}$ MG for two different piston velocities $U_p = 0.5$ and 1.5 km/s is shown in Fig. 5-6. The initial compression

wave created in the MG sample steepens as it propagates, which can be seen clearly in the inset of Fig. 5-6(a) as a converging of the $x-t$ contour levels starting from $t = 0$. At ~ 25 ps, the contour levels have converged, which indicates that the compression wave has broken into a shock. Parts of the sample that have not yet been affected by the shock wave have a pressure near zero and are shown in blue in Fig. 5-6, while areas that have been compressed to the final shock pressure are shown in red. For the overdriven plastic shock wave shown in Fig. 5-6(a), the boundary region between these two states is very narrow and can be approximated by a single line, the slope of which roughly corresponds to the shock velocity U_s . A similarly narrow boundary region is also observed for elastic shock waves with amplitudes $< P_{\text{HEL}}$.

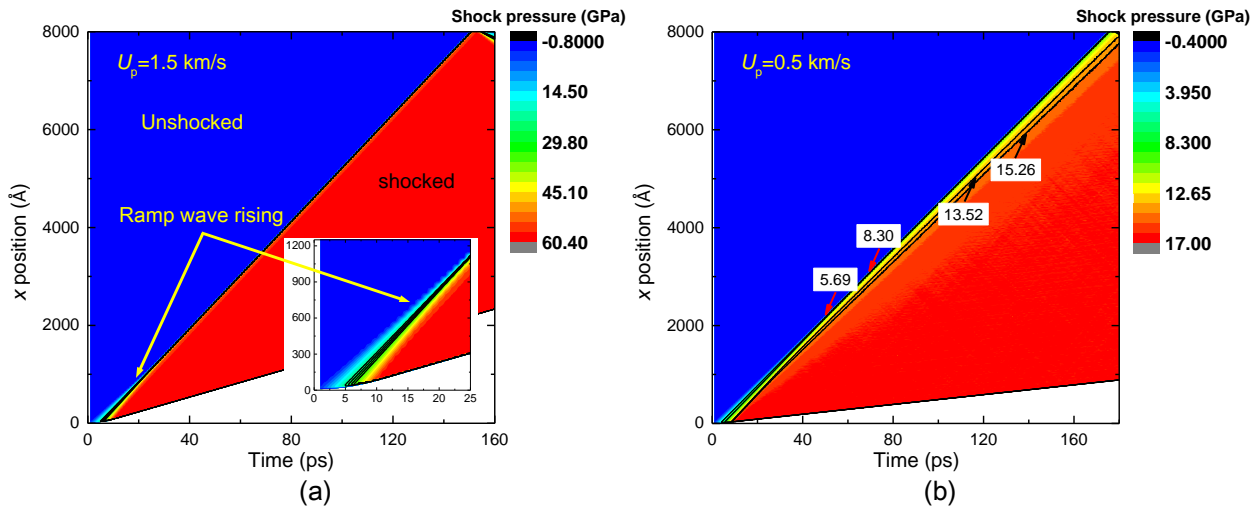


Figure 5-6. Shock pressure distributions at different times and positions for $\text{Cu}_{50}\text{Zr}_{50}$ metallic glass at (a) $U_p = 1.5$ km/s and (b) $U_p = 0.5$ km/s.

However, when there is an elastic-plastic two-wave structure, as is this case for $U_p = 0.5$ km/s, there is ambiguity in the location the plastic shock wave front. This ambiguity can be attributed to the sluggishly rising nature of the plastic front, which is evident from the wide transition region between the unshocked and shocked regions of

the sample in Fig. 5-6(b). By using an appropriate value of the shock pressure P_{xx} , the positions of the elastic and plastic fronts as a function of time are extracted from the simulation. The elastic and plastic shock wave velocities are then estimated from the slopes of the corresponding trajectories. To track the elastic precursor, a P_{xx} level with a value $< P_{HEL}$ is used. For $Cu_{50}Zr_{50}$ MG, P_{HEL} is ~ 11 GPa when $U_p = 0.5$ km/s. Taking P_{xx} levels at 5.7 and 8.3 GPa gives elastic precursor velocities of 4.653 and 4.649 km/s, respectively, which is a difference of $< 0.1\%$. Therefore, we conclude that the elastic precursor velocity is insensitive to the exact choice of the P_{xx} tracking level provided it is $< P_{HEL}$. This insensitivity can be attributed to the sharp rise and narrow width ($\sim 5\text{--}10$ nm) of the elastic precursor.

In contrast, the plastic shock wave velocity is sensitive to the choice of the P_{xx} level used to track its motion through the sample. For example, taking P_{xx} levels of 13.52 and 15.26 GPa for the plastic front, gives velocities of 4.54 and 4.32 km/s, respectively, which is a difference of 4.8%. To calculate the plastic shock wave velocity in a way that is consistent for different shock intensities and compositions, we set the P_{xx} level to track the plastic front equal to the median pressure in the plastic shock $(P_{shock} + P_{HEL})/2$, where P_{shock} is the final steady shock pressure and P_{HEL} is the pressure at the peak shear stress. Note P_{HEL} depends on the final shock pressure and MG composition as is shown in Fig. 5-5. The $U_p\text{--}U_s$ relationships for shock compression of $Cu_{30}Zr_{70}$, $Cu_{50}Zr_{50}$ and $Cu_{70}Zr_{30}$ MGs obtained from MD are plotted in Fig. 5-7.

The $U_p\text{--}U_s$ plots shown in Fig. 5-7 can be broken down into three regions. When $U_p < 0.25$ km/s (region I), shear stress relaxation behind the shock wave front is negligible and a single elastic shock wave develops with an amplitude $< P_{HEL}$. As U_p is

increased beyond 0.25 km/s, plastic deformation occurs behind the elastic shock wave front and a plastic wave develops. Within the interval $0.25 < U_p < 0.75$ km/s (region II), the plastic wave velocity is less than that of the elastic precursor and the two waves separate during propagation. However, the rate of increase of the plastic wave velocity within this interval is greater than that of the elastic precursor. When $U_p > 0.75$ km/s (region III), both the elastic precursor and plastic wave have the same velocity and propagate as a single elastic-plastic shock wave.

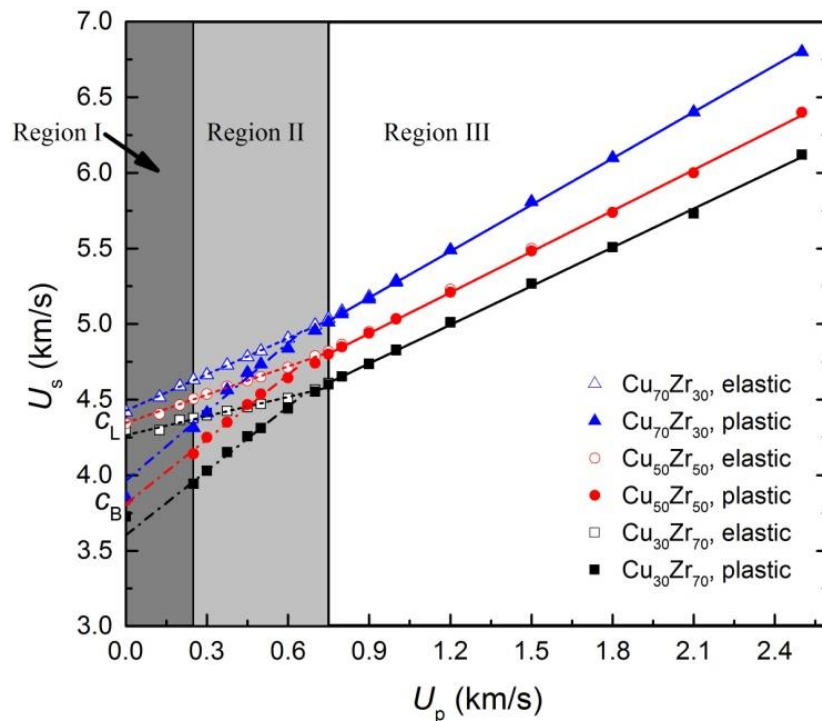


Figure 5-7. Shock velocity U_s as a function of piston velocity U_p for Cu₃₀Zr₇₀, Cu₅₀Zr₅₀ and Cu₇₀Zr₃₀ metallic glass.

The U_p-U_s data for each MG composition are found to exhibit approximately piecewise linear behavior and are fit to relationships of the form $U_s = c_0 + sU_p$, where c_0 and s are fitting parameters. Each elastic branch is best described by a single linear relationship, while each plastic branch is best described by two different linear

relationships: one for region II and another for region III. Table 5-2 gives the best-fit parameters for both the elastic and plastic branches of the U_p - U_s Hugoniot for $\text{Cu}_{30}\text{Zr}_{70}$, $\text{Cu}_{50}\text{Zr}_{50}$ and $\text{Cu}_{70}\text{Zr}_{30}$ MGs. Both c_0 and s increase with increasing Cu content for all three regions. The increase in c_0 is expected as $c_0 \approx c_B$ for the plastic branch and $c_0 \approx c_L$ for the elastic branch and, as can be seen in Table 5-1, both c_B and c_L increase with increasing Cu content.

Table 5-2. Calculated parameters for both the elastic and plastic branches of the U_p - U_s Hugoniot for $\text{Cu}_{30}\text{Zr}_{70}$, $\text{Cu}_{50}\text{Zr}_{50}$ and $\text{Cu}_{70}\text{Zr}_{30}$ metallic glass.

Composition	Elastic (regions I & II)		Plastic (region II)		Plastic (region III)	
	c_0 (km/s)	s	c_0 (km/s)	s	c_0 (km/s)	s
$\text{Cu}_{30}\text{Zr}_{70}$	4.26	0.42	3.60	1.42	3.97	0.85
$\text{Cu}_{50}\text{Zr}_{50}$	4.35	0.62	3.81	1.43	4.13	0.90
$\text{Cu}_{70}\text{Zr}_{30}$	4.43	0.80	3.96	1.52	4.25	1.02

Note: the standard errors in c_0 and s are $< 1\%$ and $< 7\%$, respectively.

5.3.4 Composition Dependence of the Shock Response

Shock wave profiles at $U_p = 1.5$ km/s for $\text{Cu}_{30}\text{Zr}_{70}$, $\text{Cu}_{50}\text{Zr}_{50}$ and $\text{Cu}_{70}\text{Zr}_{30}$ MG are shown in Fig. 5-8. Profiles are taken at 100 ps after the initial piston compression. As Cu content increases from 30% to 70%, the shock pressure increases from 54 to 66 GPa. This is consistent with the increase in bulk modulus with increasing Cu content of the MG, as shown in Table 5-1. Figure 5-8 also shows that τ_{peak} increases towards Cu-rich MG compositions. The dependence of the stress state on Cu content is nonlinear. For example, at $U_p = 1.5$ km/s, $\tau_{\text{peak}} = 2.7$ GPa for $\text{Cu}_{30}\text{Zr}_{70}$, while $\tau_{\text{peak}} = 3.2$ GPa for

Cu₅₀Zr₅₀, which is an increase of ~18%. However, $\tau_{\text{peak}} = 4.7$ GPa for Cu₇₀Zr₃₀, which is an increase of 47% over that of Cu₅₀Zr₅₀.

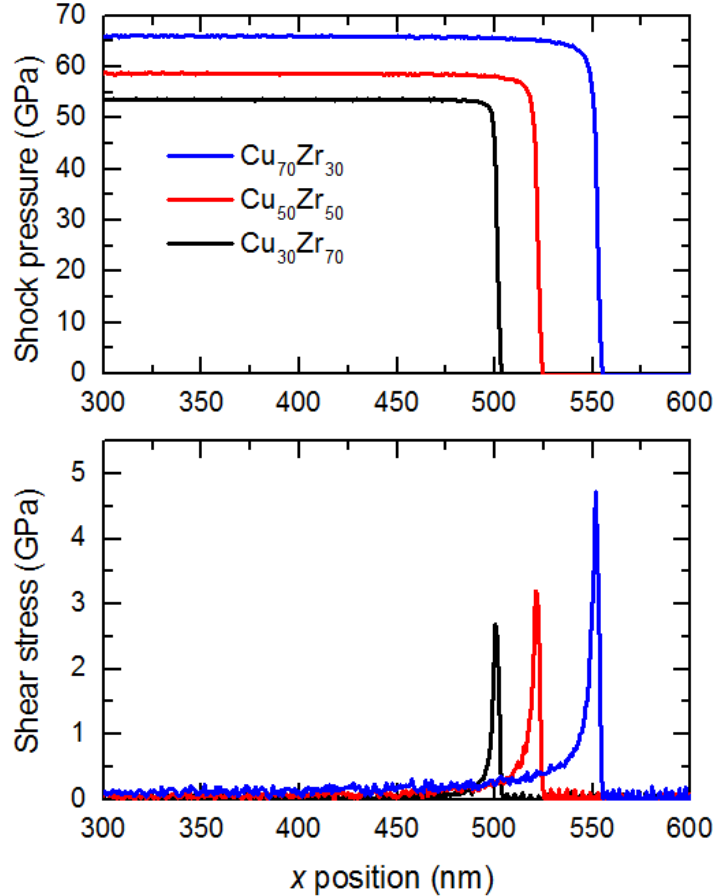


Figure 5-8. Shock wave profiles at $t = 100$ ps for Cu₃₀Zr₇₀, Cu₅₀Zr₅₀ and Cu₇₀Zr₃₀ metallic glass samples at $U_p = 1.5$ km/s.

The temperature of the material in the aftershock flow is plotted in Fig. 5-9 as a function of the final shock pressure. In the figure, the dashed vertical line indicates departure from linear behavior at low shock pressures. For shock pressures < 25 GPa, the temperature increases almost linearly. This is true for all three MG compositions. The temperature increase from elastic deformation is independent of composition and is modest. At shock pressures > 25 GPa, the temperature starts to show significant deviations from linearity. As we know, the temperature reflects the intensity of the

movement of atoms and local structures (STZs for MGs). The higher the temperature, the more intense the activities of STZs for MGs. The shock-induced temperature change decreases with increasing Cu content for the same shock pressure. When the shock pressure is around 60 GPa, the temperature of $\text{Cu}_{30}\text{Zr}_{70}$ MG is ~ 130 K higher than $\text{Cu}_{70}\text{Zr}_{30}$ MG. This indicates that Zr has a more important effect on temperature rise than Cu.

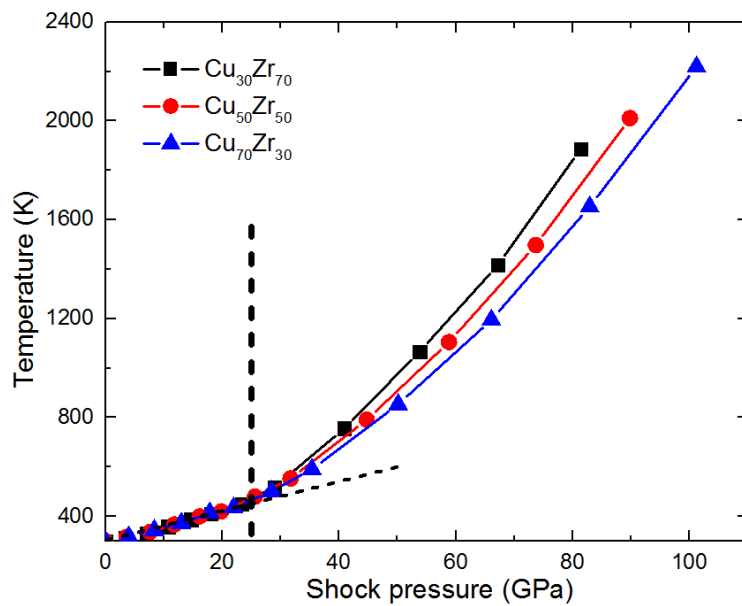


Figure 5-9. Shock-induced temperatures as a function of shock pressure.

Figure 5-10 shows τ_{peak} and τ_{flow} as a function of the final shock pressure. The peak shear stress coincides with the start of plastic deformation in our simulations provided the final shock pressure $> P_{\text{HEL}}$. Thus, the peak shear stress τ_{peak} is a measure of the critical shear stress necessary to initiate plastic flow within the pristine glass under compression by the elastic precursor. The flow stress τ_{flow} is the average of the residual shear stress far away from the plastic shock wave front and gives a measure of the strength of the material within the aftershock flow.

The peak shear stress increases with increasing shock pressure (states A–C in Fig. 5-10(a)) until reaching a maximum value (state D) that is dependent upon the composition of the MG. Beyond this maximum, τ_{peak} decreases indicating softening of the MG. As τ_{peak} corresponds to the shear strength of the initial elastically-compressed MG structure without existing STZs to facilitate plastic flow, the softening must be thermal in nature. The higher the Cu content of the MG, the higher the maximum value of τ_{peak} and the higher the shock pressure required before the MG starts to soften. For example, τ_{peak} reaches a maximum value of ~ 2.8 GPa at a shock pressure of ~ 53 GPa for $\text{Cu}_{30}\text{Zr}_{70}$ MG, whereas τ_{peak} reaches a maximum value of ~ 4.8 GPa at a shock pressure of ~ 82 GPa for $\text{Cu}_{70}\text{Zr}_{30}$ MG.

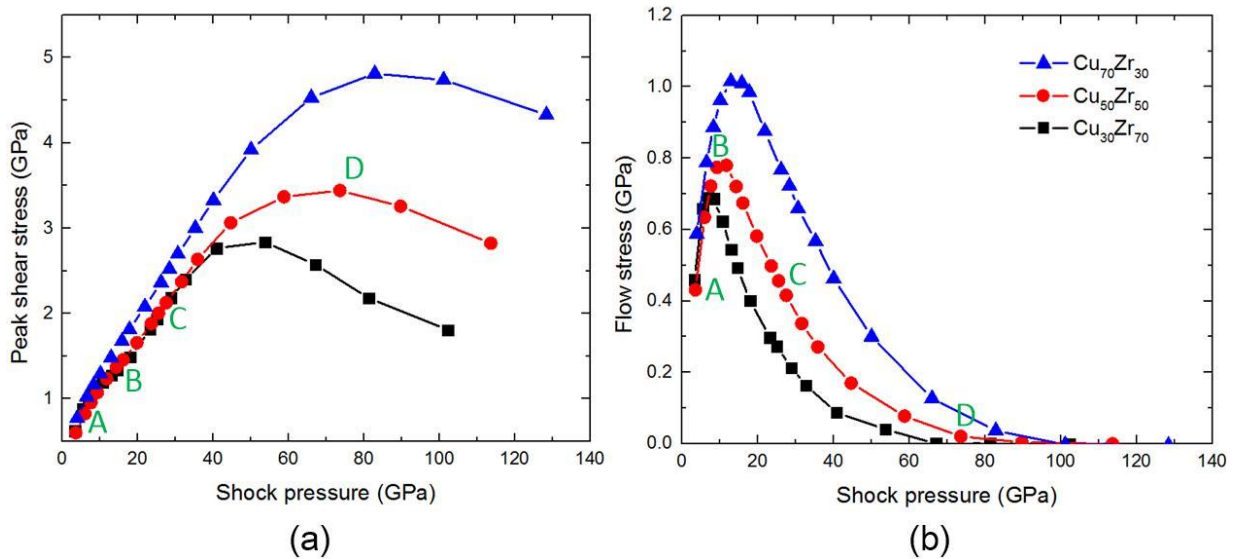


Figure 5-10. (a) Peak shear stress and (b) flow stress as a function of the final shock pressure.

The flow stress τ_{flow} increases at low shock pressures (state A in Fig. 5-10(b)), where the shock deformation is principally elastic, then reaches a maximum value at the onset of plastic deformation (state B). At a given shock pressure, τ_{flow} increases with

increasing Cu content, i.e., $\text{Cu}_{30}\text{Zr}_{70}$ and $\text{Cu}_{50}\text{Zr}_{50}$ MGs both yield more easily than $\text{Cu}_{70}\text{Zr}_{30}$. As was discussed about Fig. 5-8, the dependence of the stress state on composition is nonlinear. For example, the maximum value of τ_{flow} for $\text{Cu}_{30}\text{Zr}_{70}$ and $\text{Cu}_{50}\text{Zr}_{50}$ MGs are ~ 0.7 and ~ 0.8 GPa, respectively, while for $\text{Cu}_{70}\text{Zr}_{30}$ τ_{flow} has a maximum value of ~ 1.0 GPa.

Beyond its maximum value, τ_{flow} starts to decrease with increasing shock pressure (state C in Fig. 5-10(b)). Such softening was also observed in previous MD simulations of shock compression of $\text{Cu}_{46}\text{Zr}_{54}$ [93] and $\text{Cu}_{46}\text{Zr}_{46}\text{Al}_8$ [210] MGs, where it was attributed to a combination of thermal softening due to shock heating and strain softening due to formation of STZs and subsequent strain localization. At high shock strengths, τ_{flow} goes to zero (state D) indicating a complete loss of strength for the material within the aftershock flow. The point at which this transition occurs is sensitive to the MG composition. For $\text{Cu}_{30}\text{Zr}_{70}$, $\text{Cu}_{50}\text{Zr}_{50}$ and $\text{Cu}_{70}\text{Zr}_{30}$, loss of flow strength occurs when the shock pressure (temperature) is ~ 67 GPa (1400 K), ~ 73 GPa (1500 K) and ~ 100 GPa (2200 K), respectively. Clearly, increased Cu content leads to an increased resistance to plastic flow that persists up to very high shock pressures.

The Cu-Cu RDFs for $\text{Cu}_{50}\text{Zr}_{50}$ corresponding to states A–D are shown in Fig. 5-11. The RDFs are calculated for a 50-nm slice of material along the x -axis far behind the plastic shock wave front (not at the peak stress state). For states A–C, the glassy structure is largely maintained after shock compression, while for state D the split in the second peak has been reduced significantly indicating a transformation to a more liquid-like structure. However, from this analysis alone, it is not clear whether the change in

the local structure can be attributed to melting. The issue of shock-induced melting will be examined in detail in Chapter 6.

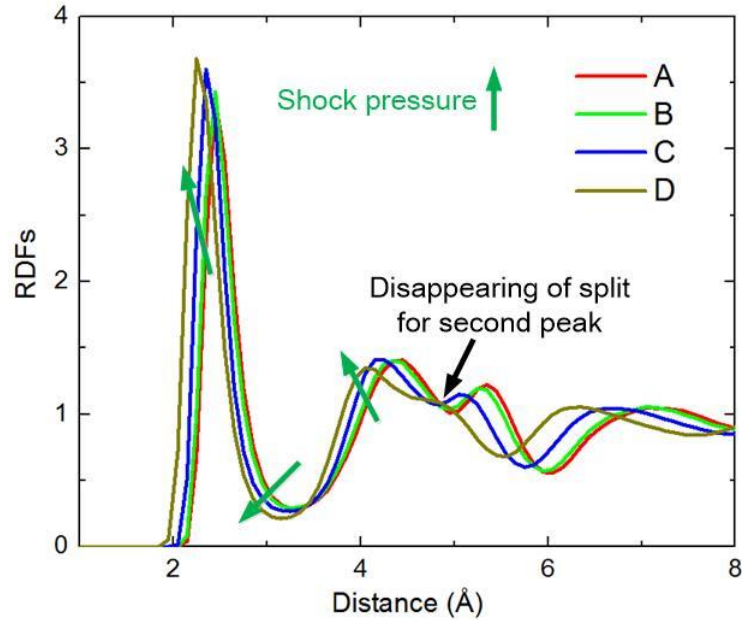


Figure 5-11. Cu-Cu RDFs in the aftershock flow of Cu₅₀Zr₅₀ metallic glass for four different shock intensities.

5.4 Discussion

5.4.1 Pressure-dependent Yield Criterion

Our MD simulations show, independent of Cu composition, that P_{HEL} increases with increasing shock intensity, see Fig. 5-5. The mean pressure $P_m = (P_{xx} + 2P_{yy})/3$ at the HEL increases with increasing shock strength, therefore P_{HEL} increases with the magnitude of the confining stress. Several impactor-based shock experiments on multi-component MGs have also observed a similar pressure-dependent HEL [57,60,200]. Figure 5-12 shows P_{HEL} as a function of P_m at the HEL for our MD simulations along with experimental data from Refs. [57,60,200]. In experiment, transverse pressure information is not available, so P_m is calculated by assuming a constant Poisson's ratio. Based on our MD simulations, the assumption of a constant Poisson's ratio leads to an

error in P_m of ~5%. Good agreement between our MD simulation data and shock compression experiments on a variety of different multi-component MGs suggests that a pressure-dependent HEL is a universal feature of MGs.

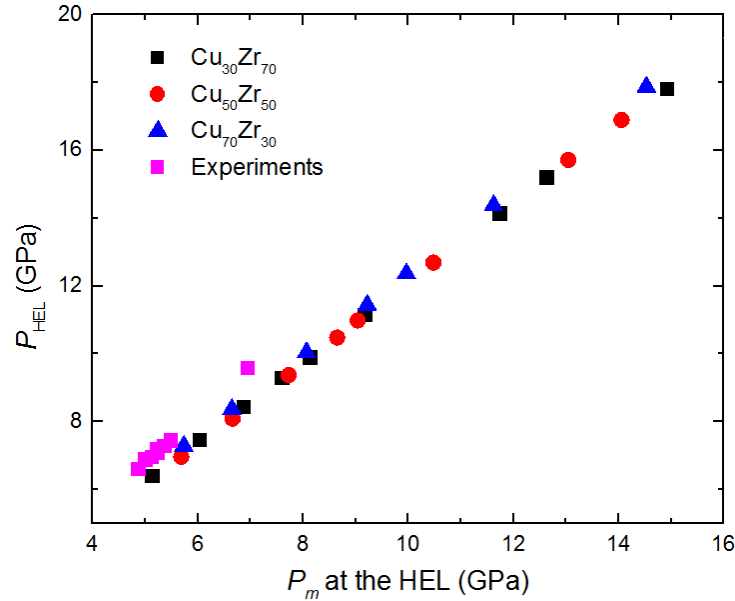


Figure 5-12. Shock pressure at the HEL P_{HEL} versus mean pressure P_m at the HEL.

Pressure-dependent yield behavior has been observed in MGs under many different loading conditions [229–235] and several different variants of yield criteria for MGs that account for the effect of non-shear components of the pressure tensor have been proposed [2]. Lu and Ravichandran found that the yield strength of $Zr_{41.2}Ti_{13.8}Cu_{12.5}Ni_{10}Be_{22.5}$ MG (Vitrelloy 1 [236]) measured in quasistatic compression tests was well described by a pressure-dependent Tresca criterion of the form $Y = Y_0 + \beta P_m$ with $\beta = 0.34$ [234]. In our MD simulations, the yield strength $Y = 2T_{peak}$, where T_{peak} is the peak shear stress obtained from the shock profiles. Fitting the yield strength data as a function of P_m at the yield point for our simulated MGs, we obtain $\beta = 0.26–0.3$. The difference in β between simulation and experiment may be attributed to different

compositions of MGs as well as differences in sample preparation, specifically the fact that the cooling rate used to form the MGs in our MD simulations is many orders of magnitude higher than in experiment.

5.4.2 Bilinear U_p-U_s Hugoniot

Our simulated U_p-U_s Hugoniot data exhibit a plastic branch characterized by approximately bilinear behavior with a change in slope occurring at the point when the plastic wave overtakes the leading elastic precursor, i.e., at the transition from region II to region III in Fig. 5-8. The shock response of $Zr_{51}Ti_5Ni_{10}Cu_{25}Al_9$ MG was investigated in two separate experiments [65,200]. Both experiments found an elastic-plastic response with P_{HEL} ranges that were consistent with one another. The plastic branches of the U_p-U_s Hugoniot curves for both experiments were found to exhibit good linearity. However, when both sets of U_p-U_s data are combined, a kink appears at a shock pressure of ~ 18 GPa ($U_p \sim 0.55$ km/s). In our MD simulations, the transition from region II to region III occurs at a shock pressure of ~ 25 GPa ($U_p \sim 0.75$ km/s). On the one hand, the fact that both experiments and simulation agree on the existence of a change in slope in the U_p-U_s Hugoniot data suggests that our results may not necessarily be an artifact of the limited length- and time-scales of MD simulation. On the other hand, previous MD simulation results for $Cu_{46}Zr_{54}$ MG showed no such change of slope with the plastic branch exhibiting good linearity throughout the entire range of shock pressures [93]. Therefore, further work is needed to determine the origin of the change in slope observed in the plastic branch of our simulated U_p-U_s Hugoniot data.

5.5 Summary

The shock response of Cu_xZr_{100-x} ($x = 30, 50$ and 70) MG has been investigated over a wide range of shock intensities using large-scale MD simulations. A two-wave

elastic-plastic structure is found for all three compositions. At low shock pressures, the plastic wave propagates more slowly than the leading elastic shock wave and the two waves separate over time. As shock pressure is increased, the plastic wave eventually catches up to the elastic precursor and the two form a single shock wave structure. Within the split wave and overdriven regimes, the amplitude of the elastic precursor P_{HEL} is found to increase with increasing confining stress, thereby indicating a pressure-dependent yield criterion for the simulated $\text{Cu}_x\text{Zr}_{100-x}$ MGs. The U_p-U_s data for the plastic branch of the Hugoniot were found to exhibit approximately bilinear behavior with the slope gradually decreasing as the velocity of the plastic wave approaches that of the elastic precursor.

The Cu content of the MG is found to have a significant effect on the shock-induced elastic-plastic transition with resistance to plastic deformation increasing towards Cu-rich compositions. Specifically, MGs with higher Cu content can support larger shear stresses before yielding both within the pristine glass and within the aftershock flow. Previous MD simulations [219] have shown such composition dependence to be a result of changes to the local structure of the MG. In Chapter 6, the microscopic deformation behavior of $\text{Cu}_x\text{Zr}_{100-x}$ MGs under shock loading will be examined in detail. Emphasis will be placed on how such changes depend on the intensity of the shock and the Cu content of the MG.

CHAPTER 6
MICROSTRUCTURAL RESPONSE OF METALLIC GLASSES TO SHOCK LOADING

6.1 Background

The Cu-Zr system has served a prototypical role in both experiment and MD simulations owing to its good glass-forming ability over a wide composition range [216,218,237–239] and availability of interatomic potentials [217,240,241]. Often new insights gained from studying this system are applicable to other metal-metal binary MGs as well as Zr- and Cu-based multicomponent MGs. Both experiments and MD simulations have shown that the mechanical behavior of Cu-Zr MGs is sensitive to composition. Quasistatic uniaxial compression experiments found increasing yield strength and decreasing plastic strain as Cu content increases from 46% to 65% [216]. Moreover, MD simulations of shearing, uniaxial and tensile loading of Cu-Zr MGs at high strain rates found that the yield strength and the propensity for strain localization increase as Cu content increases from 30% to 70% [219].

The fundamental unit of plastic deformation in MGs is the shear transformation zone (STZ), which is a small cluster of atoms that undergoes a shear event in response to an applied shear stress [2,47,242–245]. Even in monolithic glasses, there are fluctuations and variations in the short-range order (SRO) that lead to regions of low elastic stiffness or low stability [245–248]. Such sites serve as prime candidates for STZ initiation. The structure of Cu-Zr MGs is best understood from the perspective of efficient packing of Cu-centered clusters [245]. MD simulations have shown that as Cu content increases, the average coordination number around Cu increases towards twelve and the fraction of Cu-centered icosahedral clusters grows dramatically [217,219]. Another MD study found that regions of high icosahedral order within

Cu₅₀Zr₅₀ MG were more resistant to plastic flow than regions where icosahedral order was low [249].

Shock waves have long been used as a tool to measure the dynamic strength of materials at high strain rates $> 10^5 \text{ s}^{-1}$. While several impactor-based shock experiments have been performed on a variety of different MGs [57–64], measurements performed during shock propagation are limited to surface displacements or velocities, and microstructural data related to internal deformation of the sample can only be obtained after shock release. However, MD simulations have access to the complete dynamic response of the system at all stages of shock compression, while overlapping with the upper range of strain rates attainable in experiment. Therefore, they offer a unique opportunity to study the microscopic deformation behavior of MGs at high strain rates. A few MD simulations have already investigated the shock response of Cu-Zr MGs [91,93,211]. However, such studies focused on a single MG composition, so changes in the plastic deformation behavior due to changes in composition were not addressed.

To this end, we perform MD simulations to investigate the microstructural deformation behavior of Cu_xZr_{100-x} MGs under shock loading. This builds on the work done in Chapter 5, which focused mainly on the shock wave structure and Hugoniot states. We take x to be 30%, 50% and 70%, which corresponds to the same compositions used in Chapter 5 and also overlaps with the composition ranges used in the experiments [216] and MD simulations [219] mentioned above. We show that localized shear regions or STZs are the main carrier of plastic deformation in the simulated MGs. Near the onset of elastic-plastic behavior, STZ activity is inhomogeneous, but becomes more homogeneous as shock intensity increases. Shock-

induced melting is shown to occur at the highest shock intensities. Plastic strain within the aftershock flow is found to decrease with increasing Cu content of the MG. Changes in the SRO of the MGs are analyzed from the perspective of Cu-centered clusters. Icosahedral clusters are shown to be the most stable during shock compression.

6.2 Simulation Methods

MD simulations are performed using LAMMPS [140]. Interatomic interactions are described by an EAM potential for the Cu-Zr(-Al) system developed by Cheng et al. [224]. In contrast, previous MD studies on shock compression of Cu-Zr MGs [91,93] used the Finnis-Sinclair EAM potential developed by Mendeleev et al. [223]. Following the work in Chapter 5, the Cheng potential is chosen as it exhibits good behavior under compression. Initial structures consist of a $7.5 \times 7.5 \times 7.5 \text{ nm}^3$ cube of $\sim 24,000$ Cu and Zr atoms arranged in the B2 (CsCl-type) structure with periodic boundary conditions along x , y and z . Depending on the desired composition, an appropriate fraction of Cu or Zr atoms is randomly replaced by atoms of the opposite type.

Initial structures are heated at a constant rate of 10 K/ps to a temperature of 2300 K. As was shown in Chapter 5, this temperature is high enough to ensure that the initial structures have completely melted. After heating, the melts are equilibrated at 2300 K for 200 ps. Samples are then cooled at a rate of 10 K/ps to a final temperature of 300 K. The high cooling rate inhibits crystallization resulting in glass formation. The amorphous structure of the samples was confirmed using similar analysis to what was performed in Chapter 5. The cooling rate of 10 K/ps is comparable to previous MD simulations [91,93,209,211]. Glass formation simulations are carried out in the isobaric-isothermal (NPT) ensemble with a target pressure of zero and a time step of 2 fs.

To generate the large-scale samples required for shock compression simulations, the amorphous structures obtained following cooling are replicated along the x , y and z directions. The shock direction is chosen as the $+x$ -axis. Sample dimensions after replication are $797.2 \times 19.5 \times 18.2$, $798.2 \times 22.8 \times 21.9$ and $799.1 \times 22.6 \times 21.4$ nm³ for Cu₃₀Zr₇₀, Cu₅₀Zr₅₀ and Cu₇₀Zr₃₀ MGs, respectively. The large size along the x -axis is used to allow more time for relaxation processes occurring behind the shock wave front to develop. As was stated in Chapter 5, the cross-sections of our samples are larger than those used in previous MD shock simulations [90,93]. The as-replicated samples are heated at 10 K/ps to 700 K and then annealed for 200 ps in the NPT ensemble at a target pressure of zero. The annealing step is performed to reduce the long-range order in the sample produced by the replication process. After annealing, the samples are cooled at a rate of 10 K/ps to 300 K. Shock compression simulations are performed using the piston method described in Chapter 5.

Material response during shock wave propagation is monitored using the 1D binning analysis described in Chapter 5. Profiles of the pressure tensor P_{ij} and temperature T are calculated, where T is the kinetic temperature subtracting out the center-of-mass velocity of each slab along the x -axis. Shear stress $\tau = 0.5(P_{xx} - P_{yy})$ profiles are also calculated, where $P_{yy} \approx P_{zz}$ for the MG samples used in our simulations. The mean square displacement (MSD) of atoms in the aftershock flow is calculated to test for shock-induced melting. Because of the nonzero flow velocity of atoms along the x -axis, only displacements along the y and z dimensions are used in the calculation of the MSD.

Plastic deformation of the MG during shock compression is monitored using the von Mises shear strain η_i^{VM} [250]. Calculation of η_i^{VM} requires two atomic configurations, one current, and one reference. The sample after annealing is used as the reference atomic configuration. Variations of < 1 GPa and < 3% are found in the local pressure tensor and composition for the reference configurations for each of the three MG compositions. To calculate η_i^{VM} , first a local transformation matrix \mathbf{J}_i is determined that best maps

$$\{\mathbf{d}_{ji}^0\} \rightarrow \{\mathbf{d}_{ji}\}, \quad \forall j \in N_i^0, \quad (6-1)$$

where \mathbf{d}_{ji} is the separation (row) vector between atoms i and j (0 denotes the reference configuration). In Eq. 6-1, atom j is one of atom i 's nearest neighbors and N_i^0 is the total number of nearest neighbors of atom i at the reference configuration within some cutoff distance. In all our calculations, the cutoff distance is chosen as 4.5 Å. The local transformation matrix \mathbf{J}_i for each atom is determined by minimizing

$$\sum_{j \in N_i^0} |\mathbf{d}_{ji}^0 \mathbf{J}_i - \mathbf{d}_{ji}|^2. \quad (6-2)$$

The strain matrix $\boldsymbol{\eta}_i$ for each atom is computed as

$$\boldsymbol{\eta}_i = \frac{1}{2} (\mathbf{J}_i \mathbf{J}_i^T - \mathbf{I}), \quad (6-3)$$

where T represents the transpose and \mathbf{I} is the identity matrix. The local von Mises shear strain η_i^{VM} for each atom is then given by

$$\eta_i^{\text{VM}} = \left\{ \frac{1}{6} [(\eta_{11} - \eta_{22})^2 + (\eta_{22} - \eta_{33})^2 + (\eta_{33} - \eta_{11})^2] + \eta_{12}^2 + \eta_{23}^2 + \eta_{31}^2 \right\}^{1/2}, \quad (6-4)$$

where the index i in the components of the strain matrix η_i is omitted for clarity.

The SRO of the MG is characterized using a polydisperse Voronoi tessellation analysis [251], where the atomic radii for Cu and Zr are 128 and 160 pm, respectively. The Voronoi polyhedron associated with each atom is labeled by a set of indices $\langle n_3, n_4, n_5, n_6 \rangle$, where n_i is the number of faces with i vertices. For example, the Voronoi polyhedron with indices $\langle 0, 0, 12, 0 \rangle$ is composed of 12 faces each face having 5 vertices/edges. In a perfect *fcc* or *bcc* crystal, there is only a single unique Voronoi polyhedron with indices of $\langle 0, 12, 0, 0 \rangle$ or $\langle 0, 6, 0, 8 \rangle$, respectively. When performing the Voronoi tessellation, any faces having areas less than 1% of the total polyhedron surface area are deleted to reduce effects of degeneracy and thermal vibration [252]. The coordination number CN of each atom is equal to the sum of the faces of its corresponding Voronoi polyhedron, i.e., $CN = \sum_i n_i$. Visualization of the simulation snapshots, Voronoi tessellation analysis and calculation of η_i^{VM} are performed using the OVITO software package [253].

6.3 Simulation Results

6.3.1 Shock-induced Deformation

Shock compression simulations are performed for $\text{Cu}_{50}\text{Zr}_{50}$ MG varying U_p from 0.125 to 2.0 km/s. Figure 6-1 shows shock pressure P_{xx} and shear stress profiles at $t = 125$ ps for $U_p = 0.125, 0.375, 0.875$ and 1.75 km/s. At the lowest piston velocity, $U_p = 0.125$ km/s, the shear stress level behind the shock wave front is nearly constant. For example, the average shear stress in a 100-nm-thick slab immediately behind the shock wave front is 0.50 GPa, while 550 nm behind the shock wave front the average shear stress is 0.47 GPa. Therefore, shear stress relaxation is minimal, and the shock can be considered elastic at this low piston velocity.

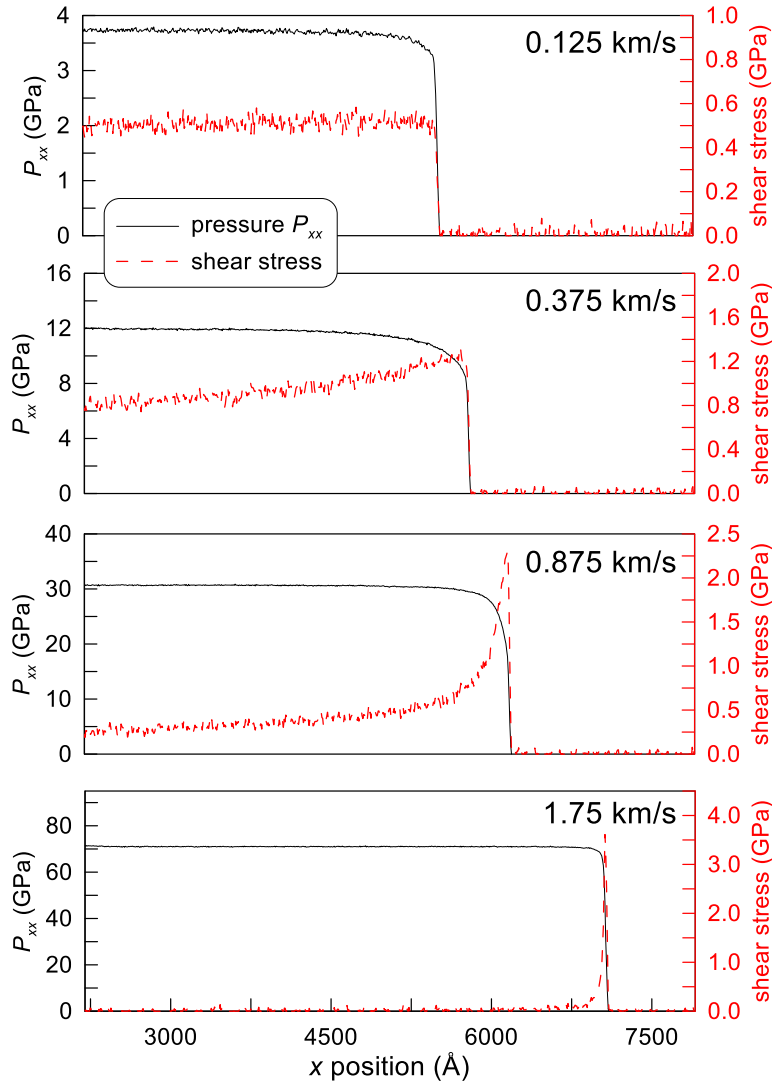


Figure 6-1. Pressure P_{xx} and shear stress profiles at $t = 125$ ps for $\text{Cu}_{50}\text{Zr}_{50}$ metallic glass at different piston velocities.

When U_p is increased to 0.375 km/s, shear stress relaxation behind the shock wave front is apparent, which indicates the material has undergone some plastic deformation. This is consistent with the results presented in Chapter 5 that showed the onset of plasticity occurs near $U_p = 0.25$ km/s. However, the relaxation process is slow and a significant residual shear stress, or flow stress τ_{flow} , remains far behind the shock front. As U_p is increased further to 0.875 km/s, the shear stress relaxation becomes more rapid and more complete, as indicated by the sharp drop in shear stress behind

the shock front and a smaller τ_{flow} level. This softening trend continues with increasing shock strength. At $U_p = 1.75$ km/s, the shear stress goes to zero within ~ 50 nm behind the shock front.

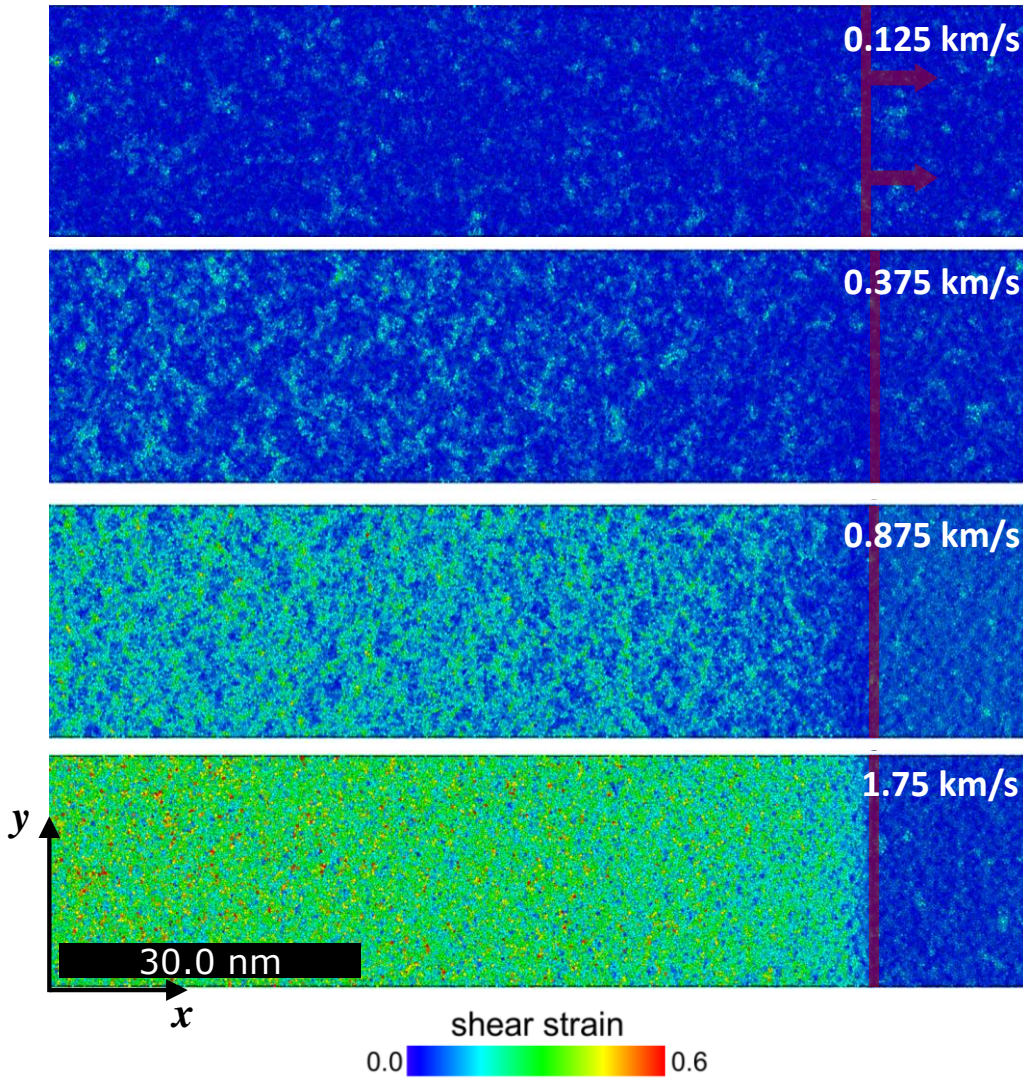


Figure 6-2. Snapshots of von Mises shear strain for Cu₅₀Zr₅₀ metallic glass at different piston velocities. Position of the shock front in each snapshot is denoted by a vertical line.

Snapshots of the atomic shear strain η_i^{VM} for Cu₅₀Zr₅₀ are shown in Fig. 6-2 for the same values of U_p plotted in Fig. 6-1. In each snapshot, the location of the shock front is denoted by a vertical line. For the shock wave generated at $U_p = 0.125$ km/s,

material behind the shock front has no perceptible change in η_i^{VM} relative to the ambient state ahead of the shock front. This confirms that the deformation is almost completely elastic. The average η_i^{VM} in the ambient unshocked material is ~ 0.04 , which is in agreement with previous MD shock simulations in $\text{Cu}_{46}\text{Zr}_{54}$ MG performed using the Mendelev potential [93].

At $U_p = 0.375$ km/s, a small number of STZs have nucleated behind the shock front. These STZs are isolated from one another and are embedded in a matrix of material with low η_i^{VM} (near the ambient value). Further behind the shock front, there is some growth and interconnection of STZs, but, for the most part, they remain spatially separated. The average temperatures of the STZs are similar to the temperature of the surrounding matrix, which indicates STZ nucleation is not due to thermal fluctuations. Instead, variations in the SRO of the MG dictate the observed STZ nucleation sites. This conclusion is in agreement with MD simulations of shock [91,93] and non-shock [219,249,254–256] deformation of Cu-Zr MGs.

Figure 6-3 shows a snapshot of η_i^{VM} for a 30-nm-thick chunk of the sample containing the shock wave front along with profiles of $\eta^{VM}(x)$ and $\tau(x)$. As can be seen clearly in the figure, the peak shear stress τ_{peak} coincides closely with the onset of STZ nucleation. The part of the shock front from the beginning of the shock wave rise to the peak shear stress constitutes the elastic precursor. The start of the elastic precursor is visible as a small dip in $\eta^{VM}(x)$, which is indicated by an arrow in the figure.

At $U_p = 0.875$ km/s, τ_{peak} is nearly twice that at $U_p = 0.375$ km/s. The high shear stress level results in an avalanche of STZ nucleation events at the plastic front, which is consistent with the sharp relaxation observed in the shear stress profile shown in Fig.

6-1. Approximately 15 nm from the start of the plastic front the shear stress has been reduced to half of its peak value. With increasing distance behind the plastic front, and thus time for evolution, the STZs grow larger and become more interconnected forming a dense network of plastic deformation. However, the deformation is not completely homogeneous and pockets of low η_i^{VM} (near the ambient value) are visible, which have largely resisted shear deformation.

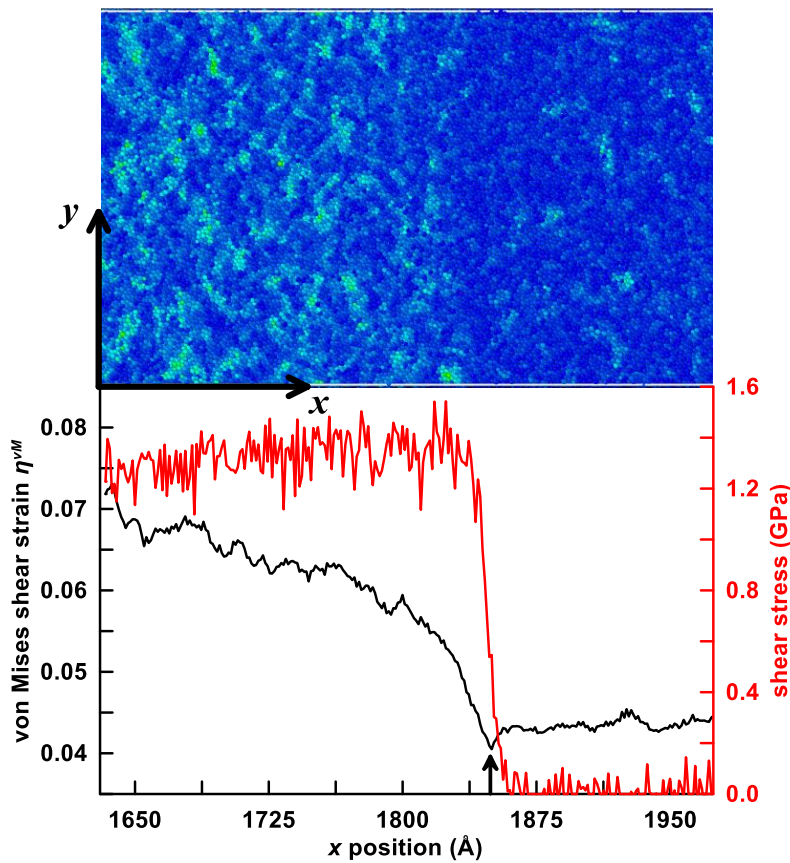


Figure 6-3. Snapshot at $t = 40$ ps of von Mises shear strain η_i^{VM} and profiles of $\eta^{\text{VM}}(x)$ and shear stress for $\text{Cu}_{50}\text{Zr}_{50}$ and $U_p = 0.375$ km/s.

The η_i^{VM} snapshot at $U_p = 1.75$ km/s shows that the shear strain distribution is now almost completely homogeneous behind the shock front. As was shown in Fig. 6-1, the shear stress drops rapidly from its peak value to zero within ~ 50 nm. The temperature immediately behind the shock front is ~ 1350 K and increases steadily to a

maximum of ~ 1550 K near the piston. As will be shown later, the MG has melted under the action of such a strong shock wave.

6.3.2 Composition Dependence and Melting

We now turn our focus to the composition dependence of the shock response. To aid in the analysis presented in the remainder of this chapter, we find it useful to differentiate between two states within the shock: state A at the position of the peak shear stress and state B in the quasi-steady flow far behind the start of the shock wave rise. The shear stress at states A and B are τ_{peak} and τ_{flow} , respectively. Figure 6-4(a) shows τ_{peak} as a function of the mean pressure $P_m = (P_{xx} + 2P_{yy})/3$ at the peak shear stress, while Fig. 6-4(b) shows τ_{flow} as a function of the final shock pressure.

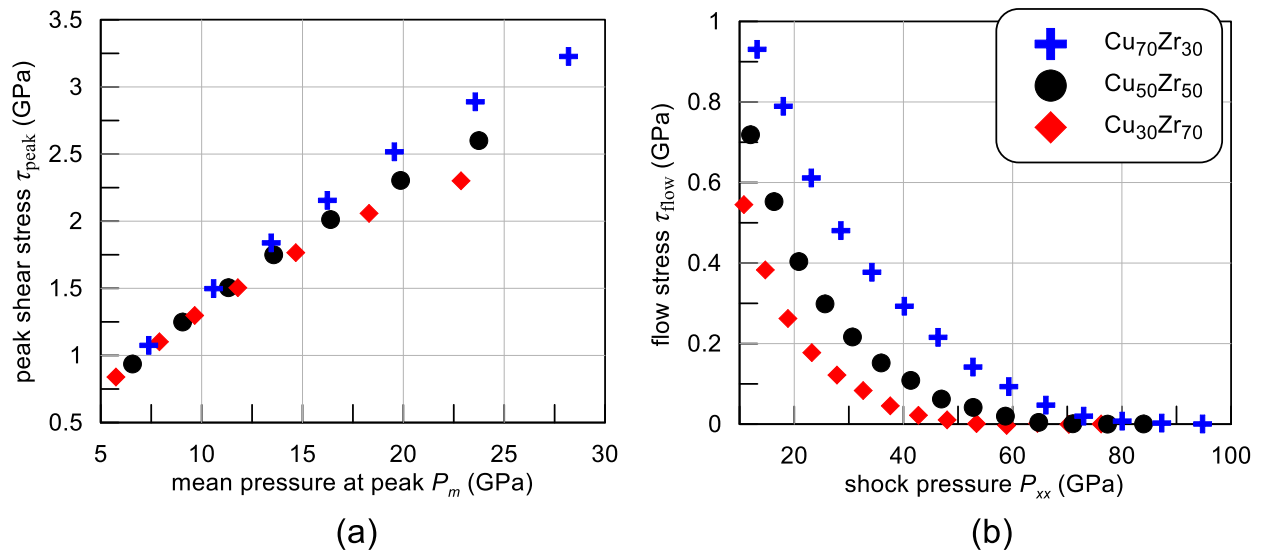


Figure 6-4. (a) Peak shear stress τ_{peak} as a function of the mean pressure P_m and (b) flow stress τ_{flow} as a function of the final shock pressure P_{xx} .

As was mentioned in Chapter 5, τ_{peak} corresponds to the critical shear stress required to plastically deform the pristine MG and is related to the yield strength $Y = 2\tau_{\text{peak}}$. Our simulations show that independent of composition τ_{peak} increases with

increasing P_m . Such behavior is consistent with the results presented in Chapter 5. Interestingly, when $P_m \leq 10$ GPa, τ_{peak} depends only on P_m and not on the composition of the MG. However, when $P_m > 10$ GPa, the curves start to diverge due to more pronounced thermal softening with decreasing Cu content.

After the initial STZ nucleation events at state A, the shear stress continues to relax as plasticity develops behind the plastic front. At state B, the shear stress has reached the quasi-steady value τ_{flow} , which corresponds to the shear strength of the rejuvenated, or plastically deformed, MG. In our simulations, τ_{flow} is calculated by averaging the shear stress in a 50-nm-thick slab near the piston face over several ps when the shock is close to the opposite edge of the sample. At a given shock pressure, τ_{flow} is greatest for $\text{Cu}_{70}\text{Zr}_{30}$ followed by $\text{Cu}_{50}\text{Zr}_{50}$ then $\text{Cu}_{30}\text{Zr}_{70}$. Therefore, MGs with higher Cu content exhibit greater resistance to plastic flow in the rejuvenated state. This is consistent with the results of Chapter 5 and the behavior of $\text{Cu}_x\text{Zr}_{100-x}$ MGs under pure shear loading found in previous MD simulations [219].

For all compositions, τ_{flow} decreases with increasing shock pressure indicating shear softening and thermal softening due to heating by the shock wave. At high enough shock pressures (50-80 GPa), the MG completely loses its ability to resist shear, i.e., $\tau_{flow} \rightarrow 0$. This transition occurs at ~ 53 GPa, ~ 65 GPa and ~ 80 GPa for $\text{Cu}_{30}\text{Zr}_{70}$, $\text{Cu}_{50}\text{Zr}_{50}$ and $\text{Cu}_{70}\text{Zr}_{30}$ MGs, respectively. The differences in these values compared to those given in Chapter 5 may be due to differences in preparation of the MG samples, including quench rate, inclusion of the annealing step and size of the initial amorphous sample prior to replication. However, the ordering observed among the different compositions remains the same.

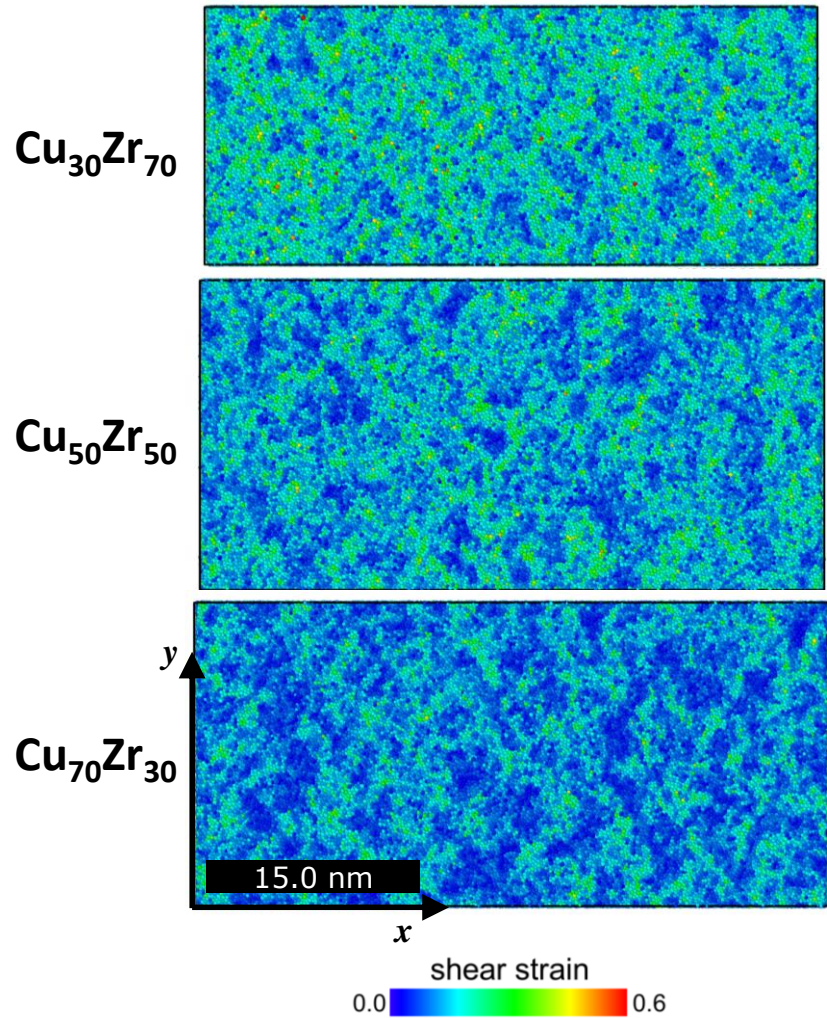


Figure 6-5. Snapshots of von Mises shear strain for $\text{Cu}_{30}\text{Zr}_{70}$, $\text{Cu}_{50}\text{Zr}_{50}$ and $\text{Cu}_{70}\text{Zr}_{30}$ metallic glasses at $P_{xx} = 20$ GPa.

Snapshots of η_i^{VM} at state B for $P_{xx} = 20$ GPa are shown in Fig. 6-5 for all three MG compositions. Visual inspection of the snapshots shows that the amount of shear deformation is highest for $\text{Cu}_{30}\text{Zr}_{70}$ followed by $\text{Cu}_{50}\text{Zr}_{50}$ then $\text{Cu}_{70}\text{Zr}_{30}$. Defining atoms having $\eta_i^{\text{VM}} > 0.2$ as participating in a shear transformation event [257], the fraction of atoms involved in STZs in $\text{Cu}_{30}\text{Zr}_{70}$, $\text{Cu}_{50}\text{Zr}_{50}$ and $\text{Cu}_{70}\text{Zr}_{30}$ are 29.3%, 17.5% and 8.6%, respectively. The average η_i^{VM} at state B is plotted in Fig. 6-6 as a function of shock pressure. Averages are taken over the same 50-nm-thick slab used in the calculation of

Fig. 6-4(b). At all shock pressures, the average η_i^{VM} is highest for $\text{Cu}_{30}\text{Zr}_{70}$ and decreases with increasing Cu content. This is consistent with the composition-dependent behavior of τ_{flow} observed in Fig. 6-4(b) and confirms that composition plays a large role in the yield behavior of the MG. Specifically, $\text{Cu}_x\text{Zr}_{100-x}$ MGs with higher Cu compositions (over the range of 30% to 70%) exhibit greater resistance to shear deformation and less plastic strain in the aftershock flow.

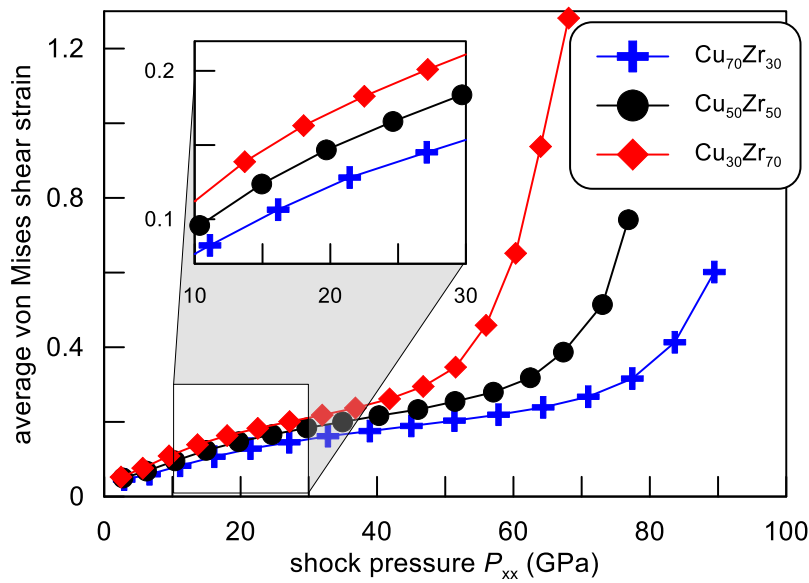


Figure 6-6. Average von Mises shear strain in the quasi-steady flow state B behind the shock front as a function of the final shock pressure P_{xx} .

The diffusivity D is calculated at state B to determine the melting transition under shock loading for each MG sample. For a given simulation, the 2D MSD for all atoms within a 50-nm-thick slab near the piston is calculated over an interval of 80 ps when the shock wave front is near the far side of the sample. A linear fit is applied to the $\text{MSD}(t)$ data and D is proportional to the slope of the fit. Figure 6-7 shows D as a function of the shock pressure P_{xx} for our simulated MGs together with results from previous MD Hugoniotat simulations for $\text{Cu}_{46}\text{Zr}_{54}$ MG obtained using the Mendeleev potential [91]. In

that work, the transition to shock melting occurs when $P_{xx} \approx 60$ GPa, which is evident by a rapid increase in D . Our results for $\text{Cu}_{50}\text{Zr}_{50}$ MG show a similar increase in D near ~ 60 GPa, thereby indicating a similar melting transition under shock loading for the Cheng and Mendeleev potentials.

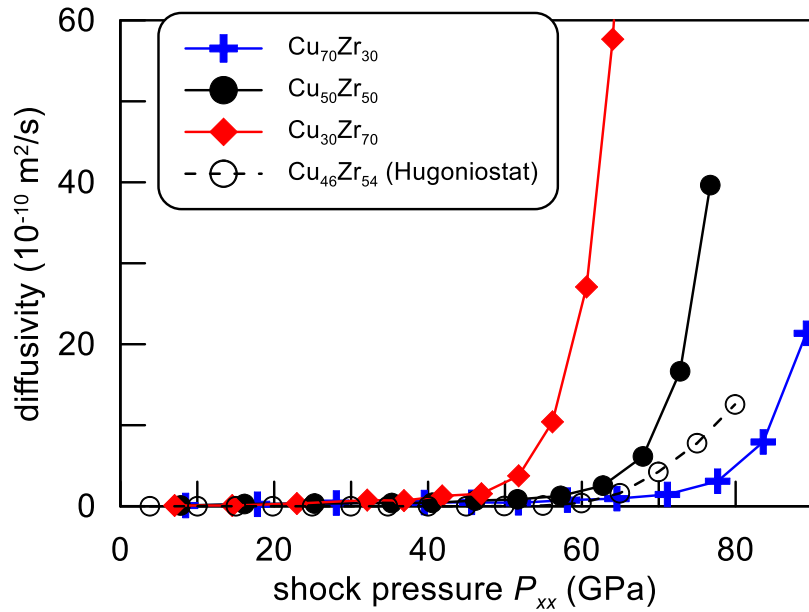


Figure 6-7. Diffusivity as a function of shock pressure P_{xx} for Cu-Zr metallic glasses from this work and $\text{Cu}_{46}\text{Zr}_{54}$ metallic glass from Hugoniostat simulations of Ref. [91].

Similar increases in the diffusivity data are observed for $\text{Cu}_{30}\text{Zr}_{70}$ and $\text{Cu}_{70}\text{Zr}_{30}$, but at different shock pressures. A sharp increase in D occurs near ~ 50 GPa for $\text{Cu}_{30}\text{Zr}_{70}$, whereas for $\text{Cu}_{70}\text{Zr}_{30}$ the increase in D is more gradual and starts near ~ 70 GPa. Clearly, the shock pressure required to induce melting increases as the Cu content of the MG increases over the range of 30% to 70%. The diffusivity analysis is consistent with the flow stress data plotted in Fig. 6-4(b).

6.3.3 Local Structural Changes During Shock Compression

Previous experiments [258] and MD simulations [217,219] have found that the local structures of Cu-Zr MGs are best understood from the perspective of Cu-centered clusters. Each cluster can be represented by a Voronoi polyhedron with indices $\langle n_3, n_4, n_5, n_6 \rangle$. Although faces with more than six vertices are observed in our samples, the fraction of polyhedra with more than six-sided faces is negligible and all observed polyhedra can be distinguished using indices up to n_6 . There are several hundred unique Cu-centered polyhedra types that make up the initial MG samples. However, the majority belong to a small number of polyhedra types. Specifically, we identified 24 types that represent ~70% of the total population for all three compositions.

Out of those 24 polyhedra types, nine were selected based on the criterion of greatest population change before and after shock loading. The polyhedra types (from 1 to 9), listed in order of increasing CN, are $\langle 0,2,8,0 \rangle$, $\langle 0,1,8,1 \rangle$, $\langle 0,3,6,1 \rangle$, $\langle 0,2,8,1 \rangle$, $\langle 0,1,8,2 \rangle$, $\langle 0,0,12,0 \rangle$, $\langle 0,2,8,2 \rangle$, $\langle 0,1,10,2 \rangle$ and $\langle 0,3,6,4 \rangle$. Together they make up ~40% of the overall polyhedra population of the initial MGs. Among these polyhedra are the so-called Z clusters, which have the minimum intrinsic disclination (rotational defect) density for a given CN and are presumably the most stable [245]. These are $\langle 0,2,8,0 \rangle$, $\langle 0,2,8,1 \rangle$, $\langle 0,0,12,0 \rangle$ and $\langle 0,1,10,2 \rangle$ for CN = 10, 11, 12 and 13, respectively. Clusters with Voronoi indices $\langle 0,0,12,0 \rangle$ have no intrinsic disclinations and have the maximum possible five-fold bonds for CN = 12. They are known as full icosahedra [259–261]. Representative Cu-centered clusters for each of the Z clusters are shown in Fig. 6-8 in order of increasing CN from left to right. Cu atoms are colored brown, while Zr atoms are colored green.

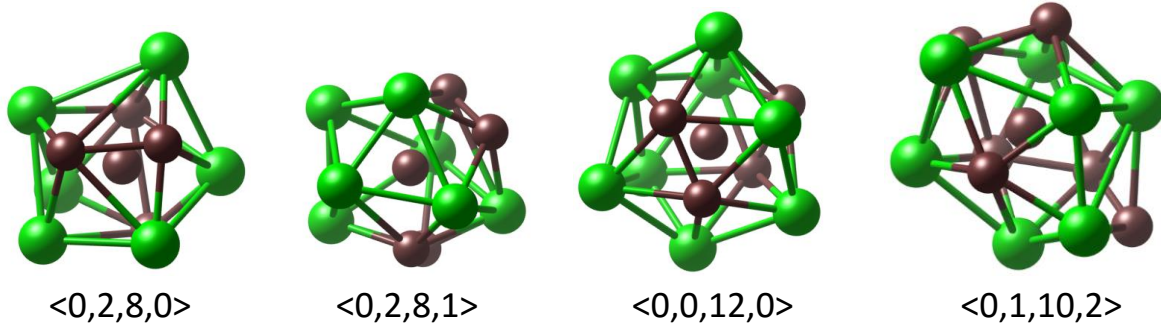


Figure 6-8. Representative Cu-centered clusters corresponding to the given set of Voronoi indices. Cu atoms are colored brown, while Zr atoms are colored green.

We tracked the populations of the four Z clusters in a 50-nm-thick slab near the piston as the shock wave passed through the sample. Every 10 ps the populations were calculated and compared to the values at the previous iteration. When $t \geq 100$ ps, the populations reached nearly steady values. Figure 6-9 shows the fractions of the different Cu-centered Z clusters at their quasi-steady values as a function of the piston velocity U_p for all three MGs. Independent of composition, the fraction of $\langle 0,2,8,0 \rangle$ polyhedra decreases with increasing U_p , while the fraction of $\langle 0,1,10,2 \rangle$ polyhedra increases up until $U_p \approx 1.8$ km/s. This is consistent with the higher compression ratios at higher shock intensities, which leads to an increase in the average CN of the polyhedra. The behavior is somewhat more complicated for $\langle 0,2,8,1 \rangle$ and $\langle 0,0,12,0 \rangle$ polyhedra. Both $\text{Cu}_{30}\text{Zr}_{70}$ and $\text{Cu}_{50}\text{Zr}_{50}$ exhibit large increases in $\langle 0,0,12,0 \rangle$ polyhedra with increasing U_p , while in $\text{Cu}_{70}\text{Zr}_{30}$ the fraction remains nearly steady. When $U_p \geq 1.5$ km/s, the fraction of $\langle 0,0,12,0 \rangle$ polyhedra decreases due to shock-induced melting.

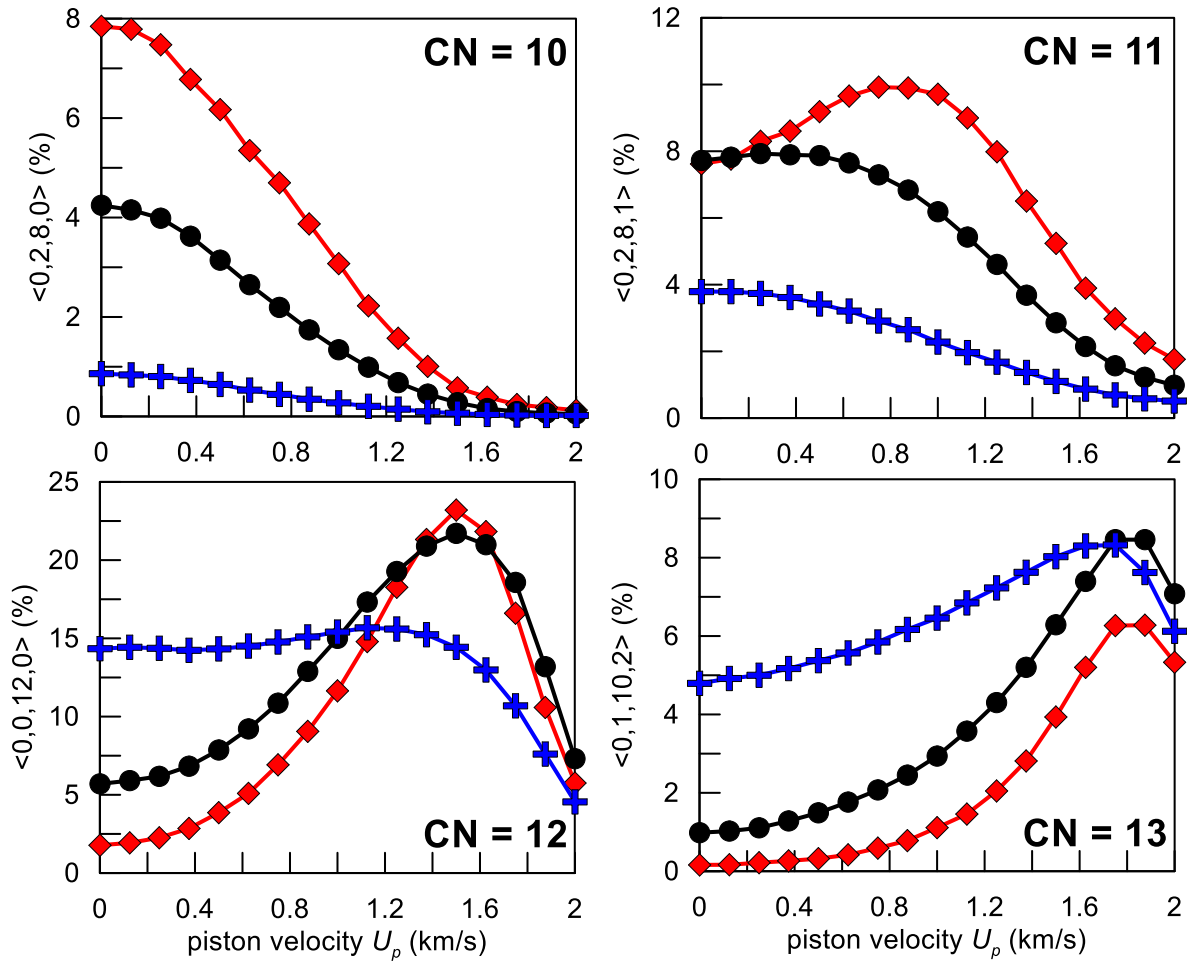


Figure 6-9. Fraction of Cu-centered Voronoi polyhedra at the quasi-steady flow state behind the shock front as a function of the piston velocity U_p . The polyhedron for each coordination number (CN) corresponds to the Z cluster, which has the minimum disclinations of any polyhedra type for that CN.

The data in Fig. 6-9 reflects total changes in polyhedra populations. However, it does not convey information related to transformations of polyhedra before and after shock loading. Such information would help assess the relative stability of different polyhedra types. To this end, we determined the distribution of polyhedra for a fixed group of atoms at two configurations: an initial configuration corresponding to a 50-nm-thick slab in the unshocked sample near the piston and a final configuration corresponding to the same slab at the quasi-steady flow state B behind the shock front.

Voronoi tessellation was performed on both the initial and final atomic configurations. The fraction of polyhedra transformed into different types was then calculated by comparing the initial and final Voronoi indices for each Cu atom. For example, the fraction of $\langle 0,0,12,0 \rangle$ polyhedra in the initial state for $\text{Cu}_{50}\text{Zr}_{50}$ MG is 5.7%. At $U_p = 0.75$ km/s, 1.4% are still the same type at the final state, state B. Therefore, $0.014/0.057 = 24\%$ of the original $\langle 0,0,12,0 \rangle$ polyhedra remain the same type, while $1 - 0.24 = 76\%$ have transformed into other types.

The fractions of transformed polyhedra as a function of the piston velocity U_p are plotted in Fig. 6-10 for the following nine polyhedra types: $\langle 0,2,8,0 \rangle$, $\langle 0,1,8,1 \rangle$, $\langle 0,3,6,1 \rangle$, $\langle 0,2,8,1 \rangle$, $\langle 0,1,8,2 \rangle$, $\langle 0,0,12,0 \rangle$, $\langle 0,2,8,2 \rangle$, $\langle 0,1,10,2 \rangle$ and $\langle 0,3,6,4 \rangle$.

These polyhedra types were selected based on the criteria of highest overall population fractions and greatest total population change during shock compression. Data for each MG composition is shown. The polyhedra types in the legend are listed in order of increasing CN from top to bottom. The transformed fraction can range from 100%, in which all the original polyhedra of that type have transformed into other types, to 0%, in which none have changed types. Note that the data in Fig. 6-10 only considers the initial and final atomic configurations, so multiple transformations may be occurring between these two end states.

For all three compositions, the $\langle 0,0,12,0 \rangle$ polyhedra, or full icosahedra, exhibit the lowest transformed fraction over almost the entire range of U_p . This indicates that the full icosahedra are the most resistant to change under shock loading. Such behavior is consistent with previous MD simulations of shock [93] and non-shock [219] loading of Cu-Zr MGs. The remaining eight polyhedra types, including the other three Z clusters,

exhibit less stability than the full icosahedra. Interestingly, when comparing the stability of the Z clusters: $\langle 0,2,8,0 \rangle$, $\langle 0,2,8,1 \rangle$, $\langle 0,0,12,0 \rangle$ and $\langle 0,1,10,2 \rangle$ with other clusters with the same CN, we find that the Z clusters are generally more stable.

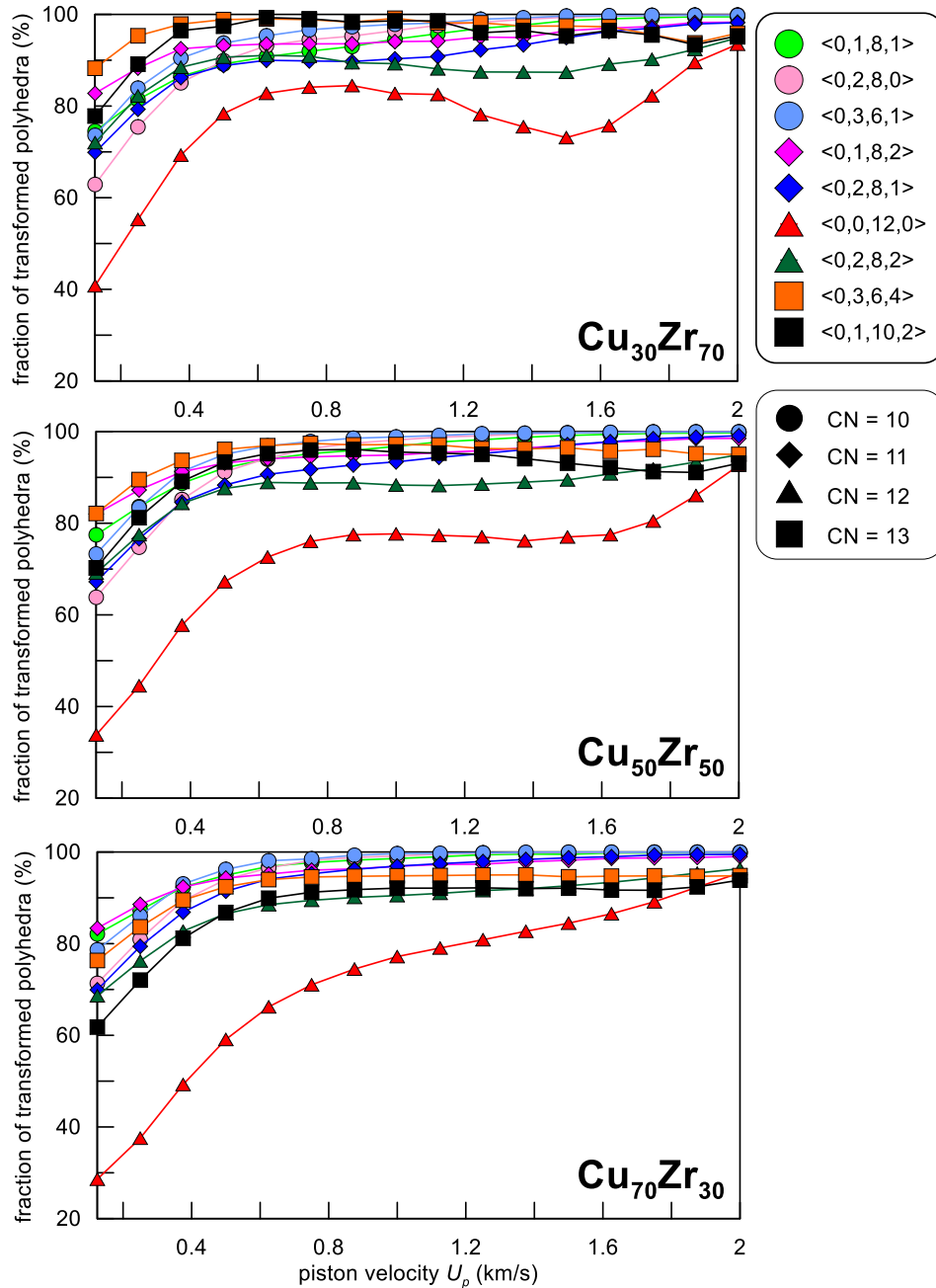


Figure 6-10. Fraction of Cu-centered Voronoi polyhedra that have been transformed into other types after transitioning from the unshocked state to the quasi-steady flow state B behind the shock front. A value of 100% indicates that all initial polyhedra of that type have transformed into other types at state B, while a value of 0% indicates that none have changed types.

With increasing U_p , the fractions of transformed polyhedra increase then reach nearly stable values when $U_p \approx 0.75$ km/s. This indicates that as shock intensity is increased more and more Cu-centered clusters become involved in the plastic deformation processes behind the shock front. Then, when $U_p \approx 0.75$ km/s, the fractions of transformed polyhedra saturate, corresponding to an exhaustion of clusters participating in the plastic response. Most polyhedra types shown in Fig. 6-10 exhibit such behavior, apart from $\langle 0,0,12,0 \rangle$ polyhedra for $\text{Cu}_{70}\text{Zr}_{30}$ MG, which continues to increase above $U_p \approx 0.75$ km/s. This change in the plastic response may explain why we observe a gradual change in slope in the plastic branches of the U_p - U_s Hugoniot curves between regions II and III that were shown in Chapter 5.

6.4 Summary

In this chapter, we studied the microstructural changes that occurred during shock compression of $\text{Cu}_x\text{Zr}_{100-x}$ MGs using MD simulations. The main plastic deformation mechanism found in our simulations was nucleation and growth of localized regions of higher-than-average shear strain, or simply STZs. At low shock intensities, the number of STZs nucleated behind the shock front is low and the plastic deformation is inhomogeneous. However, as the shock intensity is increased, more STZs are nucleated resulting in a more homogeneous plastic response. MGs with higher Cu content exhibit higher shear strengths and less shear strain in the quasi-steady flow behind the shock front, which is consistent with the increase in yield strength and decrease in plastic strain found in non-shock MD simulations [219] and quasistatic loading experiments [216]. The shock-induced melting transition is also found to occur at higher shock pressures as the Cu content of the MG is increased. Full icosahedra are

found to be the most stable under shock compression. The exhaustion of the number of Cu-centered clusters that are transformed under shock loading may contribute to the gradual change in slope observed in the plastic branch of the U_p - U_s relationship shown in Chapter 5.

CHAPTER 7 FERROELECTRICITY IN LANTHANUM BOROGERMANATE³

7.1 Background

LaBGeO₅ is a prototypical and well-studied material from the borosilicate stillwellite family of compounds, RB(Si,Ge)O₅ with R=(La,...,Er,Y). Particular technological interest in this material stems from its ferroelectric properties [98–102] and non-linear optical properties [108,262,263]. Moreover, LaBGeO₅ has good glass forming ability and it is possible to nucleate nano-crystallites within LaBGeO₅ glass [108]. Such a ferroelectric nanocomposite material is a transparent and optically-active medium and has interesting potential applications. The measured values for the spontaneous polarization are somewhat varied depending on the measurement method: pyroelectric measurements give a room-temperature polarization of 4.2 $\mu\text{C}/\text{cm}^2$ [100], whereas calorimetric measurements give a saturated polarization of 2.7 $\mu\text{C}/\text{cm}^2$ [99] and second-harmonic generation intensity measurements give a value of 12 $\mu\text{C}/\text{cm}^2$ [98].

At about 530°C, LaBGeO₅ undergoes a second-order transition to a high-symmetry paraelectric phase [98–101]. Valence Force Field examination of the phase transition [118] identified a possible phonon mode driving the ferroelectric phase transition. However, from an *ab initio* perspective, only examination of the low-temperature (LT) paraelectric phase has been performed [264]; neither the high-temperature (HT) phase nor the dynamics of the phase transition have been examined. Consideration of both phases is necessary to determine the ferroelectric properties of LaBGeO₅, specifically the spontaneous polarization. In this chapter, we present DFT

³The work described in this chapter has been published in B. J. Demaske, A. Chernatynskiy, and S. R. Phillpot, J. Phys: Condens. Matt. 28, 165901 (2016).

calculations on both the LT and HT phases of LaBGeO₅ as well as on the dynamics of the phase transition and the spontaneous polarization. We compare our results to available experimental data and previous theoretical models.

7.2 Simulation Methods

The energetics and ferroelectric properties LaBGeO₅ are determined from DFT calculations [126,265]. Specifically, we use the plane-wave DFT code VASP [131,159], which employs the PAW method to simplify treatment of core electrons [160,161]. In our calculations, 11 electrons for La ($5s^25p^65d^16s^2$), 3 for B ($2s^22p^1$), 14 for Ge ($3d^{10}4s^24p^2$) and 6 for O ($2s^22p^4$) are explicitly treated as valence, while the remaining core electrons are treated using the PAW pseudopotentials supplied by VASP. For comparison purposes, the Perdew-Zunger parameterization of the LDA [128], the PBE form of the GGA [129], and a revised PBE functional for solids PBEsol [130] are used to approximate the exchange-correlation functional. A plane-wave energy cutoff of 550 eV and a Γ -centered Monkhorst-Pack [266] $3\times 3\times 3$ k -point mesh are found to give energies converged to within 5 meV per atom.

Use of the LDA and GGA functionals results in an unphysical lowering of energy of the f orbitals of La such that they lie near the bottom of the conduction band. To correct for this behavior a Hubbard U correction is applied to these orbitals using the Dudarev formulation [188] present in VASP. As there are no published U parameters available for La in LaBGeO₅, we choose instead to use published values of $U = 11$ eV and $J = 0.68$ eV for the f orbitals of La in LaTiO₃ [267]. This choice is motivated by the similar La bonding environments in LaTiO₃ and LaBGeO₅.

Structures are relaxed until the maximum forces on each atom are less than 0.01 eV/Å and total stress on the unit cell is less than 0.01 eV/Ω, where Ω is the cell volume.

Second-order force constants are determined using the finite-displacement method implemented in the software package Phonopy [164] with VASP as the force calculator. Phonon dispersions are obtained by diagonalizing the dynamical matrix constructed from the second-order force constants. The MEP between the two symmetry-equivalent ferroelectric structures is calculated using the CI-NEB method [168,169,192] with a total of seven intermediate images. The macroscopic polarization of LaBGeO₅ is calculated using the modern theory of polarization based on the Berry phase formalism [119–123] as implemented in VASP.

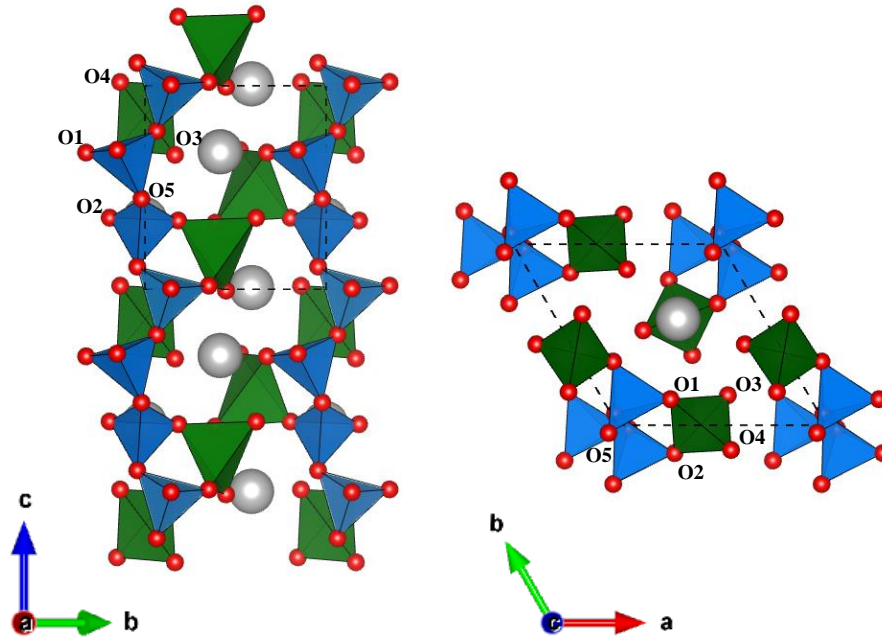


Figure 7-1. Structure of the low-temperature phase of LaBGeO₅ from the side (left panel) and from the top (right panel).

7.3 Simulation Results

7.3.1 Low-temperature Phase of LaBGeO₅

The LT phase of LaBGeO₅ belongs to the polar space group $P3_1$ and contains three formula units per cell (24 atoms). A schematic of the crystal structure of the LT

phase showing the locations of the five unique O atoms is shown in Fig. 7-1. Each of the B and Ge ions are surrounded by oxygen forming BO₄ (blue) and GeO₄ (green) tetrahedra. La atoms are shown in gray and O atoms in red with indices labeled. The BO₄ tetrahedra are linked together through corners to form chains along the c-axis, with each of the GeO₄ tetrahedra sharing corners with two BO₄ tetrahedra along a chain. The La ions are surrounded by oxygen forming large LaO₉ polyhedra that serve to interconnect the BO₄/GeO₄ chains. These LaO₉ polyhedra are composed of 14 triangular faces with the O atoms arranged at the nine vertices as shown in Fig. 7-2.

Table 7-1. Comparison of equilibrium lattice constants for the low-temperature phase of LaBGeO₅.

	Experiment (20°C)	VASP (LDA+ <i>U</i>)	VASP (PBEsol+ <i>U</i>)	ABINIT (norm-conserving)
<i>a</i> (Å)	7.0018	6.9986 (-0.05%)	7.0563 (+0.78%)	6.957 (-0.64%)
<i>c</i> (Å)	6.8606	6.8057 (-0.80%)	6.8578 (-0.04%)	6.742 (-1.73%)
<i>c/a</i>	0.9798	0.9724	0.9719	0.9691

Note: values in parentheses are percentage differences from experiment.

Theoretical and experimental lattice constants for the low-temperature phase of LaBGeO₅ are given in Table 7-1. Experimental values are taken from neutron powder data [116]. Theoretical results from another DFT study using norm-conserving pseudopotentials [264] are also given in addition to our DFT results. Percentage errors from experiment are given in parentheses. DFT results from our VASP calculations are given for the LDA and PBEsol functionals with the Hubbard *U* correction. Results from the PBE functional are omitted as they overestimate experimental lattice parameters; addition of the Hubbard *U* correction leads to an increase in the equilibrium volume,

worsening the agreement. The magnitudes of the total errors of the LDA+ U and PBEsol+ U lattice constants are almost equal. However, when considering the lattice constants from the high-temperature phase as well as atomic positions and interatomic distances, PBEsol+ U outperforms LDA+ U in terms of overall accuracy. Therefore, the results presented in the remainder of this work are calculated using PBEsol+ U functional unless stated otherwise.

The DFT-relaxed fractional coordinates of the atoms in the LT phase are given in Table 7-2 along with data from neutron powder experiments at 20°C [116] and another DFT work [264], where norm-conserving pseudopotentials were used in contrast to the PAW approach used here. Accounting for the differences in relaxed volumes, our atom positions differ from the neutron diffraction data by an average of $< 0.1 \text{ \AA}$ with the largest deviation of 0.08 \AA for the O5 atom. Furthermore, our atom positions and those obtained using norm-conserving pseudopotentials differ by on average $\sim 0.1 \text{ \AA}$ with the largest difference of 0.37 \AA for the B atom. Interatomic distances for the BO_4 and GeO_4 tetrahedra and LaO_9 polyhedra are given in Table 7-3.

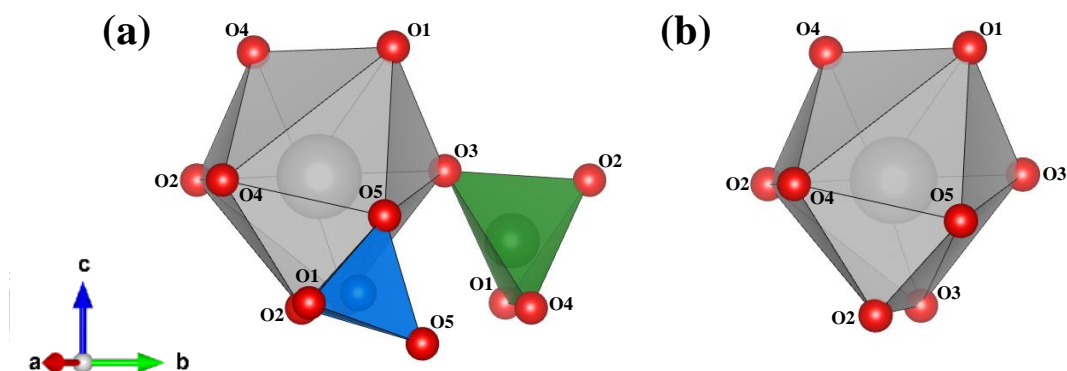


Figure 7-2. Structure of the LaO_9 polyhedra (a) with attached GeO_4 (green) and BO_4 (blue) tetrahedra and (b) without.

Table 7-2. Comparison of atom positions for the low-temperature phase of LaBGeO₅.

Atom	Position and multiplicity	Experiment (20°C)			This work (PBEsol+ <i>U</i>)			DFT (norm-conserving)		
		x/a	y/b	z/c	Δx	Δy	Δz	Δx	Δy	Δz
La	3a	0.4108	0.9990	1/3	0.0004	-0.0010	0.0052	0.0019	0.0001	0.0013
B	3a	0.8847	0.9878	0.3086	-0.0008	-0.0035	0.0015	-0.0460	-0.0021	-0.0017
Ge	3a	0.4181	0.0004	0.8433	0.0020	0.0068	-0.0041	0.0010	0.0063	-0.0071
O1	3a	0.1528	0.3428	0.0179	0.0024	0.0056	-0.0027	0.0017	0.0046	0.0000
O2	3a	0.3356	0.1481	0.9989	-0.0110	-0.0069	0.0016	-0.0081	-0.0067	-0.0065
O3	3a	0.1342	0.6089	0.3376	0.0031	0.0008	0.0085	0.0005	-0.0007	0.0009
O4	3a	0.6081	0.1620	0.6615	-0.0003	-0.0029	-0.0012	-0.0018	-0.0098	0.0051
O5	3a	0.0121	0.0543	0.7861	0.0070	0.0073	-0.0089	0.0032	0.0036	-0.0054

Note: theoretical values given as differences from experiment.

Table 7-3. Comparison of B-O, Ge-O and La-O interatomic distances (in Å) for the low-temperature phase of LaBGeO₅.

	Experiment (20°C)				This work (PBEsol+ <i>U</i>)				DFT (norm-conserving)			
La-O (Å)	O1:	2.651	O1':	2.772	O1:	-0.006	O1':	-0.049	O1:	0.068	O1':	-0.166
	O2:	2.684	O2':	2.678	O2:	0.033	O2':	0.071	O2:	0.008	O2':	0.021
	O3:	2.433	O3':	2.566	O3:	0.006	O3':	-0.017	O3:	-0.018	O3':	-0.036
	O4:	2.589	O4':	2.412	O4:	-0.037	O4':	0.032	O4:	-0.175	O4':	0.118
	O5:	2.672			O5:	-0.028			O5:	-0.078		
B-O (Å)	O1:	1.480	O5:	1.414	O1:	0.027	O5:	0.042	O1:	0.021	O5:	0.034
	O2:	1.535	O5':	1.481	O2:	-0.025	O5':	-0.021	O2:	-0.029	O5':	-0.035
Ge-O (Å)	O1:	1.782	O3:	1.625	O1:	0.008	O3:	0.099	O1:	-0.052	O3:	0.057
	O2:	1.772	O4:	1.761	O2:	0.019	O4:	-0.032	O2:	-0.032	O4:	-0.075

Note: theoretical values given as differences from experiment.

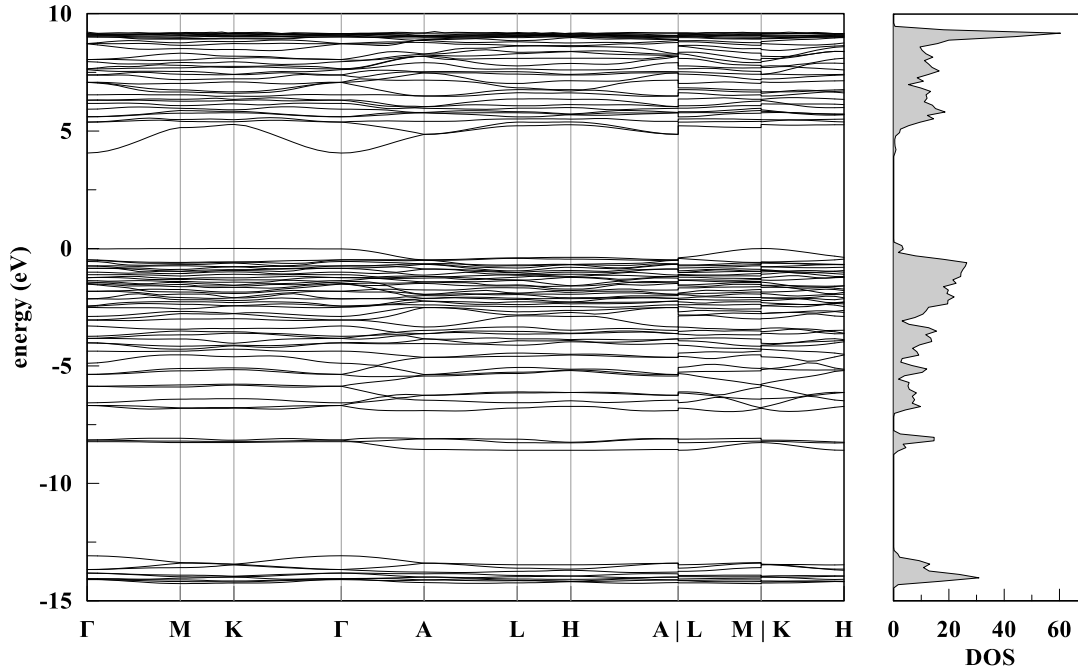


Figure 7-3. Electronic band structure and DOS for the low-temperature phase of LaBGeO₅ calculated using DFT.

The electronic band structure and DOS for the LT phase of LaBGeO₅ are shown in Fig. 7-3. In the figure, the zero energy is shifted to the top of the valence band. Our DFT calculations predict LaBGeO₅ to have an indirect band gap of 4.06 eV between the valence band maximum at K (1/3, 1/3, 0) and the conduction band minimum at Γ ; without the Hubbard U correction, the calculated band gap is 4.12 eV. This value is in good agreement with the value of 4.54 eV determined from a previous DFT study [264]. To the best of our knowledge, there are no experimental results for the band gap in LaBGeO₅. As was found in Ref. [264], the top of the valence band is almost flat along Γ -M-K- Γ . In our calculations, the energy decrease from K to Γ is only 0.018 eV. The concentrated group of bands near the upper edge of the conduction band belongs to the f orbitals of La. Without the Hubbard U correction, these bands are incorrectly predicted to lie near the bottom edge of the conduction band.

The phonon dispersion and DOS for the LT phase of LaBGeO₅ is shown in Fig. 7-4. Negative numbers correspond to imaginary frequencies. The absence of any imaginary phonon modes indicates that the structure is mechanically stable. This agrees with experiment as there is no evidence of any further phase transitions in LaBGeO₅ for temperatures below 20°C.

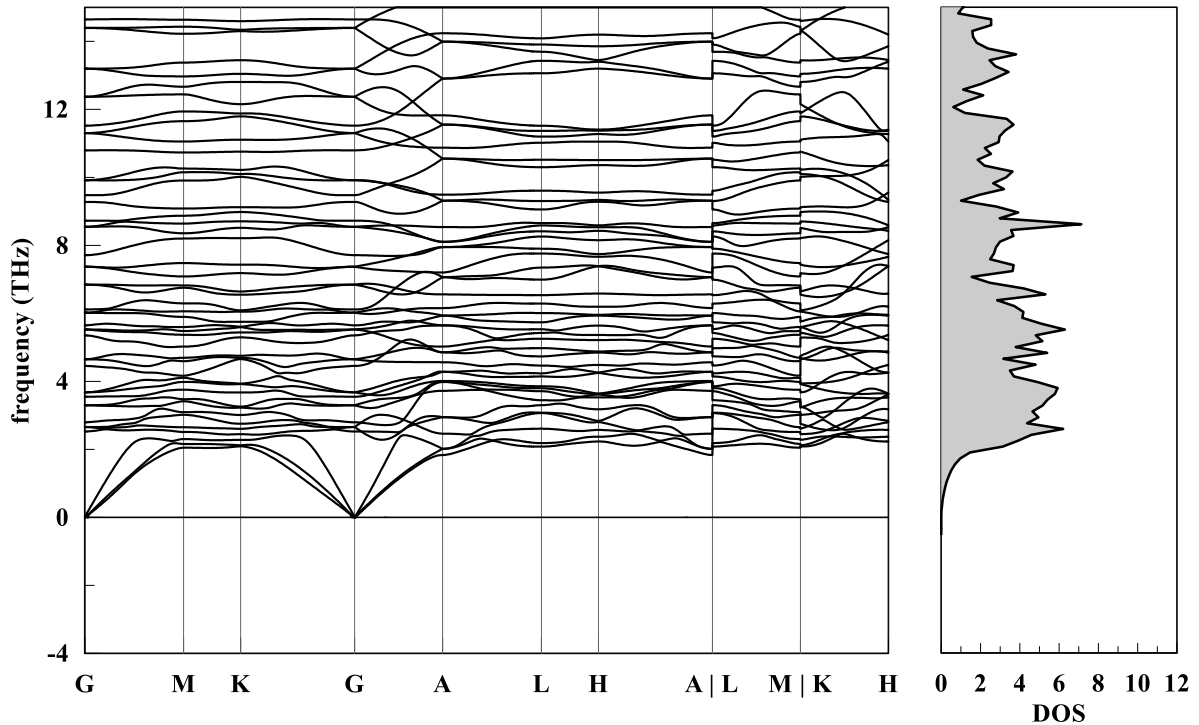


Figure 7-4. Phonon dispersion and DOS for the low-temperature phase of LaBGeO₅ calculated using DFT.

7.3.2 High-temperature Phase of LaBGeO₅

At 532°C, LaBGeO₅ undergoes a second-order phase transition from the polar space group $P3_1$ to the non-polar space group $P3_121$ [116,118]. According to the model in Ref. [116], both the La and Ge atoms undergo small displacements to bring them to lie on the twofold axis, while the four unique oxygen (O1, O2, O3 and O4) in the LT phase merge into only two unique oxygen (O1 and O3) in the HT phase. The B atom

and the remaining O5 atom lie near, but not on, the twofold axis. To maintain the stoichiometry of the cell, the generated sites on the B and O5 sublattices must be half-occupied. It is not clear whether the disorder is dynamic (a single atom oscillating between two sites or static) or static (with a random distribution of atoms filling half of the available sites) [116].

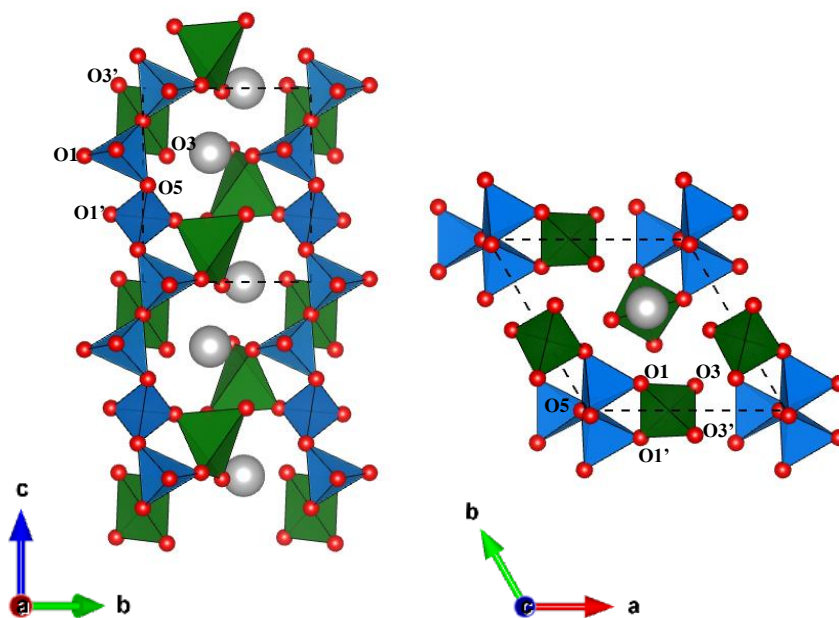


Figure 7-5. Structure of the high-temperature phase of LaBGeO₅.

In our calculations, the HT phase is constructed by placing atoms at the experimental positions given in Table 7-4 and generating a unit cell using the symmetry operators of the $P3_121$ space group. Results are given as differences from neutron powder data measurements performed at 535°C [116]. To account for the half occupancy of the B and O5 sites, we make the approximation that pairs of neighboring sites share a single atom which is placed at the mean position between the two sites. By doing so, the B and O5 atoms are forced to lie on the twofold axis to maintain the

$P3_121$ symmetry as well as the stoichiometry of the cell. A schematic of the crystal structure for the HT phase of LaBGeO_5 is shown in Fig. 7-5. In the figure, the B tetrahedra are shown in blue, Ge tetrahedra in green, La atoms in gray and O atoms in red with indices of all atoms labeled. The equilibrium lattice parameters from our DFT calculations using the PBEsol+ U functional are $a = 6.9939 \text{ \AA}$ and $c = 6.9508 \text{ \AA}$; LDA+ U gives $a = 6.9365 \text{ \AA}$ and $c = 6.8993 \text{ \AA}$. At 535°C the experimental lattice parameters are $a = 6.9926 \text{ \AA}$ and $c = 6.9315 \text{ \AA}$ [116].

Table 7-4. Comparison of atom positions for the high-temperature phase of LaBGeO_5 .

Atom	Position and multiplicity	Experiment (535°C)			This work (PBEsol+ U)		
		x/a	y/b	z/c	Δx	Δy	Δz
La	3(a)	0.4076	0	1/3	-0.0067	0.0000	0.0000
B	6(c)	0.8921	0.9988	0.3226	-0.0016	0.0012	0.0107
Ge	3(b)	0.4198	0	5/6	0.0005	0.0000	0.0000
O1	6(c)	0.1516	0.3418	0.0157	0.0045	0.0015	-0.0004
O3	6(c)	0.1444	0.6104	0.3392	-0.0034	-0.0014	0.0078
O5	6(c)	0.9955	0.0367	0.8031	-0.0246	-0.0366	0.0303

Note: theoretical results are given as differences from experiment.

The fractional atom positions for the relaxed structure are given in Table 7-4 along with data from neutron powder experiments at 535°C [116]. The average deviation in our atom positions from the neutron diffraction data is $< 0.1 \text{ \AA}$, with the largest deviation of 0.31 \AA for the O5 atom, which is expected as our approximation of the HT phase places the O5 atom between the two half-occupied sites observed in experiment. In the HT phase, both the B and Ge atoms retain fourfold coordination with the surrounding oxygen, whereas the coordination of the La polyhedra increases by

one, see Fig. 7-6. Interatomic distances for the BO_4 and GeO_4 tetrahedra and LaO_{10} polyhedra in the HT phase are given in Table 7-5. Calculated values are given as differences from neutron powder data measurements performed at 535°C [116]. Overall DFT gives good predictions for the oxygen bond distances in these polyhedra except for the La-O5 bond, which is overestimated by $\sim 0.2 \text{ \AA}$.

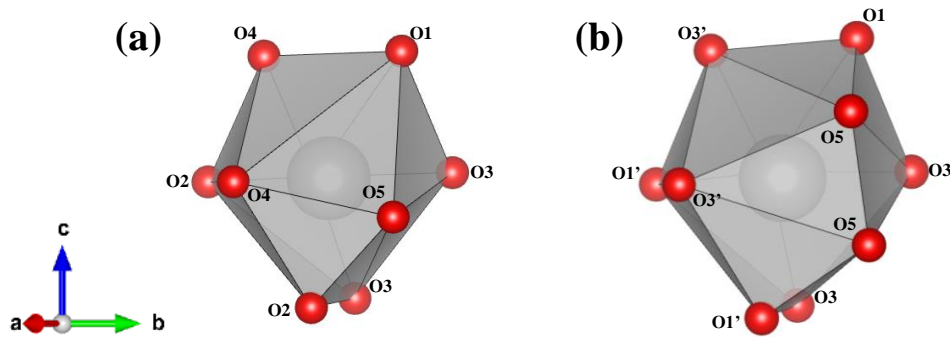


Figure 7-6. (a) Structure of the LaO_9 polyhedron from the low-temperature phase of LaBGeO_5 and (b) the LaO_{10} polyhedron from the high-temperature phase.

7.3.3 Lattice Dynamics of the Ferroelectric Phase Transition

Calculation of the phonon dispersion of the HT phase of LaBGeO_5 reveals an unstable mode, see the dashed curve in Fig 7-7. Note negative numbers correspond to imaginary phonon frequencies. Instabilities occur along the path Γ -M-K- Γ as well as near the L point. Displacing the atoms along the eigenvectors of the unstable mode at each of the high-symmetry points Γ , M, K and L leads to a set of double-well structures in the total energy as shown in Fig. 7-8. The double-well structure for the L-point modulation is omitted from the figure as the minima were much shallower than those obtained for the M-, K- and Γ -point modulations. Of these three double-well structures, the Γ -point eigendisplacements produce the deepest energy minima and the modulated

Table 7-5. Comparison of B-O, Ge-O and La-O interatomic distances (in Å) for the high-temperature phase of LaBGeO₅.

	Experiment (20°C)				This work (PBEsol+ <i>U</i>)			
La-O (Å)	O1 (x2):	2.680	O3' (x2):	2.598	O1 (x2):	0.002	O3' (x2):	-0.031
	O1' (x2):	2.771	O5 (x2):	2.747	O1' (x2):	-0.002	O5 (x2):	0.199
	O3 (x2):	2.408			O3 (x2):	0.004		
B-O (Å)	O1:	1.516	O5:	1.451	O1:	-0.014	O5:	0.007
	O1':	1.516	O5':	1.451	O1':	-0.014	O5':	0.007
Ge-O (Å)	O1 (x2):	1.760			O1 (x2):	0.022		
	O3 (x2):	1.697			O3 (x2):	0.031		

Note: theoretical distances are reported as differences from experiment.

structures have the same symmetry as observed in the LT phase. This confirms the LT phase observed in experiments is indeed the lowest energy structure of LaBGeO₅ that can be formed from breaking the symmetry of the HT phase.

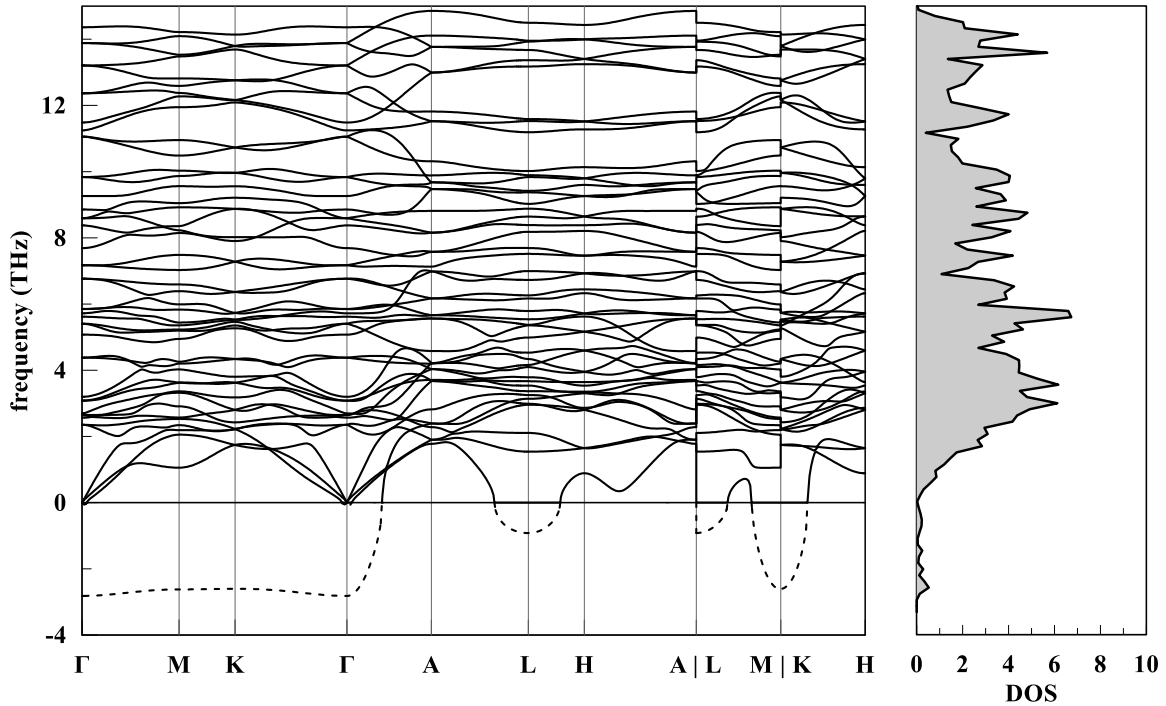


Figure 7-7. Phonon dispersion and DOS for the high-temperature phase of LaBGeO₅ calculated using DFT.

The main feature of the eigendisplacements of the unstable mode at the Γ point is a rigid rotation of the BO₄ tetrahedra about the O1-O1' (O1-O2) edges, which results in a z-displacement of 0.16 Å for the O5 atoms and a much smaller z-displacement of ~0.06 Å for the B atoms. The uncompensated z-displacements of these atoms leads to a change in the polarization of the cell along the *c*-axis. This is in agreement with previous calculations based on a Valence Force Field model [118] that identified this mode as the main driver for the ferroelectric phase transition in LaBGeO₅. In contrast, the unstable modes at the M, K and L points are antiferrodistortive, not producing any

change in polarization. In addition to the rigid BO_4 rotations, the Γ -point eigendisplacements feature a twisting of the GeO_4 tetrahedra within the xy -plane as well as small ~ 0.01 Å z -displacements of the La and Ge atoms in the direction opposite to that of the B and O5 atoms.

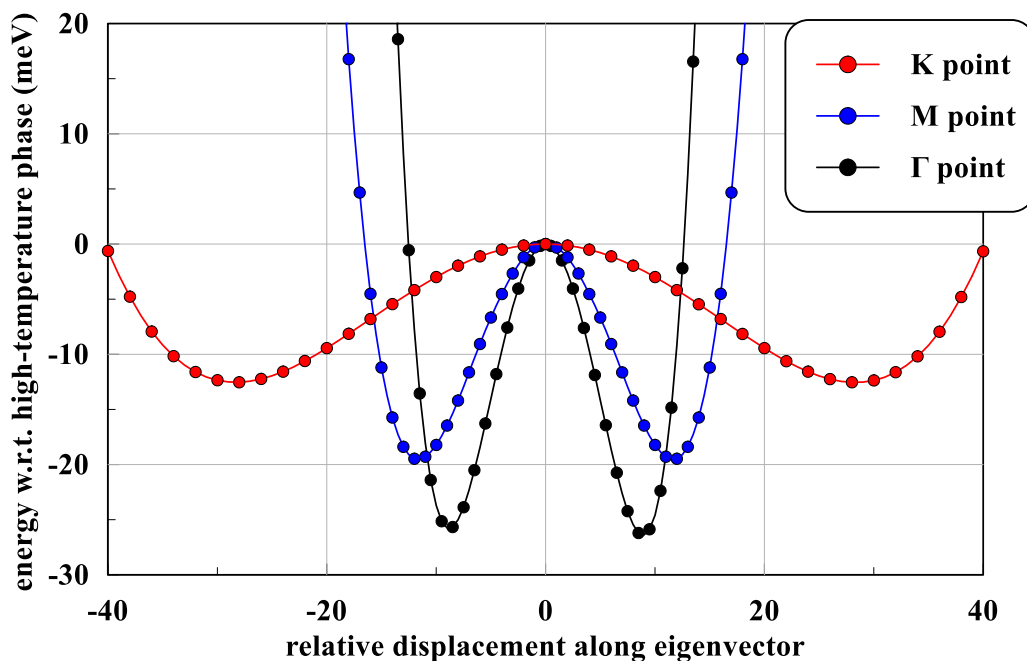


Figure 7-8. Energy as a function of the relative displacement of atoms from the high-temperature phase of LaBGeO_5 along the unstable phonon modes at the Γ , M and K points.

By performing full relaxation calculations on the structures obtained at the minima of the double well in Fig. 7-8, we obtain two symmetry-equivalent structures: $P3_1$ and $-(P3_1)$ belonging to the LT phase and spatially inverted in the c -direction. A CI-NEB calculation between the two structures gives the MEP as shown in Fig. 7-9(a). The saddle point along the MEP corresponds to a structure belonging to the high-symmetry space group $P3_121$, but with lattice parameters fixed to those of the LT phase. The height of the barrier is 0.62 eV. This is a much larger energy than that of the minima of

the double well shown in Fig. 7-8, which indicates more substantial atomic motions in the transformation between the $P3_1$ and $P3_121$ structures than predicted by the Γ -point modulation alone. Table 7-6 gives the atomic displacements along the MEP between the $P3_1$ and $P3_121$ structures and those from the Γ -point modulation from the structure at the left-hand minima of the double well to the unmodulated structure (HT phase of LaBGeO_5).

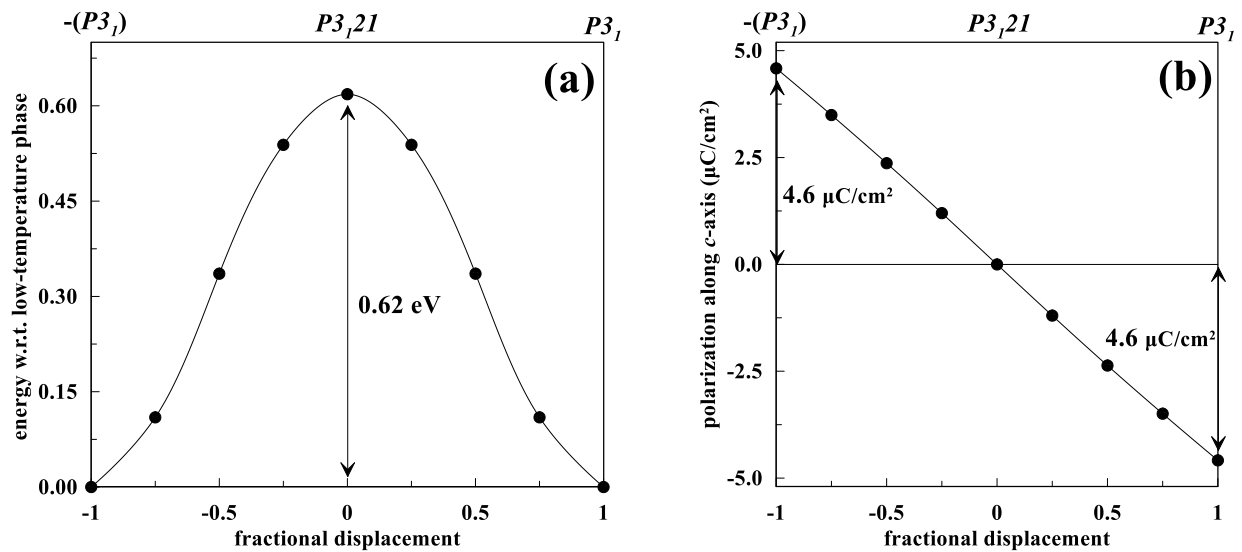


Figure 7-9. (a) MEP between the low-temperature (ferroelectric) and high-temperature (paraelectric) phases of LaBGeO_5 , and (b) magnitude of polarization along the c -axis for different points along the path shown in (a).

7.3.4 Spontaneous Polarization

According to the modern theory of polarization [119–123], the spontaneous polarization P_s is defined as the one-half the difference in polarization between two enantiomorphous polar structures along a continuous “switching” path from one structure to the other. The $P3_1$ and $-(P3_1)$ structures calculated in the previous section correspond to such a pair of enantiomorphous structures for the LT phase of LaBGeO_5 . The calculated MEP for the transformation from the $P3_1$ structure to $-(P3_1)$ structure is

shown in Fig. 7-9(a). The total polarization along the c -axis calculated along the transformation path is shown in Fig. 7-9(b). As only changes in polarization are measurable, values in Fig. 7-9(b) are given relative to the polarization at the transition state (paraelectric $P3_121$ structure). Changes to the polarization perpendicular to the c -axis are negligible. The spontaneous polarization P_s is therefore directed along the c -axis and is given by the difference in polarization between either of the two endpoint structures: $P3_1$ and $-(P3_1)$ and the transition state structure $P3_121$. For calculations using the PBEsol+ U functional, $P_s = 4.6 \mu\text{C}/\text{cm}^2$, whereas, without the Hubbard U correction, $P_s = 5.2 \mu\text{C}/\text{cm}^2$. Both calculated values lie within the experimental range of $2.7 - 12 \mu\text{C}/\text{cm}^2$ [98–100].

7.4 Discussion

The structural, electronic and vibrational properties for both the LT and HT phases of LaBGeO₅ have been calculated from first-principles. Phonon dispersion calculations on the relaxed HT phase revealed a zone-centered unstable mode with eigendisplacements corresponding almost exclusively to a rotation of BO₄ tetrahedra about the O1-O1' (O1-O2) edges, see the illustration of the rotation in Fig. 7-10. Valence Force Field model calculations [118] had previously identified this same mode, called a rigid unit mode or RUM, as exhibiting strong softening when the LT structure was changed towards the HT phase. Our CI-NEB calculations of the MEP between the two enantiomorphous LT structures showed that the complete phase transition dynamics feature a more pronounced BO₄ rotation as well as small displacements of the La and Ge atoms, see Table 7-6.

The difference in polarization between the initial and saddle points along the MEP in Fig. 7-9 is $4.6 \mu\text{C}/\text{cm}^2$, whereas when considering only the displacements due

to the Γ -point modulation the difference in polarization between the structures at the minimum and maximum of the double well in Fig. 7-8 is $1.9 \mu\text{C}/\text{cm}^2$. The large difference in these two values can be attributed to the more pronounced rotation of the BO_4 tetrahedra that occurs along the MEP between the LT and HT phases for which the z-displacements of the O5 and B atoms are more than double those of the Γ -point modulation alone.

Table 7-6. Atom displacements for the Γ -point modulation of the high-temperature phase and those between the initial and saddle points along the MEP.

Atom	Γ -point modulation			NEB MEP (initial \rightarrow saddle)		
	Δx (Å)	Δy (Å)	Δz (Å)	Δx (Å)	Δy (Å)	Δz (Å)
La	0.0000	0.0008	-0.0085	0.0780	0.0124	-0.0588
B	0.0001	0.0387	0.0576	-0.0878	-0.0400	0.1354
Ge	0.0001	-0.0142	-0.0132	-0.0271	-0.0447	-0.0639
O1	-0.0101	-0.0255	-0.0306	-0.0391	-0.1144	-0.1319
O2 (O1')	0.0101	-0.0255	-0.0307	-0.0248	-0.0312	-0.0234
O3	0.0366	-0.0099	-0.0028	0.1296	-0.0075	-0.0728
O4 (O3')	-0.0368	-0.0101	-0.0028	-0.0319	-0.0044	-0.0179
O5	-0.0003	-0.1703	0.1598	0.1224	-0.3760	0.3612

The spontaneous polarization estimated from the Valence Force Field model used in Ref. [118] is $13.8 \mu\text{C}/\text{cm}^2$, whereas our DFT calculations give a value less than half that. A likely source of this disagreement is an overestimation of the electronic contribution to the total macroscopic polarization, which is treated classically in the Valence Force Field model. However, according to the modern theory of polarization [119–121], the electronic polarization is a feature of the global phase of the Kohn-Sham

orbitals or, more generally, the phase of the many-body electronic wavefunction and is, therefore, strictly a quantum mechanical phenomenon.

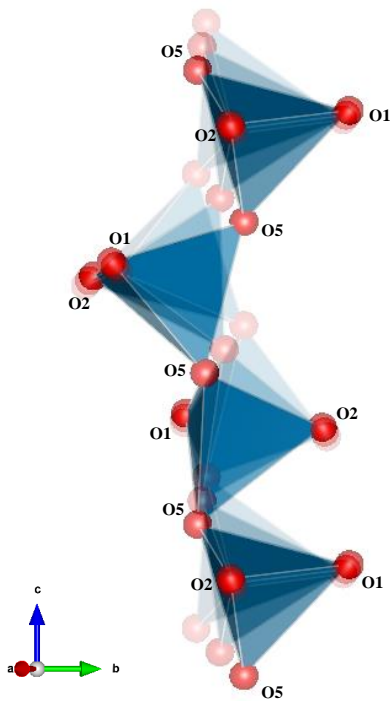


Figure 7-10. Illustration of the rigid rotation of the BO_4 tetrahedra occurring during the ferroelectric phase transition in LaBGeO_5 .

7.5 Summary

First-principles calculations on the LT and HT phases of crystalline LaBGeO_5 give fully relaxed structures in excellent agreement with atom positions determined via neutron diffraction experiments [116]. Phonon dispersion calculations coupled with CI-NEB calculations helped to elucidate the atomic displacements leading to the ferroelectric phase transition in LaBGeO_5 . The main feature of the phase transition is a rigid rotation of the BO_4 tetrahedra, which has also been recently confirmed by Valence Force Field model calculations [118]. Our DFT calculation of the spontaneous

polarization in LaBGeO₅ using the PBEsol+*U* functional is 4.6 μC/cm², which is in good agreement with the experimental range of 2.7 – 12 μC/cm² [98–100].

CHAPTER 8 CONCLUSIONS

In Chapter 3, the intrinsic defect and self-diffusion behavior in ordered phases of V_2C was investigated using DFT calculations. Calculated activation energies for vacancy-assisted vanadium self-diffusion and interstitial carbon self-diffusion showed good agreement with experimental values for self-diffusion of Nb in NbC_x [27] and C in V_6C_5 [24]. However, diffusion prefactors were underestimated in both cases. Interstitial carbon atoms were found to strongly influence vanadium migration barriers between basal planes. Migration paths closest to the carbon interstitials were found to exhibit the highest energy barriers, while those farthest away exhibited the smallest. Moreover, differences in carbon ordering among the three V_2C structures led to small differences in activation energies (~ 10 kJ/mol) for vanadium self-diffusion.

The work in Chapter 3 confirmed results of diffusion experiments in transition metal carbides, namely that carbon self-diffusion is several orders of magnitude faster than the metal atom self-diffusion. This can be attributed to the abundance of structural vacancies on the octahedral interstitial sublattice in V_2C , which facilitate carbon self-diffusion. Predicted self-diffusion coefficients, especially for carbon, are largely unaffected by the ordering of carbon atoms on the octahedral sublattice. Therefore, it seems reasonable to assume self-diffusion in disordered V_2C should exhibit similar activation energies and diffusion prefactors. Failure of DFT calculations to reproduce experimental diffusion prefactors for the case of vanadium self-diffusion may be due to a lack of anharmonicity or electronic entropy in the free energy calculations. Future work including at least quasi-harmonic and electronic entropy contributions to the free energy may help to determine if this is indeed the case. For carbon diffusion prefactors, the

underestimation is so severe that it is unlikely that more accurate calculations will improve the agreement much. Experiments on carbon self-diffusion in single-crystals of V_2C would help to confirm the diffusion prefactors measured in V_6C_5 [24] and $NbC_{0.868}$ [20]. If the results are confirmed, then other mechanisms for carbon self-diffusion must be proposed to reconcile the large disparity observed in the diffusion prefactors predicted by DFT calculations.

In Chapter, 4, the behavior of Fe, Ni, Ce, Nd and U impurities in V_2C was investigated using DFT calculations. It was found that all impurity types prefer the vanadium substitutional site over the much smaller octahedral site. The energy required to incorporate the impurity atom into V_2C was shown to increase with the size of the impurity. Specifically, the impurity volumes and defect energies follow the order $Fe < Ni < U < Nd < Ce$. Both Fe and Ni are smaller in size than the original vanadium atom, while Ce, Nd and U are larger. The large impurities, Ce, Nd and U, bind strongly to neighboring vanadium vacancies, whereas impurity-vacancy binding is much weaker for the small impurities, Fe and Ni. Because of their large size, Ce, Nd and U undergo significant displacements from the ideal substitutional site upon relaxation to form defect clusters with neighboring vanadium vacancies. This makes the prospect of a standard vacancy-assisted diffusion mechanism unlikely for these impurities. However, Fe and Ni remain close to the ideal substitutional site, which permitted calculation of migration barriers. Compared to migration barriers for vanadium self-diffusion, those of Ni were found to be lower on average, while those of Fe were higher.

The work done in Chapter 5 took the first steps to address the diffusion behavior of dilute metal impurities in V_2C . However, the formation of strongly bound defect

clusters for the case of Ce, Nd and U seems to point to a diffusion mechanism involving multiple vanadium or carbon vacancies. Future work is necessary to determine the correct lattice diffusion mechanism for such large impurities. In the case of the Fe and Ni, migration barriers were calculated for direct exchange of the impurity atom with a neighboring vanadium vacancy. However, calculation of the complete diffusion coefficients requires more work, and should start by considering the 8-frequency model of Ghate for diffusion of dilute impurities in an *hcp* lattice [268]. In addition to lattice diffusion, future studies should also consider other mechanisms including grain boundary diffusion and diffusion along dislocations, both of which may provide fast diffusion paths for impurities.

In Chapter 5, the behavior of Cu-Zr MGs under shock compression was investigated using MD simulations. An elastic-plastic response was found for all compositions with the shock wave consisting of a narrow elastic precursor and a sluggishly rising plastic wave. In contrast to crystalline metals, the HEL has a strong dependence on the final shock pressure, which indicates a pressure-dependent yield criterion for the simulated MGs. This agrees with shock experiments on multi-component MGs that also observed an increasing P_{HEL} with increasing shock intensity [57,60,200]. The calculated U_p - U_s Hugoniot (Fig. 5-7) can be broken into three regions: Region I ($U_p < 0.25$ km/s) nominally elastic shock wave, region II ($0.25 < U_p < 0.75$ km/s) split elastic and plastic shock waves and region III ($U_p > 0.75$ km/s) single elastic-plastic shock wave. The plastic branch of the U_p - U_s Hugoniot has approximately bilinear behavior with a gradual change in slope occurring near the transition from region II to III. The yield strength in the aftershock flow of the simulated $\text{Cu}_x\text{Zr}_{100-x}$ MGs was found to

increase with increasing Cu content over the experimental glass-forming range of 30% to 70%. Such behavior is consistent with previous MD simulations and quasistatic loading experiments.

One of the major predictions of a pressure-dependent HEL needs to be verified by additional shock compression experiments as most of the available experimental data is clustered around low impact velocities. It would be particularly helpful if such experiments could be performed with sub-ps time resolution of the rear surface motion, so that the narrow elastic precursor may be resolved with higher fidelity. In region II, both the elastic and plastic waves are unsteady as indicated by the slight, but continual attenuation of the elastic precursor as it propagates through the MG sample. Therefore, the shock velocities in this region are dependent on the length of the sample that was simulated. Further simulations on longer samples might determine whether shock waves generated in region II can reach a steady state, i.e., without further attenuation of the elastic precursor. It is known from MD simulations that the structure and mechanical properties of $\text{Cu}_x\text{Zr}_{100-x}$ MGs have a strong dependence on the cooling rate used to quench the melt [219,269–271] or, more generally, on the configurational potential energy of the resulting glassy structure [272]. In addition, quasistatic loading experiments have found that the mechanical properties of $\text{Cu}_x\text{Zr}_{100-x}$ MGs undergo significant changes when small amounts of Al or Ag are added [273–276]. It would be interesting to see how changes in configurational potential energy or small element additions affect the shock response of the resultant MGs. Such studies would be facilitated by the availability of interatomic potentials for both the Cu-Zr-Al [259] and Cu-Zr-Ag [277] systems that were both fit to amorphous structures.

In Chapter 6, the focus of the analysis was turned to the microstructural response of $\text{Cu}_x\text{Zr}_{100-x}$ MGs during shock compression. It was found that plastic deformation occurs via nucleation of localized regions of higher-than-average shear strain, termed shear transformation zones (STZs). With increasing shock intensity, the rate of STZ nucleation behind the shock front increased with a gradual progression towards homogeneous plastic flow. Moreover, the amount of shear strain at a given shock pressure was also shown to decrease with increasing Cu content, which is consistent with the increase in flow stress with Cu content observed in Chapter 5. The transition to shock-induced melting was also found to be dependent on the MG composition with higher Cu content leading to higher shock pressures for melting. Analysis of the local structure showed that regions of high icosahedral order ($\langle 0,0,12,0 \rangle$ Voronoi polyhedra) were most resistant to shear deformation. As $\text{Cu}_x\text{Zr}_{100-x}$ MGs with higher Cu compositions exhibit more icosahedral order, it is clear why we observe the similar trends in the composition dependence of the flow strength, shear strain and melting transition discussed above.

The shock pressure at the melting transition found in Chapter 6 was estimated using the diffusivity. From this analysis alone, it was not clear how the thermodynamic state of the material within the aftershock flow compared to the equilibrium liquid at the same pressure. By comparing the temperature and pressure of the material in the aftershock flow to the equilibrium melting line $T_m(P)$, one could determine whether the material is superheated, i.e., a solid above the equilibrium melting line, or supercooled, i.e., a liquid below the equilibrium melting line. As was shown in previous MD simulations of single-crystal Al, recrystallization can occur behind the shock front if the

melt is sufficiently undercooled [86]. Further work on shock-induced melting of $\text{Cu}_x\text{Zr}_{100-x}$ MGs should calculate the theoretical equilibrium melting line for different compositions. A way of differentiating solid amorphous structures from liquid ones also needs to be developed to complement the diffusivity analysis used in Chapter 6. One possible method is an in-plane RDF, which was used successfully in Ref. [86] to differentiate crystalline solid and liquid atomic configurations. It has been shown that MGs exhibit ordering that extends a few nanometers beyond the first nearest-neighbor shell [278–280]. In $\text{Cu}_x\text{Zr}_{100-x}$ MGs, this so-called medium-range order develops from connections among Cu-centered clusters, typically clusters of icosahedra [91,245,259,281,282]. MD simulations have found that these icosahedral networks form a kind of “elastic backbone” that starts to break down once the MG starts to yield [283–287]. Future work on shock loading of $\text{Cu}_x\text{Zr}_{100-x}$ MGs should focus on the evolution of connections among Cu-centered clusters as a function of shock intensity. One method to quantitatively assess the connectivity of different clusters is through the strength of the spatial correlation for different Voronoi polyhedra types [222,282].

In Chapter 7, the dynamics of the ferroelectric phase transition was investigated in the stillwellite compound LaBGeO_5 . From DFT calculations of the phonon dispersion for the high-temperature paraelectric phase, it was found that an unstable mode exists at the Γ point. Displacing the atoms along the eigenvectors of this mode led to two equivalent structures with oppositely-oriented polarization vectors that had the symmetry of the low-temperature ferroelectric phase. The main feature of the displacements is a rigid rotation of BO_4 tetrahedra, which is consistent with previous experimental and theoretical results [117,118]. The spontaneous polarization was

determined by calculating the change in the total polarization along a continuous path between the two enantiomorphous polar structures. The calculated value of $4.6 \mu\text{C}/\text{cm}^2$ lies within the experimental range of $2.7 - 12 \mu\text{C}/\text{cm}^2$ [98–100].

In this work, we used atomic-scale simulation methods to explore the thermodynamics and kinetics of defect formation and diffusion, phase transitions and high-strain-rate plastic deformation processes in ceramics and metals. Both static and dynamic simulation methods were used to explore different aspects of the PES. Energy- and force-based energy minimization methods were used to determine local energy minima to predict various defect structures and crystalline phases for V_2C and LaBGeO_5 . Constrained search methods, like the CI-NEB method, were used to determine MEPs and, hence, transition states for diffusive hops in V_2C . Force-constant matrix calculations of the transition states in V_2C and LaBGeO_5 were used to determine eigendisplacements and phonon frequencies. The process of glass formation in the Cu-Zr system was simulated using MD through rapid cooling of the melt to a quasi-stable local energy minimum corresponding to the amorphous state. Non-equilibrium MD simulations were performed to determine the system's trajectory within the energy landscape in response to high-strain-rate shock loading. Small clusters of atoms were shown to exhibit thermally-activated shear deformation events under sufficiently high stresses. Under action of a strong shock, the MG system was shown to undergo melting as it collectively escapes the local energy basin of the glassy state.

LIST OF REFERENCES

- [1] P. G. Debenedetti and F. H. Stillinger, *Nature* **410**, 259 (2001).
- [2] C. A. Schuh, T. C. Hufnagel, and U. Ramamurty, *Acta Mater.* **55**, 4067 (2007).
- [3] G. L. Hofman, A. G. Hins, D. L. Porter, L. Leibowitz, and E. L. Wood, *Int. Conf. Reliab. Fuels Liq. Met. React.* (1986).
- [4] L. A. Lawrence, *Nucl. Technol.* **64**, 139 (1984).
- [5] C. Gueneau, J. P. Piron, J. C. Dumas, V. Bouineau, F. C. Iglesias, and B. J. Lewis, *Fuel-Cladding Chemical Interaction* (Nuclear Energy Agency of the OECD (NEA), 2015).
- [6] D. C. Fee and C. E. Johnson, *J. Nucl. Mater.* **96**, 80 (1981).
- [7] R. J. M. Konings, T. R. Allen, R. E. Stoller, and S. Yamanaka, *Comprehensive Nuclear Materials* (Elsevier Science, Burlington, 2011).
- [8] D. D. Keiser and J. I. Cole, *TMS Lett.* **2**, 79 (2005).
- [9] D. D. Keiser and M. A. Dayananda, *J. Nucl. Mater.* **200**, 229 (1993).
- [10] R. G. Pahl, C. E. Lahm, and S. L. Hayes, *J. Nucl. Mater.* **204**, 141 (1993).
- [11] A. B. Cohen, H. Tsai, and L. A. Neimark, *J. Nucl. Mater.* **204**, 244 (1993).
- [12] H. J. Ryu, B. O. Lee, S. J. Oh, J. H. Kim, and C. B. Lee, *J. Nucl. Mater.* **392**, 206 (2009).
- [13] S. W. Yang, H. J. Ryu, J. H. Kim, B. O. Lee, and C. B. Lee, *J. Nucl. Mater.* **401**, 98 (2011).
- [14] D. D. Keiser and J. I. Cole, *An Evaluation of Potential Liner Materials for Eliminating FCCI in Irradiated Metallic Nuclear Fuel Elements* (Idaho National Laboratory (INL), 2007).
- [15] W. Y. Lo and Y. Yang, *J. Nucl. Mater.* **451**, 137 (2014).
- [16] S. Sarian, *J. Appl. Phys.* **39**, 3305 (1968).
- [17] F. J. J. Van Loo, W. Wakelkamp, G. F. Bastin, and R. Metselaar, *Solid State Ionics* **32**, 824 (1989).
- [18] S. Sarian and J. M. Criscione, *J. Appl. Phys.* **38**, 1794 (1967).
- [19] B. B. Yu and R. F. Davis, *Phys. Status Solidi* **51**, 261 (1979).

- [20] B. B. Yu and R. F. Davis, *J. Phys. Chem. Solids* **40**, 997 (1979).
- [21] A. V Shovensin, G. V Shcherbedinskii, and A. N. Minkevich, *Sov. Powder Metall. Met. Ceram.* **5**, 880 (1966).
- [22] S. Sarian, *J. Appl. Phys.* **39**, 5036 (1968).
- [23] W. Brizes, L. Cadoff, and J. Tobin, *J. Nucl. Mater.* **20**, 57 (1966).
- [24] S. Sarian, *J. Phys. Chem. Solids* **33**, 1637 (1972).
- [25] C. P. Buhsmer and P. H. Crayton, *J. Mater. Sci.* **6**, 981 (1971).
- [26] G. L. DePoorter and T. Wallace, *Adv. High Temp. Chem.* **4**, 107 (1970).
- [27] B. B. Yu and R. F. Davis, *J. Phys. Chem. Solids* **42**, 83 (1981).
- [28] S. Sarian, *J. Appl. Phys.* **40**, 3515 (1969).
- [29] M. Mantina, *Mater. Sci. Eng.* **PhD**, 252 (2008).
- [30] M. Mantina, Y. Wang, R. Arroyave, L. Q. Chen, Z. K. Liu, and C. Wolverton, *Phys. Rev. Lett.* **100**, 1 (2008).
- [31] M. Mantina, Y. Wang, R. Arroyave, S. L. Shang, L. Q. Chen, and Z. K. Liu, *J. Phys. Condens. Matter* **24**, 305402 (2012).
- [32] M. Mantina, Y. Wang, L. Q. Chen, Z. K. Liu, and C. Wolverton, *Acta Mater.* **57**, 4102 (2009).
- [33] M. Mantina, L. Q. Chen, and Z. K. Liu, *Defect Diffus. Forum* **294**, 1 (2009).
- [34] S. Huang, D. L. Worthington, M. Asta, V. Ozolins, G. Ghosh, and P. K. Liaw, *Acta Mater.* **58**, 1982 (2010).
- [35] N. Sandberg and R. Holmestad, *Phys. Rev. B - Condens. Matter Mater. Phys.* **73**, 1 (2006).
- [36] S. Ganeshan, L. G. Hector, and Z. K. Liu, *Acta Mater.* **59**, 3214 (2011).
- [37] S. Ganeshan, L. G. Hector, and Z. K. Liu, *Comput. Mater. Sci.* **50**, 301 (2010).
- [38] C. Z. Hargather, S. L. Shang, Z. K. Liu, and Y. Du, *Comput. Mater. Sci.* **86**, (2014).
- [39] M. Chen, *Annu. Rev. Mater. Res.* **38**, 445 (2008).
- [40] M. D. Demetriou, M. E. Launey, G. Garrett, J. P. Schramm, D. C. Hofmann, W. L. Johnson, and R. O. Ritchie, *Nat. Mater.* **10**, 123 (2011).

- [41] A. L. Greer, *Mater. Today* **12**, 14 (2009).
- [42] A. L. Greer and E. Ma, *MRS Bull.* **32**, 611 (2007).
- [43] W. L. Johnson, *JOM* **54**, 40 (2002).
- [44] J. F. Löffler, *Intermetallics* **11**, 529 (2003).
- [45] M. Miller and P. Liaw, *Bulk Metallic Glasses* (2008).
- [46] C. Suryanarayana and A. Inoue, *Bulk Metallic Glasses* (CRC Press, 2010).
- [47] M. M. Trexler and N. N. Thadhani, *Prog. Mater. Sci.* **55**, 759 (2010).
- [48] W. H. Wang, C. Dong, and C. H. Shek, *Mater. Sci. Eng. R Reports* **44**, 45 (2004).
- [49] A. R. Yavari, J. J. Lewandowski, and J. Eckert, *MRS Bull.* **32**, 635 (2007).
- [50] T. C. Hufnagel, C. A. Schuh, and M. L. Falk, *Acta Mater.* **109**, 375 (2016).
- [51] T. Mukai, T. G. Nieh, Y. Kawamura, A. Inoue, and K. Higashi, *Intermetallics* **10**, 1071 (2002).
- [52] T. C. Hufnagel, T. Jiao, Y. Li, L. Q. Xing, and K. T. Ramesh, *J. Mater. Res.* **17**, 1441 (2002).
- [53] R. F. Trunin, *Shock Compression of Condensed Materials* (Cambridge University Press, Cambridge, 1998).
- [54] L. Davison and R. A. Graham, *Phys. Rep.* **55**, 255 (1979).
- [55] L. C. Chhabildas, L. Davison, and Y. Horie, *High-Pressure Shock Compression of Solids VIII: The Science and Technology of High-Velocity Impact* (Springer Berlin Heidelberg, 2004).
- [56] S. J. Turneaure, J. M. Winey, and Y. M. Gupta, *Appl. Phys. Lett.* **84**, 1692 (2004).
- [57] S. J. Turneaure, J. M. Winey, and Y. M. Gupta, *J. Appl. Phys.* **100**, 63522 (2006).
- [58] T. Mashimo, H. Togo, Y. Zhang, Y. Uemura, T. Kinoshita, M. Kodama, and Y. Kawamura, *Appl. Phys. Lett.* **89**, 31 (2006).
- [59] H. Togo, Y. Zhang, Y. Kawamura, and T. Mashimo, *Mater. Sci. Eng. A* **448–451**, 264 (2007).
- [60] M. Martin, T. Sekine, T. Kobayashi, L. Kecskes, and N. N. Thadhani, *Metall. Mater. Trans. A Phys. Metall. Mater. Sci.* **38 A**, 2689 (2007).
- [61] F. Yuan, V. Prakash, and J. J. Lewandowski, *Mech. Mater.* **41**, 886 (2009).

- [62] S. A. Atroshenko, N. F. Morozov, W. Zheng, Y. J. Huang, Y. V. Sudenkov, N. S. Naumova, and J. Shen, *J. Alloys Compd.* **505**, 501 (2010).
- [63] F. Xi, Y. Yu, C. Dai, Y. Zhang, and L. Cai, *J. Appl. Phys.* **108**, 1 (2010).
- [64] T. Jaglinski, S. J. Turneaure, and Y. M. Gupta, *J. Appl. Phys.* **112**, 1 (2012).
- [65] B. Luo, G. Wang, F. Tan, J. Zhao, C. Liu, and C. Sun, *AIP Adv.* **5**, (2015).
- [66] Y. Y. Yu, F. Xi, C. Da Dai, L. C. Cai, Y. Tan, X. M. Li, Q. Wu, and H. Tan, *Chinese Phys. B* **24**, 66201 (2015).
- [67] Y. Hironaka, A. Yazaki, F. Saito, K. G. Nakamura, K. Kondo, H. Takenaka, and M. Yoshida, *Appl. Phys. Lett.* **77**, 1967 (2000).
- [68] S. N. Luo, D. C. Swift, T. E. Tierney, D. L. Paisley, G. A. Kyrala, R. P. Johnson, A. A. Hauer, O. Tschauner, and P. D. Asimow, *High Press. Res.* **24**, 409 (2004).
- [69] K. Rosolankova, J. S. Wark, E. M. Bringa, and J. Hawreliak, *J. Phys. Condens. Matter* **18**, 6749 (2006).
- [70] M. Righini, R. Quidant, S. R. Emory, J. A. Dionne, H. A. Atwater, Y. Kadoya, H. F. Hofmann, Q. Wang, F. Capasso, V. M. Shalaev, A. Polman, A. Archambault, T. V Teperik, F. Marquier, J. J. Greffet, P. Yeh, D. Milathianaki, S. Boutet, G. J. Williams, A. Higginbotham, D. Ratner, A. E. Gleason, M. Messerschmidt, M. M. Seibert, D. C. Swift, P. Hering, J. Robinson, W. E. White, and J. S. Wark, *Science* (80-.). **342**, 220 (2013).
- [71] M. G. Gorman, R. Briggs, E. E. McBride, A. Higginbotham, B. Arnold, J. H. Eggert, D. E. Fratanduono, E. Galtier, A. E. Lazicki, H. J. Lee, H. P. Liermann, B. Nagler, A. Rothkirch, R. F. Smith, D. C. Swift, G. W. Collins, J. S. Wark, and M. I. McMahon, *Phys. Rev. Lett.* **115**, 1 (2015).
- [72] G. Mogni, A. Higginbotham, K. Gaál-Nagy, N. Park, and J. S. Wark, *Phys. Rev. B* **89**, 64104 (2014).
- [73] T. R. Mattsson, J. M. D. Lane, K. R. Cochrane, M. P. Desjarlais, A. P. Thompson, F. Pierce, and G. S. Grest, *Phys. Rev. B* **81**, 54103 (2010).
- [74] J. Budzien, A. P. Thompson, and S. V. Zybin, *J. Phys. Chem. B* **113**, 13142 (2009).
- [75] H. N. Jarmakani, E. M. Bringa, P. Erhart, B. A. Remington, Y. M. Wang, N. Q. Vo, and M. A. Meyers, *Acta Mater.* **56**, 5584 (2008).
- [76] M. J. Cawkwell, T. D. Sewell, L. Zheng, and D. L. Thompson, *Phys. Rev. B - Condens. Matter Mater. Phys.* **78**, 1 (2008).

- [77] S. Zhao, T. C. Germann, and A. Strachan, Phys. Rev. B - Condens. Matter Mater. Phys. **76**, 1 (2007).
- [78] T. Germann, B. Holian, P. Lomdahl, and R. Ravelo, Phys. Rev. Lett. **84**, 5351 (2000).
- [79] V. Zhakhovskii, S. Zybin, K. Nishihara, and S. Anisimov, Phys. Rev. Lett. **83**, 1175 (1999).
- [80] D. H. Robertson, D. W. Brenner, and C. T. White, Phys. Rev. Lett. **67**, 3132 (1991).
- [81] E. M. Bringa, A. Caro, Y. Wang, M. Victoria, J. M. McNaney, B. A. Remington, R. F. Smith, B. R. Torralva, and H. Van Swygenhoven, Science **309**, 1838 (2005).
- [82] K. Kadau, T. C. Germann, P. S. Lomdahl, and B. L. Holian, Phys. Rev. B - Condens. Matter Mater. Phys. **72**, 1 (2005).
- [83] E. M. Bringa, K. Rosolankova, R. E. Rudd, B. A. Remington, J. S. Wark, M. Duchaineau, D. H. Kalantar, J. Hawreliak, and J. Belak, Nat. Mater. **5**, 805 (2006).
- [84] H. N. Jarmakani, E. M. Bringa, P. Erhart, B. A. Remington, Y. M. Wang, N. Q. Vo, and M. A. Meyers, Acta Mater. **56**, 5584 (2008).
- [85] V. V. Zhakhovsky, M. M. Budzevich, N. A. Inogamov, I. I. Oleynik, and C. T. White, Phys. Rev. Lett. **107**, 1 (2011).
- [86] M. M. Budzevich, V. V. Zhakhovsky, C. T. White, and I. I. Oleynik, Phys. Rev. Lett. **109**, (2012).
- [87] W. Ma, W. Zhu, and Y. Hou, J. Appl. Phys. **114**, (2013).
- [88] R. Ravelo, T. C. Germann, O. Guerrero, Q. An, and B. L. Holian, Phys. Rev. B - Condens. Matter Mater. Phys. **88**, (2013).
- [89] D. Tramontina, P. Erhart, T. Germann, J. Hawreliak, A. Higginbotham, N. Park, R. Ravelo, A. Stukowski, M. Suggit, Y. Tang, J. Wark, and E. Bringa, High Energy Density Phys. (2014).
- [90] K. Chen, Y. Yu, Z. Zhang, and S. Q. Shi, Scr. Mater. **120**, 62 (2016).
- [91] W. R. Jian, X. H. Yao, L. Wang, X. C. Tang, and S. N. Luo, J. Appl. Phys. **118**, 15901 (2015).
- [92] P. Wen, G. Tao, C. Pang, S. Yuan, and Q. Wang, Comput. Mater. Sci. **124**, 304 (2016).
- [93] B. Arman, S. N. Luo, T. C. Germann, and T. Çağın, Phys. Rev. B - Condens. Matter Mater. Phys. **81**, 1 (2010).

- [94] E. M. Bringa, *Science* (80-.). **309**, 1838 (2005).
- [95] V. N. Sigaev, E. V. Lopatina, P. D. Sarkisov, S. Y. Stefanovich, and V. I. Molev, *Mater. Sci. Eng. B* **48**, 254 (1997).
- [96] V. N. Sigaev, S. Y. Stefanovich, P. D. Sarkisov, and E. V Lopatina, *Glas. Phys. Chem.* **20**, 392 (1994).
- [97] V. N. Sigaev, S. Y. Stefanovich, P. D. Sarkisov, and E. V. Lopatina, *Mater. Sci. Eng. B* **32**, 17 (1995).
- [98] S. Y. Stefanovich, B. V Mill, and A. V Butashin, *Kristallografiya* **37**, 965 (1992).
- [99] A. Onodera, B. A. Strukov, and A. Belov, *J. Phys. Soc. Japan* **62**, 4311 (1993).
- [100] E. V. Milov and B. A. Strukov, *Phys. Solid State* **43**, 513 (2001).
- [101] E. V. Milov, B. A. Strukov, and V. N. Milov, *Ferroelectrics* **269**, 15 (2002).
- [102] B. A. Strukov, E. V. Milov, V. N. Milov, A. P. Korobtsov, T. Tomida, K. Sato, M. Fukunaga, and Y. Uesu, *Ferroelectrics* **314**, 105 (2005).
- [103] J. Capmany, D. Jaque, J. García Solé, and A. A. Kaminskii, *Appl. Phys. Lett.* **72**, 531 (1998).
- [104] J. Capmany and J. García Solé, *Appl. Phys. Lett.* **70**, 2517 (1997).
- [105] Y. Takahashi, Y. Benino, V. Dimitrov, and T. Komatsu, *J. Non. Cryst. Solids* **260**, 155 (1999).
- [106] Y. Takahashi, Y. Benino, T. Fujiwara, and T. Komatsu, *J. Appl. Phys.* **89**, 5282 (2001).
- [107] V. N. Sigaev, P. D. Sarkisov, P. Pernice, A. Aronne, A. M. Datsenko, S. Y. Stefanovich, V. I. Fertikov, O. A. Pozhogin, and D. A. Zakharkin, *J. Eur. Ceram. Soc.* **24**, 1063 (2004).
- [108] P. Gupta, H. Jain, D. B. Williams, O. Kanert, and R. Kuechler, *J. Non. Cryst. Solids* **349**, 291 (2004).
- [109] V. N. Sigaev, S. V. Lotarev, E. V. Orlova, S. Y. Stefanovich, P. Pernice, A. Aronne, E. Fanelli, and I. Gregora, *J. Non. Cryst. Solids* **353**, 1956 (2007).
- [110] V. N. Sigaev, E. A. Alieva, S. V. Lotarev, N. M. Lepekhn, Y. S. Priseko, and A. V. Rasstanaev, *Glas. Phys. Chem.* **35**, 13 (2009).
- [111] A. Stone, M. Sakakura, Y. Shimotsuma, G. Stone, P. Gupta, K. Miura, K. Hirao, V. Dierolf, and H. Jain, *Opt. Express* **17**, 23284 (2009).

- [112] T. O. Lipat'eva, S. V. Lotarev, A. S. Lipat'ev, P. G. Kazansky, and V. N. Sigaev, in *Proc. SPIE* (2015), p. 945018.
- [113] A. Stone, H. Jain, V. Dierolf, M. Sakakura, Y. Shimotsuma, K. Miura, K. Hirao, J. Lapointe, and R. Kashyap, *Sci. Rep.* **5**, 10391 (2015).
- [114] A. S. Lipat'ev, T. O. Lipat'eva, S. V. Lotarev, S. S. Fedotov, E. V. Lopatina, and V. N. Sigaev, *Glas. Ceram. (English Transl. Steklo I Keramika)* **73**, 441 (2017).
- [115] A. S. Lipat'ev, T. O. Lipat'eva, S. V. Lotarev, A. G. Okhrimchuk, A. S. Larkin, M. Y. Presnyakov, and V. N. Sigaev, *Cryst. Growth Des.* **17**, 4670 (2017).
- [116] E. L. Belokoneva, W. I. F. David, J. B. Forsyth, and K. S. Knight, *J. Physics. Condens. Matter* **9**, 3503 (1997).
- [117] S. Kamba, J. Petzelt, I. Gregora, and Z. Zikmund, *Phys. Stat. Sol.* **214**, (1999).
- [118] M. B. Smirnov, A. V. Menschikova, I. Kratochvilova-Hruba, and Z. Zikmund, *Phys. Status Solidi* **241**, 1017 (2004).
- [119] R. D. King-Smith and D. Vanderbilt, *Phys. Rev. B* **47**, 1651 (1993).
- [120] D. Vanderbilt and R. D. King-Smith, *Phys. Rev. B* **48**, 4442 (1993).
- [121] R. Resta, *Rev. Mod. Phys.* **66**, 899 (1994).
- [122] R. Resta, *Model. Simul. Mater. Sci. Eng.* **11**, R69 (2003).
- [123] R. Resta and D. Vanderbilt, *Top. Appl. Phys.* **105**, 31 (2007).
- [124] G. H. Vineyard, *J. Phys. Chem. Sol.* **3**, 121 (1957).
- [125] M. Mantina, *A First-Principles Methodology for Diffusion Coefficients in Metals and Dilute Alloys* (ProQuest, 2008).
- [126] P. Hohenberg and W. Kohn, *Phys. Rev.* **136**, B864 (1964).
- [127] W. Kohn and L. J. Sham, *Phys. Rev.* **140**, A1133 (1965).
- [128] J. P. Perdew and A. Zunger, *Phys. Rev. B* **23**, 5048 (1981).
- [129] J. P. Perdew, K. Burke, and M. Ernzerhof, *Phys. Rev. Lett.* **77**, 3865 (1996).
- [130] J. P. Perdew, A. Ruzsinszky, G. I. Csonka, O. A. Vydrov, G. E. Scuseria, L. A. Constantin, X. Zhou, and K. Burke, *Phys. Rev. Lett.* **100**, 136406 (2008).
- [131] G. Kresse and J. Furthmüller, *Phys. Rev. B* **54**, 11169 (1996).
- [132] N. A. Spaldin, *J. Solid State Chem.* **195**, 2 (2012).

- [133] L. Verlet, Phys. Rev. **159**, 98 (1967).
- [134] W. C. Swope, H. C. Andersen, P. H. Berens, and K. R. Wilson, J. Chem. Phys. **76**, 637 (1982).
- [135] C. W. Gear, *Numerical Initial Value Problems in Ordinary Differential Equations* (Prentice-Hall, 1971).
- [136] S. Nosé, J. Chem. Phys. **81**, 511 (1984).
- [137] S. Nosé, Mol. Phys. **52**, 255 (1984).
- [138] W. G. Hoover, Phys. Rev. A **31**, 1695 (1985).
- [139] M. Parrinello and A. Rahman, J. Appl. Phys. **52**, 7182 (1981).
- [140] S. Plimpton, J. Comput. Phys. **117**, 1 (1995).
- [141] J. E. Jones, Proc. R. Soc. London. Ser. A **106**, 463 LP (1924).
- [142] A. C. T. van Duin, S. Dasgupta, F. Lorant, and W. A. Goddard, J. Phys. Chem. A **105**, 9396 (2001).
- [143] M. S. Daw and M. I. Baskes, Phys. Rev. B **29**, 6443 (1984).
- [144] M. S. Daw, S. M. Foiles, and M. I. Baskes, Mater. Sci. Reports **9**, 251 (1993).
- [145] Y. Mishin, in *Handb. Mater. Model. SE - 23*, edited by S. Yip (Springer Netherlands, 2005), pp. 459–478.
- [146] L. E. Toth, *Transition Metal Carbides and Nitrides* (Academic Press, New York, 1971).
- [147] S. T. Oyama, *The Chemistry of Transition Metal Carbides and Nitrides* (Springer Science & Business Media, 1996).
- [148] H. O. H. Pierson, *Handb. Refract. Carbides Nitrides Prop. Charact. Process. Apps.* 81 (1996).
- [149] D. D. Keiser and J. Cole, Mater. Sci. **597** (2007).
- [150] O. N. Carlson, A. H. Ghaneya, and J. F. Smith, Bull. Alloy Phase Diagrams **6**, 115 (1985).
- [151] V. N. Lipatnikov, A. I. Gusev, P. Etmayer, and W. Lengauer, J. Phys. Condens. Matter **11**, 163 (1999).
- [152] V. N. Lipatnikov, Russ. Chem. Rev. **74**, 697 (2005).

- [153] C. P. Buhsmer and P. H. Crayton, *J. Mater. Sci.* **6**, 981 (1971).
- [154] B. Ozturk, V. L. Fearing, J. A. Ruth, and G. Simkovich, *Metall. Trans. A* **13**, 1871 (1982).
- [155] X. Chong, Y. Jiang, R. Zhou, and J. Feng, *RSC Adv.* **4**, 44959 (2014).
- [156] L. Wu, T. Yao, Y. Wang, J. Zhang, F. Xiao, and B. Liao, *J. Alloys Compd.* **548**, 60 (2013).
- [157] H. Liu, J. Zhu, Y. Liu, and Z. Lai, *Mater. Lett.* **62**, 3084 (2008).
- [158] H. Matzke, in *Defect Diffus. Forum* (Trans Tech Publ, 1992), pp. 111–130.
- [159] G. Kresse and J. Furthmüller, *Comput. Mat. Sci.* **6**, 15 (1996).
- [160] G. Kresse and D. Joubert, *Phys. Rev. B* **59**, 1758 (1999).
- [161] P. E. Blöchl, *Phys. Rev. B* **50**, 17953 (1994).
- [162] P. Pulay, *Chem. Phys. Lett.* **73**, 393 (1980).
- [163] P. E. Blöchl, O. Jepsen, and O. K. Andersen, *Phys. Rev. B* **49**, 16223 (1994).
- [164] A. Togo, F. Oba, and I. Tanaka, *Phys. Rev. B - Condens. Matter Mater. Phys.* **78**, 1 (2008).
- [165] X. Wu, D. Vanderbilt, and D. R. Hamann, *Phys. Rev. B - Condens. Matter Mater. Phys.* **72**, 1 (2005).
- [166] A. U. Ortiz, A. Boutin, A. H. Fuchs, and F. X. Coudert, *J. Chem. Phys.* **138**, 174703 (2013).
- [167] A. Togo and I. Tanaka, *Scr. Mater.* **108**, 1 (2015).
- [168] G. Mills, H. Jónsson, and G. K. Schenter, *Surf. Sci.* **324**, 305 (1995).
- [169] H. Jónsson, G. Mills, and K. W. Jacobsen, in *Class. Quantum Dyn. Condens. Phase Simulations* (Citeseer, 1998), pp. 385–404.
- [170] E. Rudy and C. E. Brukl, *J. Am. Ceram. Soc.* **50**, 265 (1967).
- [171] S. Curtarolo, W. Setyawan, G. L. W. Hart, M. Jahnatek, R. V. Chepulskii, R. H. Taylor, S. Wang, J. Xue, K. Yang, O. Levy, M. J. Mehl, H. T. Stokes, D. O. Demchenko, and D. Morgan, *Comput. Mater. Sci.* **58**, 218 (2012).
- [172] G. L. W. Hart and R. W. Forcade, *Phys. Rev. B* **80**, 14120 (2009).

- [173] A. K. Rappe, C. J. Casewit, K. S. Colwell, W. A. Goddard, and W. M. Skiff, *J. Am. Chem. Soc.* **114**, 10024 (1992).
- [174] W. Xing, F. Meng, and R. Yu, *Sci. Rep.* **6**, 21794 (2016).
- [175] M. P. Arbutov, V. G. Fak, and B. V Khaenko, *Izv. Akad. Nauk SSSR, Neorg. Mater* **12**, 846 (1976).
- [176] K. Yvon, H. Nowotny, and R. Kieffer, *Monatshefte Für Chemie/Chemical Mon.* **98**, 34 (1967).
- [177] R. Hill, *Proc. Phys. Soc. Sect. A* **65**, 349 (2002).
- [178] N. W. Ashcroft and N. D. Mermin, *Solid State Physics* (Saunders College, 1976).
- [179] S. Lany and A. Zunger, *Model. Simul. Mater. Sci. Eng.* **17**, 84002 (2009).
- [180] C. Freysoldt, B. Grabowski, T. Hickel, J. Neugebauer, G. Kresse, A. Janotti, and C. G. Van De Walle, *Rev. Mod. Phys.* **86**, 253 (2014).
- [181] M. Hagen, *Philos. Mag. A* **77**, 447 (1998).
- [182] C. G. Van De Walle and J. Neugebauer, *J. Appl. Phys.* **95**, 3851 (2004).
- [183] M. T. Dove, *Introduction to Lattice Dynamics* (Cambridge University Press, 1993).
- [184] J. G. Mullen, *Phys. Rev.* **124**, 1723 (1961).
- [185] L. V. Azároff, *J. Appl. Phys.* **32**, 1658 (1961).
- [186] L. V. Azároff, *J. Appl. Phys.* **32**, 1663 (1961).
- [187] J. E. Saal and C. Wolverton, *Acta Mater.* **60**, 5151 (2012).
- [188] S. L. Dudarev, S. Y. Savrasov, C. J. Humphreys, and A. P. Sutton, *Phys. Rev. B* **57**, 1505 (1998).
- [189] W. Xie, W. Xiong, C. A. Marianetti, and D. Morgan, *Phys. Rev. B* **88**, 235128 (2013).
- [190] M. Methfessel and A. T. Paxton, *Phys. Rev. B* **40**, 3616 (1989).
- [191] W. M. Haynes, D. R. Lide, and T. J. Bruno, *CRC Handbook of Chemistry and Physics : A Ready-Reference Book of Chemical and Physical Data.* (2015).
- [192] G. Henkelman, B. P. Uberuaga, and H. Jónsson, *J. Chem. Phys.* **113**, 9901 (2000).
- [193] D. Sheppard, R. Terrell, and G. Henkelman, *J. Chem. Phys.* **128**, 134106 (2008).

- [194] B. J. Demaske, A. Chernatynskiy, and S. R. Phillpot, *J. Phys. Condens. Matter* **29**, (2017).
- [195] D. Shin and C. Wolverton, *Acta Mater.* **58**, 531 (2010).
- [196] C. Wolverton, *Acta Mater.* **55**, 5867 (2007).
- [197] A. Inoue and A. Takeuchi, *Acta Mater.* **59**, 2243 (2011).
- [198] Y. Q. Cheng and E. Ma, *Prog. Mater. Sci.* **56**, 379 (2011).
- [199] W. H. Wang, *Prog. Mater. Sci.* **57**, 487 (2012).
- [200] F. Xi, Y. Yu, C. Dai, Y. Zhang, and L. Cai, *J. Appl. Phys.* **108**, 1 (2010).
- [201] X. Huang, Z. Ling, H. S. Zhang, J. Ma, and L. H. Dai, *J. Appl. Phys.* **110**, 103519 (2011).
- [202] L. Lu, C. Li, W. H. Wang, M. H. Zhu, X. L. Gong, and S. N. Luo, *Mater. Sci. Eng. A* **651**, 848 (2016).
- [203] B. Cao, E. M. Bringa, and M. A. Meyers, *Metall. Mater. Trans. A* **38**, 2681 (2007).
- [204] E. M. Bringa, J. U. Cazamias, P. Erhart, J. Stölken, N. Tanushev, B. D. Wirth, R. E. Rudd, and M. J. Caturla, *J. Appl. Phys.* **96**, 3793 (2004).
- [205] M. M. Sichani and D. E. Spearot, *J. Appl. Phys.* **120**, 45902 (2016).
- [206] M. M. Sichani and D. E. Spearot, *Comput. Mater. Sci.* **108**, 226 (2015).
- [207] W. Ma, W. Zhu, and Y. Hou, *J. Appl. Phys.* **114**, 1 (2013).
- [208] W. Ma, W. Zhu, and J. Fuqian, *Appl. Phys. Lett.* **97**, 121903 (2010).
- [209] S. Marinier and L. J. Lewis, *Phys. Rev. B* **92**, 184108 (2015).
- [210] K. G. Chen, Y. Y. Yu, Z. G. Zhang, and S. Q. Shi, *Scr. Mater.* **120**, 62 (2016).
- [211] X. Huang, Z. Ling, and L. H. Dai, *J. Appl. Phys.* **116**, (2014).
- [212] S. G. Hao, C. Z. Wang, M. J. Kramer, and K. M. Ho, *J. Appl. Phys.* (2010).
- [213] H. L. Peng, M. Z. Li, W. H. Wang, C. Wang, and K. M. Ho, *Appl. Phys. Lett.* **96**, 30 (2010).
- [214] Z. D. Sha, Y. P. Feng, and Y. Li, *Appl. Phys. Lett.* **96**, 61903 (2010).
- [215] J. C. Lee, K. W. Park, K. H. Kim, E. Fleury, B. J. Lee, M. Wakeda, and Y. Shibutani, *J. Mater. Res.* **22**, 3087 (2007).

- [216] K. W. Park, J. I. Jang, M. Wakeda, Y. Shibutani, and J. C. Lee, *Scr. Mater.* **57**, 805 (2007).
- [217] Y. Q. Cheng, H. W. Sheng, and E. Ma, *Phys. Rev. B - Condens. Matter Mater. Phys.* **78**, 1 (2008).
- [218] N. Mattern, A. Schöps, U. Kühn, J. Acker, O. Khvostikova, and J. Eckert, *J. Non. Cryst. Solids* **354**, 1054 (2008).
- [219] Y. Q. Cheng, A. J. Cao, H. W. Sheng, and E. Ma, *Acta Mater.* **56**, 5263 (2008).
- [220] N. Mattern, P. Jovari, I. Kaban, S. Gruner, A. Elsner, V. Kokotin, H. Franz, B. Beuneu, and J. Eckert, *J. Alloy. Compd. J.* **485**, 163 (2009).
- [221] A. E. Lagogianni, G. Almyras, C. E. Lekka, and D. G. Papageorgiou, *J. Alloys Compd.* **483**, 658 (2009).
- [222] M. Li, C. Wang, S. Hao, M. Kramer, and K. Ho, *Phys. Rev. B* **80**, 1 (2009).
- [223] M. I. Mendeleev, D. J. Sordelet, and M. J. Kramer, *J. Appl. Phys.* **102**, (2007).
- [224] Y. Q. Cheng, E. Ma, and H. W. Sheng, *Phys. Rev. Lett.* **102**, (2009).
- [225] L. Davison, *Fundamentals of Shock Wave Propagation in Solids* (Springer Berlin Heidelberg, 2008).
- [226] H. Okamoto, *J. Phase Equilibria Diffus.* **29**, 204 (2008).
- [227] B. L. Holian, *Science* (80-.). **280**, 2085 (1998).
- [228] M. A. Meyers, H. Jarmakani, E. M. Bringa, and B. A. Remington, *Dislocations in Shock Compression* (2009).
- [229] L. A. Davis and S. Kavesh, *J. Mater. Sci.* **10**, 453 (1975).
- [230] P. E. Donovan, *Acta Metall.* **37**, 445 (1989).
- [231] K. M. Flores and R. H. Dauskardt, *Acta Mater.* **49**, 2527 (2001).
- [232] J. J. Lewandowski and P. Lowhaphandu, *Philos. Mag. A* **82**, 3427 (2002).
- [233] P. Lowhaphandu, S. L. Montgomery, and J. J. Lewandowski, *Scr. Mater.* **41**, 19 (1999).
- [234] J. Lu and G. Ravichandran, *J. Mater. Res.* **18**, 2039 (2003).
- [235] R. Vaidyanathan, M. Dao, G. Ravichandran, and S. Suresh, *Acta Mater.* **49**, 3781 (2001).

- [236] A. Peker and W. L. Johnson, *Appl. Phys. Lett.* **63**, 2342 (1993).
- [237] O. J. Kwon, Y. C. Kim, K. B. Kim, Y. K. Lee, and E. Fleury, *Met. Mater. Int.* **12**, 207 (2006).
- [238] N. Mattern, P. Jóvári, I. Kaban, S. Gruner, A. Elsner, V. Kokotin, H. Franz, B. Beuneu, and J. Eckert, *J. Alloys Compd.* **485**, 163 (2009).
- [239] J. Antonowicz, A. Pietnoczka, W. Zalewski, R. Bacewicz, M. Stoica, K. Georgarakis, and A. R. Yavari, *J. Alloys Compd.* **509**, S34 (2011).
- [240] M. I. Mendeleev, D. K. Rehbein, R. T. Ott, M. J. Kramer, and D. J. Sordelet, *J. Appl. Phys.* **102**, (2007).
- [241] M. I. Mendeleev, M. J. Kramer, R. T. Ott, D. J. Sordelet, D. Yagodin, and P. Popel, *Philos. Mag.* **89**, 967 (2009).
- [242] A. S. Argon, *Acta Metall.* **27**, 47 (1979).
- [243] C. A. Schuh and A. C. Lund, *Nat. Mater.* **2**, 449 (2003).
- [244] A. C. Lund and C. A. Schuh, *Acta Mater.* **51**, 5399 (2003).
- [245] Y. Q. Cheng and E. Ma, *Prog. Mater. Sci.* **56**, 379 (2011).
- [246] K. Yoshimoto, T. S. Jain, K. Van Workum, P. F. Nealey, and J. J. de Pablo, *Phys. Rev. Lett.* **93**, 175501 (2004).
- [247] M. Tsamados, A. Tanguy, C. Goldenberg, and J. L. Barrat, *Phys. Rev. E* **80**, 26112 (2009).
- [248] S. G. Mayr, *Phys. Rev. B* **79**, 60201 (2009).
- [249] H. L. Peng, M. Z. Li, and W. H. Wang, *Phys. Rev. Lett.* **106**, 1 (2011).
- [250] F. Shimizu, S. Ogata, and J. Li, *Mater. Trans.* **48**, 2923 (2007).
- [251] C. H. Rycroft, *Chaos An Interdiscip. J. Nonlinear Sci.* **19**, 41111 (2009).
- [252] H. W. Sheng, W. K. Luo, F. M. Alamgir, J. M. Bai, and E. Ma, *Nature* **439**, 419 (2006).
- [253] A. Stukowski, *Model. Simul. Mater. Sci. Eng.* **18**, 15012 (2010).
- [254] M. Wakeda, Y. Shibutani, S. Ogata, and J. Park, *Intermetallics* **15**, 139 (2007).
- [255] C. E. Lekka, A. Ibenskas, A. R. Yavari, and G. A. Evangelakis, *Appl. Phys. Lett.* **91**, 214103 (2007).

- [256] Y. Q. Cheng, A. J. Cao, and E. Ma, *Acta Mater.* **57**, 3253 (2009).
- [257] C. Zhong, H. Zhang, Q. P. Cao, X. D. Wang, D. X. Zhang, U. Ramamurty, and J. Z. Jiang, *Scr. Mater.* **114**, 93 (2016).
- [258] D. Ma, A. D. Stoica, X. L. Wang, Z. P. Lu, M. Xu, and M. Kramer, *Phys. Rev. B - Condens. Matter Mater. Phys.* **80**, 1 (2009).
- [259] Y. Q. Cheng, E. Ma, and H. W. Sheng, *Phys. Rev. Lett.* **102**, 1 (2009).
- [260] L. Zhang, Y. Cheng, A. Cao, J. Xu, and E. Ma, *Acta Mater.* **57**, 1154 (2009).
- [261] S. Trady, M. Mazroui, A. Hasnaoui, and K. Saadouni, *J. Non. Cryst. Solids* **443**, 136 (2016).
- [262] D. Vouagner, C. Coussa, C. Martinet, H. Hugueney, B. Champagnon, V. Califano, and V. Sigaev, *J. Non. Cryst. Solids* **353**, 1910 (2007).
- [263] V. N. Sigaev, S. V. Lotarev, E. V. Orlova, N. V. Golubev, V. V. Koltashev, V. G. Plotnichenko, and G. A. Komandin, *Glas. Ceram.* **67**, 105 (2010).
- [264] R. Shaltaf, H. K. Juwhari, B. Hamad, J. Khalifeh, G. M. Rignanese, and X. Gonze, *J. Appl. Phys.* **115**, 74103 (2014).
- [265] W. Kohn and L. J. Sham, *Phys. Rev.* **137**, (1965).
- [266] H. J. Monkhorst and J. D. Pack, *Phys. Rev. B* **13**, 5188 (1976).
- [267] S. Okamoto, A. J. Millis, and N. A. Spaldin, *Phys. Rev. Lett.* **97**, 56802 (2006).
- [268] P. B. Ghate, *Phys. Rev.* **133**, A1167 (1964).
- [269] Y. J. Hu, D. D. Wen, Y. Q. Jiang, Y. H. Deng, and P. Peng, *Trans. Nonferrous Met. Soc. China (English Ed.)* **25**, 533 (2015).
- [270] R. E. Ryltsev, B. A. Klumov, N. M. Chtchelkatchev, and K. Y. Shunyaev, *J. Chem. Phys.* **145**, (2016).
- [271] A. Foroughi, H. Ashuri, R. Tavakoli, D. Sopy, M. Stoica, and J. Eckert, (2017).
- [272] G. Duan, M. L. Lind, M. D. Demetriou, W. L. Johnson, W. A. Goddard, T. Çagin, and K. Samwer, *Appl. Phys. Lett.* **89**, 23 (2006).
- [273] T. L. Cheung and C. H. Shek, *J. Alloys Compd.* **434–435**, 71 (2007).
- [274] G. Kumar, T. Ohkubo, T. Mukai, and K. Hono, *Scr. Mater.* **57**, 173 (2007).
- [275] G. Duan, K. De Blauwe, M. L. Lind, J. P. Schramm, and W. L. Johnson, **58**, 159 (2008).

- [276] N. Barekar, P. Gargarella, K. Song, S. Pauly, U. Kühn, and J. Eckert, *J. Mater. Res.* **26**, 1702 (2011).
- [277] T. Fujita, P. F. Guan, H. W. Sheng, A. Inoue, T. Sakurai, and M. W. Chen, *Phys. Rev. B - Condens. Matter Mater. Phys.* **81**, 1 (2010).
- [278] A. R. Yavari, *Nature* **439**, 405 (2006).
- [279] H. W. Sheng, W. K. Luo, F. M. Alamgir, J. M. Bai, and E. Ma, *Nature* **439**, 419 (2006).
- [280] A. L. Greer, *Mater. Today* **12**, 14 (2009).
- [281] F. Li, X. J. Liu, and Z. P. Lu, **85**, 147 (2014).
- [282] C. Tang and C. H. Wong, *Intermetallics* **58**, 50 (2015).
- [283] J. C. Ye, J. Lu, C. T. Liu, Q. Wang, and Y. Yang, *Nat. Mater.* **9**, 619 (2010).
- [284] Y. Shi and M. L. Falk, *Phys. Rev. Lett.* **95**, 1 (2005).
- [285] A. J. Cao, Y. Q. Cheng, and E. Ma, *Acta Mater.* **57**, 5146 (2009).
- [286] Y. Cheng and E. Ma, *Phys. Rev. B* **80**, 064104:1 (2009).
- [287] Y. Shi and M. L. Falk, *Scr. Mater.* **54**, 381 (2006).

BIOGRAPHICAL SKETCH

Brian Demaske was born and raised in the suburbs of Cleveland, Ohio. He moved to Florida with his family in the summer of 2005. He attended the University of Florida (UF) after graduating high school, but decided to transfer to the University of South Florida (USF) in the spring of 2008. In 2010, he graduated from USF with a B.S. in physics. He started his graduate education in physics the following year. There he was introduced to the field of computational materials science. His main projects included molecular dynamics simulations of laser-matter interactions and shock compression of crystalline metals. After graduating from USF with his M.S. in physics in August 2012, he applied and was accepted into the doctoral program in Materials Science and Engineering at UF under the direction of Prof. Simon Phillpot, co-leader of the Florida Laboratory for Advanced Materials Engineering Simulation. During his graduate studies, Brian performed research in several different areas ranging from defect and diffusion behavior in carbides to high-strain-rate mechanical behavior of amorphous metals to ferroelectricity in ceramics. In December 2017, he graduated from UF with a Ph.D. in materials science and engineering.